

Prepared for:

Texas Commission on Environmental Quality
12100 Park 35 Circle MC 164
Austin, TX 78753

Prepared by:

Ramboll US Corporation
7250 Redwood Blvd., Suite 105
Novato, California 94945

June 30, 2020

Hemispheric Comprehensive Air Quality Model with Extensions, Enhancement and Testing

Final Report

PREPARED UNDER A CONTRACT FROM THE
TEXAS COMMISSION ON ENVIRONMENTAL QUALITY

The preparation of this document was financed through a contract from the State of Texas through the Texas Commission on Environmental Quality.

The content, findings, opinions and conclusions are the work of the author(s) and do not necessarily represent findings, opinions or conclusions of the TCEQ.



Hemispheric Comprehensive Air Quality Model with Extensions, Enhancement and Testing

Final Report

Ramboll
7250 Redwood Boulevard
Suite 105
Novato, CA 94945
USA

T +1 415 899 0700
<https://ramboll.com>

Contents

List of Acronyms and Abbreviations	vii
Executive Summary	9
1.0 Introduction	11
1.1 Project Objectives	11
1.2 Report Organization	12
2.0 Adapting Satellite Data for Initial/Boundary Conditions	13
2.1 Envisioned Approach	13
2.1.1 Revised Approach	13
2.1.2 Top Concentrations	16
2.1.3 Initial and Lateral Boundary Concentrations	19
3.0 WRF Simulations	20
3.1 EPA WRF Configuration	20
3.2 Ramboll WRF Configuration/Application Strategy	20
3.2.1 Increased Vertical Resolution	21
3.2.2 Multi-Scale Kain-Fritsch Convection	21
3.3 Results	21
4.0 H-CAMx Sensitivity Testing and Performance Evaluation	37
4.1 Configurations for Annual 2016 H-CAMx Runs	37
4.2 Global Measurement Data Selection	38
4.2.1 Surface Ozone Measurements	38
4.2.2 Ozonesonde Measurements	44
4.3 Postprocessing Methodology	46
4.3.1 Surface Ozone Data	46
4.3.2 Ozonesonde Data	46
4.4 Inter-Model Performance Comparison	46
4.4.1 Ozonesonde Comparisons	47
4.4.2 Surface Ozone Comparisons	53
4.5 H-CAMx Sensitivity Results	60
4.5.1 Ozonesonde Comparisons	60
4.5.2 Surface Ozone Comparisons	66
4.6 Recommended H-CAMx Configuration	71
5.0 Conclusion and Recommendations	73
5.1 Summary	73
5.2 Recommendations	75
6.0 References	76
Appendices	
Appendix A. Statistical Definitions	78

List of Figures

Figure 2-1.	Example MOPITT total atmospheric CO column (mol/cm ²) on March 9, 2019. With narrow view angles, the daily data swaths exhibit large areas of missing data over the globe.	14
Figure 2-2.	AIRS V6/L3 ozone fields (ppb) on June 1, 2016 at 6 pressure altitudes spanning the troposphere and lower stratosphere. Below 250 hPa (mb) ozone fields approach the a-priori climatological June average and at 1000 hPa the solution is almost entirely the a-priori. Note that 1000 hPa is often below continental terrain elevations, as shown by continental areas shaded white, and the highest terrain around the globe extends to altitudes above 700 hPa, as shown by diminishing continental areas shaded white.	15
Figure 2-3.	AIRS V6/L3 ozone fields (ppb) on June 1, 2016 at the 50 hPa (mb) pressure altitude, which is consistent with the top of the H-CAMx modeling domain.	16
Figure 2-4.	Daily H-CAMx ozone top concentrations derived from AIRS ozone retrievals at 50 mb. Individual plots are shown for January 15 (top left), April 15 (top right), July 15 (bottom left) and October 15 (bottom right).	17
Figure 2-5.	(Left) Original ozone top concentrations derived from AIRS 50 mb data on September 25-28 (top to bottom). (Right) Filled data fields for the same days. See text for details; filled top concentrations on the 26 th and 27 th are identical.	18
Figure 3-1.	Comparisons of January-average near-surface wind speed (top row), temperature (middle row) and absolute humidity (bottom row) between WRF Run0 (left), Run1 (middle) and their differences (right). Fields are extracted from the WRF layer containing 950 mb over oceans.	25
Figure 3-2.	Comparisons of January-average near-tropopause wind speed (top row), temperature (middle row) and absolute humidity (bottom row) between WRF Run0 (left), Run1 (middle) and their differences (right). Fields are extracted from the WRF layer containing 300 mb over oceans.	26
Figure 3-3.	Comparisons of July-average near-surface wind speed (top row), temperature (middle row) and absolute humidity (bottom row) between WRF Run0 (left), Run1 (middle) and their differences (right). Fields are extracted from the WRF layer containing 950 mb over oceans.	27
Figure 3-4.	Comparisons of July-average near-tropopause wind speed (top row), temperature (middle row) and absolute humidity (bottom row) between WRF Run0 (left), Run1 (middle) and their differences (right). Fields are extracted from the WRF layer containing 300 mb over oceans.	28
Figure 3-5.	Comparisons of January-average near-surface wind speed (top row), temperature (middle row) and absolute humidity (bottom	

	row) between WRF Run1 (left), Run2 (middle) and their differences (right). Fields are extracted from the WRF layer containing 950 mb over oceans.	29
Figure 3-6.	Comparisons of January-average near-tropopause wind speed (top row), temperature (middle row) and absolute humidity (bottom row) between WRF Run1 (left), Run2 (middle) and their differences (right). Fields are extracted from the WRF layer containing 300 mb over oceans.	30
Figure 3-7.	Comparisons of July-average near-surface wind speed (top row), temperature (middle row) and absolute humidity (bottom row) between WRF Run1 (left), Run2 (middle) and their differences (right). Fields are extracted from the WRF layer containing 950 mb over oceans.	31
Figure 3-8.	Comparisons of July-average near-tropopause wind speed (top row), temperature (middle row) and absolute humidity (bottom row) between WRF Run1 (left), Run2 (middle) and their differences (right). Fields are extracted from the WRF layer containing 300 mb over oceans.	32
Figure 3-9.	Comparisons of January-average near-surface wind speed (top row), temperature (middle row) and absolute humidity (bottom row) between WRF Run2 (left), Run3 (middle) and their differences (right). Fields are extracted from the WRF layer containing 950 mb over oceans.	33
Figure 3-10.	Comparisons of January-average near-tropopause wind speed (top row), temperature (middle row) and absolute humidity (bottom row) between WRF Run2 (left), Run3 (middle) and their differences (right). Fields are extracted from the WRF layer containing 300 mb over oceans.	34
Figure 3-11.	Comparisons of July-average near-surface wind speed (top row), temperature (middle row) and absolute humidity (bottom row) between WRF Run2 (left), Run3 (middle) and their differences (right). Fields are extracted from the WRF layer containing 950 mb over oceans.	35
Figure 3-12.	Comparisons of July-average near-tropopause wind speed (top row), temperature (middle row) and absolute humidity (bottom row) between WRF Run2 (left), Run3 (middle) and their differences (right). Fields are extracted from the WRF layer containing 300 mb over oceans.	36
Figure 4-1.	Northern hemispheric WDCRG ozone monitor locations. Note that ozone data may not be available for all locations for 2016.	39
Figure 4-2.	US CASTNET sites operating during 2016. Ozone is monitored at a majority subset of sites.	40
Figure 4-3.	All surface monitors with 2016 ozone data selected for H-CAMx MPE, color-coded by evaluation region.	41
Figure 4-4.	European monitors with 2016 ozone data selected for H-CAMx MPE.	41

Figure 4-5.	US monitors with 2016 ozone data selected for H-CAMx MPE.	42
Figure 4-6.	Global ozonesonde launch sites available in the WOUDC dataset with data available in 2016.	44
Figure 4-7.	Northern hemispheric ozonesonde locations selected for H-CAMx MPE.	45
Figure 4-8.	Modeled (grey) and observed (red) ozone profiles at global ozonesonde sites. The average over all 2016 profiles are shown as the solid lines, annual minimum to maximum ozone ranges are shaded. The number of profiles in 2016 and station latitude/longitude are noted above each plot.	48
Figure 4-9.	Measured and modeled annual average (black dots) and 10 th -90 th percentile ranges (vertical bars) of surface ozone by US site (top panel), and modeled statistical performance metrics for bias (NMB as decimal fraction) and gross error (NME as decimal fraction) by US site (bottom panel). Observations are shown in grey, GEOS-Chem results are shown in blue, H-CAMx Run0 results are shown in orange, and H-CMAQ results are shown in green.	54
Figure 4-10.	Measured and modeled annual average (black dots) and 10 th -90 th percentile ranges (vertical bars) of surface ozone by European site (top panel), and modeled statistical performance metrics for bias (NMB as decimal fraction) and gross error (NME as decimal fraction) by European site (bottom panel). Observations are shown in grey, GEOS-Chem results are shown in blue, H-CAMx Run0 results are shown in orange, and H-CMAQ results are shown in green.	55
Figure 4-11.	Measured and modeled annual average (black dots) and 10 th -90 th percentile ranges (vertical bars) of surface ozone by Asian site (left panel), and modeled statistical performance metrics for bias (NMB as decimal fraction) and gross error (NME as decimal fraction) by Asian site (right panel). Observations are shown in grey, GEOS-Chem results are shown in blue, H-CAMx Run0 results are shown in orange, and H-CMAQ results are shown in green.	56
Figure 4-12.	Measured and modeled annual average (black dots) and 10 th -90 th percentile ranges (vertical bars) of surface ozone by Oceanic site (left panel), and modeled statistical performance metrics for bias (NMB as decimal fraction) and gross error (NME as decimal fraction) by Oceanic site (right panel). Observations are shown in grey, GEOS-Chem results are shown in blue, H-CAMx Run0 results are shown in orange, and H-CMAQ results are shown in green.	56
Figure 4-13.	Measured and modeled annual average (black dots) and 10 th -90 th percentile ranges (vertical bars) of surface ozone by Polar site (left panel), and modeled statistical performance metrics for bias (NMB as decimal fraction) and gross error (NME as decimal fraction) by Polar site (right panel). Observations are	

	shown in grey, GEOS-Chem results are shown in blue, H-CAMx Run0 results are shown in orange, and H-CMAQ results are shown in green.	57
Figure 4-14.	Alignment of the H-CAMx 108-km grid cell (left, blue and right, red) and GEOS-Chem grid cell (right, blue) containing the Trinidad Head monitoring site (green dot).	58
Figure 4-15.	Time series over 2016 of monitored (blue) and simulated (red) MDA8 ozone at the WDCRG Hanoi, Vietnam site. Results for H-CAMx are in the top panel, GEOS-Chem in the bottom panel (not differences in vertical ozone scale in each). H-CMAQ results are similar to H-CAMx but present higher peak ozone.	58
Figure 4-16.	H-CAMx (grey) and observed (red) ozone profiles at global ozonesonde sites. The average over all 2016 profiles are shown as the solid lines, annual minimum to maximum ozone ranges are shaded. The number of profiles in 2016 and station latitude/longitude are noted above each plot.	61
Figure 4-17.	Measured and H-CAMx annual average (black dots) and 10 th -90 th percentile ranges (vertical bars) of surface ozone by US site (top panel), and modeled statistical performance metrics for bias (NMB as decimal fraction) and gross error (NME as decimal fraction) by US site (bottom panel). Observations are shown in grey, H-CAMx results are shown in color.	67
Figure 4-18.	Measured and H-CAMx annual average (black dots) and 10 th -90 th percentile ranges (vertical bars) of surface ozone by European site (top panel), and modeled statistical performance metrics for bias (NMB as decimal fraction) and gross error (NME as decimal fraction) by European site (bottom panel). Observations are shown in grey, H-CAMx results are shown in color.	68
Figure 4-19.	Measured and H-CAMx annual average (black dots) and 10 th -90 th percentile ranges (vertical bars) of surface ozone by Asian site (left panel), and modeled statistical performance metrics for bias (NMB as decimal fraction) and gross error (NME as decimal fraction) by Asian site (right panel). Observations are shown in grey, H-CAMx results are shown in color.	69
Figure 4-20.	Measured and H-CAMx annual average (black dots) and 10 th -90 th percentile ranges (vertical bars) of surface ozone by Oceanic site (left panel), and modeled statistical performance metrics for bias (NMB as decimal fraction) and gross error (NME as decimal fraction) by Oceanic site (right panel). Observations are shown in grey, H-CAMx results are shown in color.	69
Figure 4-21.	Measured and H-CAMx annual average (black dots) and 10 th -90 th percentile ranges (vertical bars) of surface ozone by Polar site (left panel), and modeled statistical performance metrics for bias (NMB as decimal fraction) and gross error (NME as	

	decimal fraction) by Polar site (right panel). Observations are shown in grey, H-CAMx results are shown in color.	70
Figure 4-22.	Season-averaged surface ozone fields simulated by the H-CAMx Run1 modeling configuration: winter (DJF) in top left, spring (MAM) in top right, summer (JJA) in bottom left, and autumn (SON) in bottom right.	72

List of Tables

Table 3-1.	EPA 2016 hemispheric WRF v3.8 model configuration (Run0).	20
Table 3-2.	Vertical layer structures for EPA and Ramboll WRF simulations. EPA Run0 and Ramboll Run1 are shown in the left 5 columns; Ramboll Run2 and Run3 are shown in the right 5 columns.	22
Table 3-3.	WRF physics options used in Run0 through Run3.	23
Table 4-1.	List and description of H-CAMx simulations conducted in this project.	37
Table 4-2.	Runtimes for each H-CAMx scenario using the parallelization noted in the text and the model configuration listed in Table 4-1.	38
Table 4-3.	List of all surface ozone monitoring sites selected for H-CAMx MPE.	42
Table 4-4.	List of ozonesonde sites selected for H-CAMx MPE.	45
Table 4-5.	Site-averaged annual bias (NMB, %), gross error (NME, %) and correlation coefficient (R) over five global monitoring groups for each model. Statistics are color coded according to whether they meet (green) or exceed (orange) ozone statistical performance criteria recommended by Emery et al. (2016) for regional photochemical modeling (NMB $\leq \pm 15\%$; NME $\leq 25\%$, R > 0.50).	60
Table 4-6.	Site-averaged annual bias (NMB, %), gross error (NME, %) and correlation coefficient (R) over five global monitoring groups for each H-CAMx run. Statistics are color coded according to whether they meet (green) or exceed (orange) ozone statistical performance criteria recommended by Emery et al. (2016) for regional photochemical modeling (NMB $\leq \pm 15\%$; NME $\leq 25\%$, R > 0.50).	71

LIST OF ACRONYMS AND ABBREVIATIONS

ACM2	Asymmetric Convective Model, version 2
AIRS	Atmospheric Infrared Sounder
BC	Boundary concentrations
C	Celsius
CAMx	Comprehensive Air quality Model with extensions
CASTNET	Clean Air Status and Trends Network
CB6r4	Carbon Bond 6, revision 4 photochemistry mechanism
CF	Coarse/Fine particulate matter chemistry
CiG	Cloud-in-Grid
cm	centimeter
CMAQ	Community Multiscale Air Quality model
CO	Carbon monoxide
EPA	US Environmental Protection Agency
FY	Fiscal year
g	gram
GAW	Global Atmospheric Watch
GCM	Global climate model
GEOS-Chem	Goddard Earth Observing System global Chemistry model
GES DISC	Goddard Earth Science Data and Information Services Center
GFS	Global Forecasting System
H-CAMx	Hemispheric CAMx
H-CMAQ	Hemispheric CMAQ
hPa	hectopascals (see also mb)
IC	Initial concentrations
IO-API	Input/Output Application Programming Interface
IR	Infrared
K	Kelvin
K-F	Kain-Fritsch convection algorithm
kg	Kilogram
km	Kilometer
Kv	Vertical diffusivity
L2/L3	Quality level 2, level 3
LSM	Land surface model
m	Meter
mb	millibar (see also hPa)
MDA8	Maximum daily 8-hour average
MM5	Fifth-generation Mesoscale Model
mol	Mole, Avogadro's number
MOPITT	Measurements of Pollution in the Troposphere
MPE	Model performance evaluation
MPI	Message Passing Interface
MSKF	Multiscale Kain-Fritsch convection algorithm
MSL	Mean seal level
NASA	National Aeronautics and Space Administration
NCAR	National Center for Atmospheric Research
NCO	netCDF operators
netCDF	Network Common Data Form

NILU	Norwegian Institute for Air Research
NMB	Normalized mean bias
NME	Normalized mean error
NO ₂	Nitrogen dioxide
NOAA	National Oceanic and Atmospheric Administration
NO _x	Nitrogen oxides
OMI	Ozone Monitoring Instrument
OMP	Open Multi-Processor
P-X	Pleim-Xiu algorithm
PBL	Planetary boundary layer
PM	Particulate matter
ppb	Parts per billion
Q-Q	Quantile-quantile regression plot
QA/QC	Quality assurance / quality control
QAPP	Quality Assurance Project Plan
R	Correlation coefficient
RRTMG	Rapid Radiative Transfer Model for GCMs
s	Second
SA	Source Apportionment
SIP	State Implementation Plan
SO ₂	Sulfur dioxide
TCEQ	Texas Commission on Environmental Quality
TES	Tropospheric Emission Spectrometer
TOMS	Total Ozone Mapping Spectrometer
US	United States
UV	Ultraviolet
VOC	Volatile organic compounds
WDCRG	World Data Centre for Reactive Gases
WMO	World Meteorological Organization
WOUDC	World Ozone and Ultraviolet Radiation Data Centre
WRF	Weather Research and Forecasting model
YSU	Yonsei University

EXECUTIVE SUMMARY

This project built upon previous work conducted in Fiscal Year 2019 (FY19) to enhance and further evaluate a Northern Hemispheric application of the Comprehensive Air quality Model with extensions (H-CAMx) in preparation for regulatory and policy use. The project involved three components: (1) evaluate and develop the use of satellite data products to derive hemispheric boundary concentrations; (2) apply and evaluate alternative meteorological model configurations to test H-CAMx sensitivity to vertical resolution and sub-grid convection; and (3) conduct a more comprehensive model performance for the H-CAMx application year of 2016.

The TCEQ runs CAMx on regional-scale modeling grids to support regulatory assessments for ozone. TCEQ also uses the Goddard Earth Observing System model with Chemistry (GEOS-Chem), a global photochemical model, to develop initial/boundary concentrations (IC/BC) for TCEQ's regional CAMx applications. GEOS-Chem uses different chemical mechanisms than CAMx, lacks a source apportionment capability, and its science updates are frequently out-of-step with the latest enhancements to CAMx. In FY18, Ramboll conducted a scoping study for TCEQ to assess the feasibility of applying CAMx over the Northern Hemisphere, finding that it is both feasible and desirable to pursue this goal. The advantages and tangible benefits of H-CAMx range from chemical consistency to seamless integration of the CAMx Source Apportionment (SA) tool, and to immediate availability of future CAMx updates and enhancements for both regional and hemispheric applications. H-CAMx will greatly improve TCEQ's ability to characterize the impact of global emissions on Texas air quality. In FY19, Ramboll developed and applied H-CAMx for the May-September 2016 season using meteorological and emission datasets derived by the US Environmental Protection Agency (EPA). That project included an example source apportionment run for the month of September 2016, and an initial review of H-CAMx performance against ozonesonde measurements from around the northern hemisphere. However, the project was limited by the EPA's emissions and meteorological inputs available, addressed only the Texas ozone season, and relied upon IC/BCs derived from readily available 2016 concentration fields generated by a third-party global model.

In this project we developed daily H-CAMx ozone top BCs from daily global satellite ozone data, which define stratospheric ozone profiles as H-CAMx runs. We employed a different approach to address tropospheric IC and lateral BCs for ozone and other important and highly spatially/temporally variable compounds such as CO, NO_x, VOC and PM, to alleviate the dependence of H-CAMx on third-party global models. We developed a library of monthly-averaged ICs and lateral BCs for all CAMx species from the raw output of GEOS-Chem, which can be used to represent a recent global climatology within a reasonable interval (arguably ± 5 years) from 2016. Since they are model-derived, all species are chemically consistent with each other. This solution provides the best balance among flexibility and representativeness and allows for a shortened hemispheric spin-up period.

We employed the same version of the Weather Research and Forecasting model used by EPA to develop two alternative meteorological representations over the hemispheric grid for the entire year 2016, including an H-CAMx "spin-up" period covering October 1 – December 31, 2015. Key changes in the WRF configuration included: (1) increasing vertical resolution in the mid-troposphere through the lower stratosphere; and (2) invoking an alternative sub-grid cumulus convection option that supports the CAMx "Cloud-in-Grid" convective sub-model.

We conducted a qualitative comparison of wind speed, temperature and humidity fields derived from our alternative WRF configurations to EPA's original WRF results at two altitudes (near-surface and near-tropopause) and for two months (January and July). Our results indicated no spurious or concerning differences; some minor differences occurring for near-surface humidity and temperature

were likely related to our WRF application methodology that affected soil moisture content. Differences arising from the modified layer structure were consistent with expectations and related to deeper layers resolving the lower boundary layer and better resolution of the temperature and wind profiles at jet stream altitudes. Only minor effects aloft and near the surface occurred with the alternative sub-grid convection scheme.

We compared results from our four H-CAMx runs, and the 2016 runs of GEOS-Chem and EPA's H-CMAQ, to deep ozone profiles from 22 global ozonesonde balloon launch sites as well as to surface-level ozone measurements from 67 global monitoring sites. With respect to ozone profiles, GEOS-Chem consistently best replicated stratospheric ozone at most sites around the world, with a slight negative bias in the troposphere. H-CMAQ was similar to GEOS-Chem but consistently exhibited more negative bias throughout the profiles. Conversely, H-CAMx consistently generated a negative bias in the stratosphere and a positive bias in the troposphere. All models generally exhibited narrower minimum-to-maximum ranges than the observations. At the surface, all three models performed adequately at most sites with a few outliers. GEOS-Chem exhibited a consistently negative ozone bias, H-CAMx exhibited a consistently positive ozone bias, while H-CMAQ had a mix of over and under predictions. Statistical performance for H-CAMx and H-CMAQ were more consistent with each other than GEOS-Chem, given their equivalent meteorology, emissions, and grid structures. The model inter-comparison led to identification of a few issues with EPA-derived emissions in the H-CAMx/CMAQ datasets.

In analyzing performance of H-CAMx sensitivity runs against ozonesondes, we found that all H-CAMx sensitivity cases exhibited improved performance (higher concentrations) for stratospheric ozone from a minor adjustment in the stratospheric ozone scheme. However, H-CAMx performance aloft degraded at two Asian sites (Hong Kong and Hanoi) downwind of the Himalayas where the model over predicted significantly. The higher stratospheric ozone also resulted in a slight increase (and over prediction) in upper and mid-tropospheric ozone. Somewhat surprisingly, this increase was further enhanced with the introduction of more vertical resolution. Therefore, numerically diffusive transport of stratospheric ozone into the upper troposphere was not so much a result of insufficient vertical resolution, but apparently caused by the diffusive nature of the CAMx vertical transport solver in combination with the WRF terrain-following vertical coordinate structure. This issue could be relieved, at least partially, by employing WRF's new hybrid vertical coordinate, which was not tested here. There were no obvious impacts to ozone profiles from introducing the CAMx Cloud-in-Grid sub-grid convection treatment.

At the surface, the different H-CAMx sensitivity cases were consistent, with a tendency for H-CAMx to overpredict ozone in all cases. Over predictions tended toward progressively higher mean ozone in each successive case, especially among site in the US and Europe. None of the modifications applied in the sensitivity cases resulted in fundamentally different effects on surface ozone, except to drive model bias slightly higher. In the case with enhanced vertical resolution, surface ozone increased most likely because of the deeper surface layer as opposed to any significant affect aloft. As for changes to sub-grid convection schemes, they tended to bring more mid- and upper-level ozone to the surface throughout the year at low and mid latitudes.

On the basis of the analyses described in this report, we recommend that TCEQ continue to apply H-CAMx with the original 44 layers rather than 53 layers. The lower vertical resolution does not appear to have a material impact on simulated ozone while it minimizes runtimes. We cannot offer any specific recommendation on the use of the Cloud-in-Grid convective model as it had negligible apparent impacts. In Section 5 we recommend several updates and additional analyses for future work.

1.0 INTRODUCTION

The Texas Commission on Environmental Quality (TCEQ) uses the Comprehensive Air quality Model with Extensions (CAMx; Ramboll, 2020a) for State Implementation Planning (SIP) purposes. CAMx requires input datasets that specify the temporal and spatial distributions of a multitude of chemical concentrations for initial and boundary concentrations (IC/BC). TCEQ uses a global chemical transport model called the Goddard Earth Observing System model with Chemistry (GEOS-Chem; Bey et al., 2001; Harvard, 2020) to develop CAMx IC/BC on a domain spanning much of North America. However, GEOS-Chem is primarily intended for studies of the global atmosphere and so uses different atmospheric chemical mechanisms than CAMx to simulate ozone and particulate matter (PM). Additionally, GEOS-Chem lacks a source apportionment capability for tracking ozone and PM contributions back to the source categories and regions where precursors were emitted. Finally, due to different priorities, GEOS-Chem's development and science updates are frequently out-of-step with the latest enhancements to CAMx.

In fiscal year 2018 (FY18), Ramboll conducted a scoping study for TCEQ to assess the feasibility of applying CAMx over the Northern Hemisphere (Ramboll, 2018). Those results showed that it is both feasible and desirable to pursue this goal. The advantages and tangible benefits of hemispheric CAMx include: (1) a source of chemically consistent BCs for TCEQ's regional modeling applications; (2) a seamless and stream-lined integration of the CAMx Source Apportionment (SA) tool to track contributions from foreign sources to ozone and PM in Texas and other states; (3) chemical and physical consistency between global and regional scales in a single model framework; and (4) immediate availability of future CAMx updates and enhancements for hemispheric applications without the need to implement them in other global models. Since TCEQ is familiar with CAMx and its SA features, the Hemispheric CAMx (H-CAMx) could be readily subsumed into TCEQ's set of modeling tools. Successful implementation of H-CAMx will greatly improve TCEQ's ability to characterize the impact of emissions outside the boundaries of the current modeling domain on Texas air quality.

In fiscal year 2019 (FY19), Ramboll developed an application of H-CAMx (Ramboll, 2019a) for the period April-September 2016. The US Environmental Protection Agency (EPA) developed 2016 meteorological fields, anthropogenic emissions, and certain natural emission components to support their hemispheric applications of the Community Multiscale Air Quality model (H-CMAQ; Mathur et al., 2017). Ramboll adapted those inputs and developed other inputs, including initial/boundary concentrations (IC/BC), photolysis data, and oceanic and windblown dust emissions. The H-CAMx application required updates to the CAMx model and certain support programs. The project included an example SA run for the month of September 2016 and extraction of chemical and SA boundary concentrations for the TCEQ's North American 36-km modeling domain. Ramboll performed an initial review of H-CAMx performance against ozonesonde measurements from around the northern hemisphere, and found that model results for ozone throughout the troposphere were reasonable and generally compared well with ozone profiles. However, the FY19 H-CAMx project was limited by the emissions and meteorological inputs available, addressed only the Texas ozone season, and relied upon IC/BCs derived from readily available 2016 concentration fields generated by a third-party global model.

1.1 Project Objectives

This project built upon the FY19 effort to enhance and further evaluate H-CAMx in preparation for regulatory and policy use. Specifically, project objectives included:

- Evaluate and develop the use of satellite data products to derive lateral and top boundary concentrations and reduce H-CAMx reliance on other global models;

- Apply and evaluate alternative configurations of the Weather Research Forecasting (WRF) model, which provides meteorological data to H-CAMx, to test effects of improved vertical resolution and to allow the use of the CAMx “cloud-in-grid” (CiG) convective sub-model;
- Conduct a more comprehensive model performance for the entire year of 2016.

Activities documented in this report adhered to the Work Plan as closely as possible and included quality assurance/quality control (QA/QC) checks following our Quality Assurance Project Plan (QAPP).

1.2 Report Organization

Section 2 documents activities in which we evaluated satellite data products as a source of IC/BCs to support H-CAMx applications in any year. Section 3 describes our configuration of WRF with additional layers to evaluate effects on tropospheric pollutant transport and an alternative sub-grid convection scheme that can support the CAMx CiG convective algorithm. Section 4 describes H-CAMx applications over the entire year of 2016, and reports on the expanded model performance evaluation that includes additional global surface and upper air measurement data for ozone. Additionally, Section 4 includes a comparison of H-CAMx results to the 2016 GEOS-Chem output used previously to develop H-CAMx initial/boundary concentrations, and to EPA’s 2016 H-CMAQ results. Finally, Section 4 reports on CAMx sensitivity runs using the alternative boundary concentrations described in Section 2 and to the use of alternative WRF simulations described in Section 3.

2.0 ADAPTING SATELLITE DATA FOR INITIAL/BOUNDARY CONDITIONS

2.1 Envisioned Approach

In the FY19 project, Ramboll acknowledged that the process to set IC/BCs from pre-existing global model output datasets limited the utility of H-CAMx as a stand-alone modeling system. In this project, Ramboll evaluated the utility of current satellite data products in providing reliable, well-resolved, daily global concentration data at many heights throughout the troposphere and lower stratosphere. Our envisioned approach involved deriving three-dimensional fields of ozone from the National Aeronautics and Space Administration's (NASA) newly combined Atmospheric Infrared Sounder (AIRS) and Ozone Monitoring Instrument (OMI) data product¹, and carbon monoxide (CO) from the National Center for Atmospheric Research (NCAR) Measurements of Pollution in the Troposphere (MOPITT) data product². Only ozone fields derived from AIRS/OMI would be processed to top BC input fields, whereas both AIRS/OMI ozone and MOPITT CO would be processed to ICs and lateral BCs. For other trace compounds including nitrogen oxides (NO_x), volatile organic compounds (VOC), PM and methane, we planned to apply default climatological profiles that are appropriate for equatorial areas (i.e., following EPA's approach for H-CMAQ).

The NASA AIRS-OMI ozone product represents a new combination of AIRS (thermal infrared or IR) and OMI (ultraviolet or UV) spectral radiances that provides better accuracy and improved atmospheric sensitivity to quantify the vertical distribution of tropospheric composition. It yields similar vertical information as the Tropospheric Emission Spectrometer (TES), considered the "gold standard", but with greater spatial coverage. It also includes cloud and diagnostic information for ingestion into chemical weather models.

Based on a review of AIRS-OMI V1 (Herman et al., 2017) and e-mail communications with one of the investigators (Keven Bowman, personal communication) this data product is not yet ready for routine use. The current "Level 2" (L2) data product is considered a preliminary "beta" as the latest calibration technique has not yet been applied. The first full data availability is expected in September 2020. The L2 data are not yet gridded, consisting on only raw daily "swath" data with the vertical data grid varying between soundings in the lower troposphere (but fixed at higher altitudes). Our review of available data in January 2020 revealed that L2 data were missing during July-August 2016 as the AIRS-OMI team is continuing to implement various changes.

The NCAR MOPITT V8 CO product is based on IR radiances from the TERRA satellite since 2000. The gridded profile data prior to 2018 are "Level 3" (L3) and are characterized as "archival quality". However, our review of this product revealed that daily swaths are not wide enough for complete global coverage (Figure 2-1) although monthly-averaged data do have complete coverage.

2.1.1 Revised Approach

As a result of the issues stemming from our review of the AIRS/OMI and MOPITT products, we decided to revise our approach to find an appropriate alternative source of satellite-based data and to consider other methods that would more rigorously address other trace constituents. The technical issues described above, and the revised approach detailed below, were discussed with the TCEQ project manager who concurred with our findings and approach.

¹ <https://tes.jpl.nasa.gov/science/highlights/aura-highlights>

² <https://www2.acom.ucar.edu/mopitt>

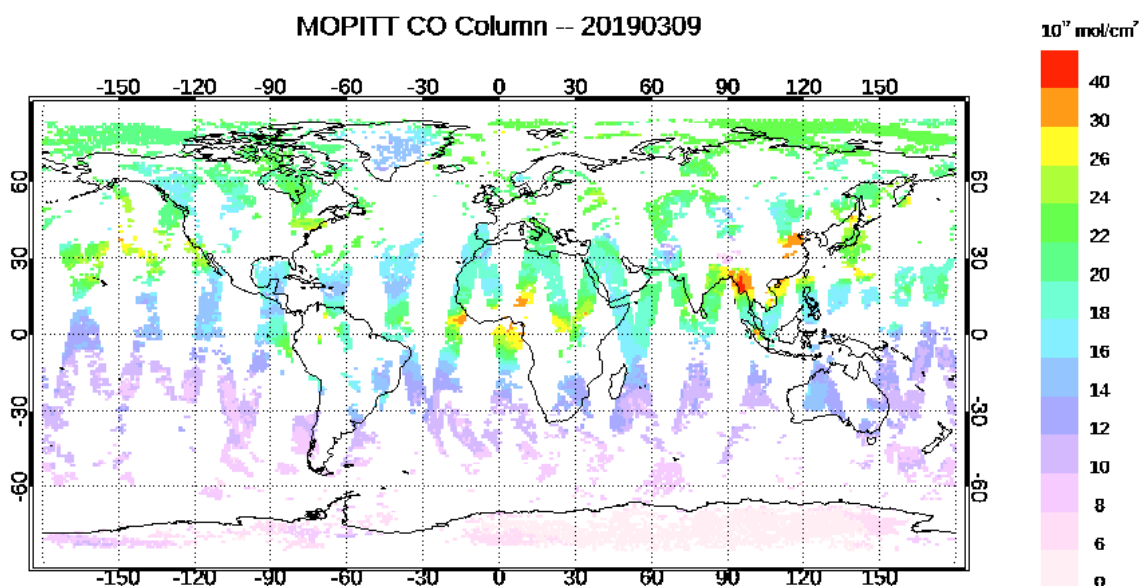


Figure 2-1. Example MOPITT total atmospheric CO column (mol/cm²) on March 9, 2019. With narrow view angles, the daily data swaths exhibit large areas of missing data over the globe.

We turned our attention to the well-established NASA AIRS V6 product³, which includes ozone, CO and methane as L3 quality-controlled filtered gridded data at 1-degree horizontal resolution and 24 pressure levels in the vertical (roughly 100 mb resolution in the troposphere). Because AIRS is a polar orbiting IR instrument, it measures ozone profiles day and night, whereas UV sensors used by Total Ozone Mapping Spectrometer (TOMS) such as OMI can only measure ozone during sunlit conditions. AIRS data are recorded over 15 orbits per day (1.5 hours apart). Ascending swaths (south to north) are daytime measurements, while descending swaths (north to south) are nighttime measurements as the satellite crosses over the north pole to the other side of the Earth. Equatorial crossings of all swaths occur around 1:30 AM/PM local time; daily data start and end at 180°E/W where the neighboring swaths are the farthest apart in time by a full day. Daily, 8-day and monthly averaged datasets are available.

We contacted the AIRS investigators to understand how the ozone profile data are produced, and reviewed available documentation (Barnet et al., 2007) and the User's Guide (Olsen et al., 2017) to understand advantages and disadvantages of the data. A complex iterative procedure is used that combines satellite-estimated profiles of temperature, water vapor and ozone with a set of initial guess ozone profiles (called the "a-priori"). The a-priori represents a monthly climatology resolved in 10-degree latitude bands between 80°S – 80°N and 100 pressure levels in the vertical. Because of progressively less AIRS ozone sensitivity from the tropopause towards the surface, the ozone a-priori is dominant in the lower troposphere and resulting AIRS ozone fields reflect primarily the a-priori near the surface (Figure 2-2). On the other hand, CO and methane soundings have maximum sensitivity in the mid-troposphere (300-500 mb), but they also converge to their a-priori initial guess near the surface. Daily AIRS CO products exhibit smaller areas of missing data between swaths around the globe than MOPITT. Even though data are provided on 24 pressure levels, there may be unreliable measurement data on each level.

³ https://airs.jpl.nasa.gov/data/physical_retrievals

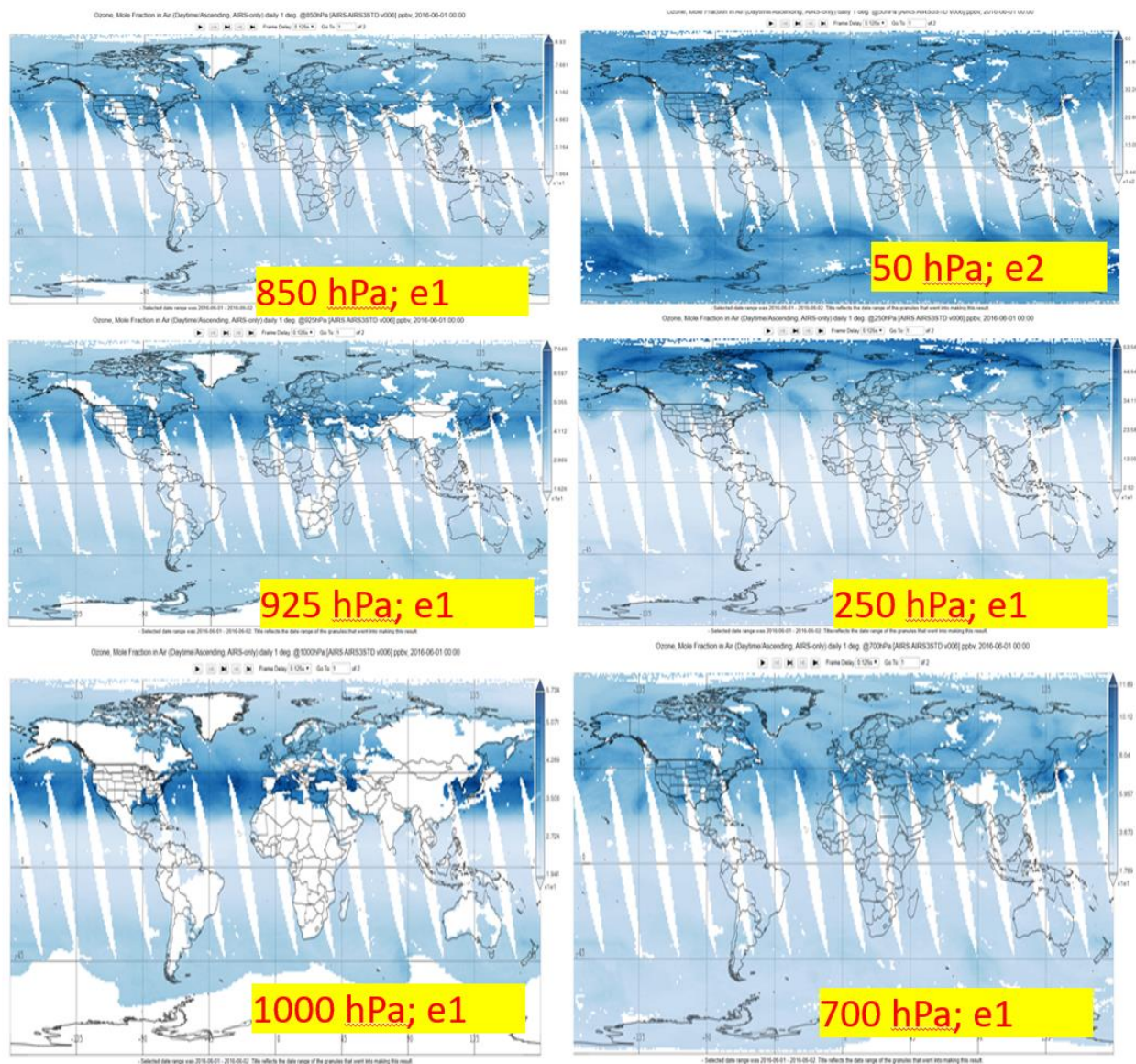


Figure 2-2. AIRS V6/L3 ozone fields (ppb) on June 1, 2016 at 6 pressure altitudes spanning the troposphere and lower stratosphere. Below 250 hPa (mb) ozone fields approach the a-priori climatological June average and at 1000 hPa the solution is almost entirely the a-priori. Note that 1000 hPa is often below continental terrain elevations, as shown by continental areas shaded white, and the highest terrain around the globe extends to altitudes above 700 hPa, as shown by diminishing continental areas shaded white.

The V6/L3 AIRS data are available as netCDF4 gridded datasets and are directly useable to support the development of H-CAMx IC/BCs. While the ozone, CO and methane products are questionable in the lower troposphere, AIRS ozone is sufficient to characterize spatial and temporal variations in the stratosphere at the top of the model (Figure 2-3). Therefore, we developed a tool that would temporarily use the AIRS ozone product to develop top BCs while easily adaptable to the AIRS-OMI ozone product when it becomes available in the near future.

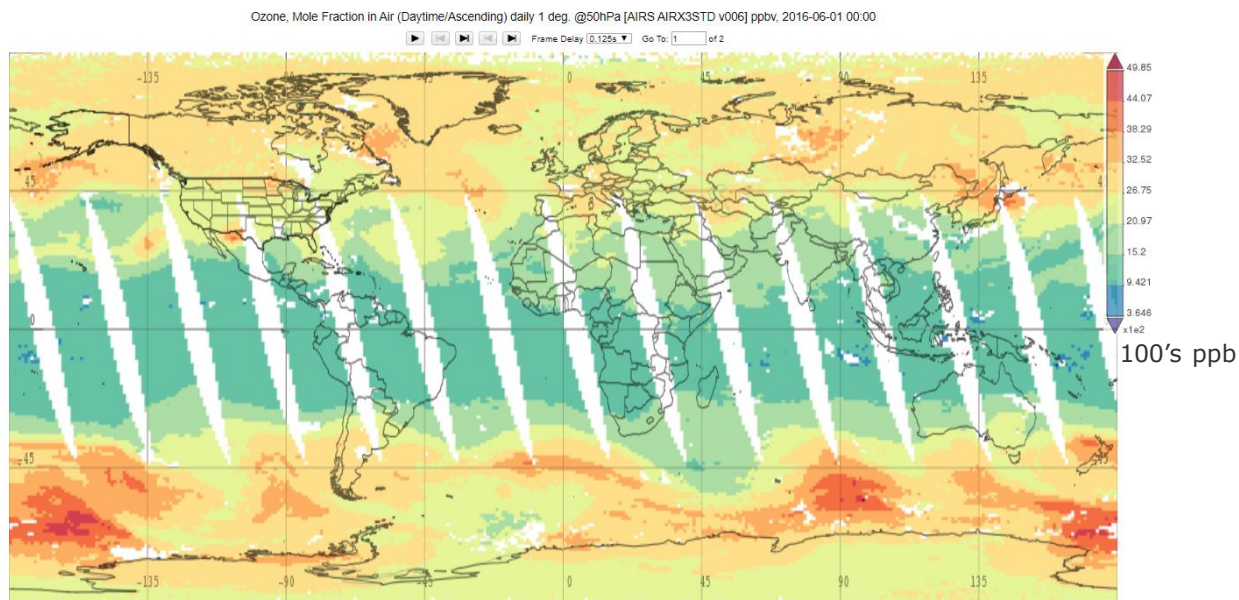


Figure 2-3. AIRS V6/L3 ozone fields (ppb) on June 1, 2016 at the 50 hPa (mb) pressure altitude, which is consistent with the top of the H-CAMx modeling domain.

2.1.2 Top Concentrations

We developed daily H-CAMx ozone top BC input files from daily global AIRS ozone data at the 50 mb pressure level, which coincides with the top pressure of both WRF and H-CAMx modeling domains. AIRS datafiles in netCDF4 format were obtained from the NASA GES DISC website⁴. A new Fortran program, derived from the existing O3MAP preprocessor, translates AIRS data to the CAMx top BC Fortran binary input file format (note that a future update will produce top BC files as netCDF4). The new program, called AIRS2CAMxTC, supports all CAMx map projections, and the Fortran code will ease installation and use at TCEQ.

The program first combines separate ascending and descending swath data into a single ozone field. It then fills missing data zones that routinely occur between the swaths (as seen in Figure 2-3), and in other more randomly-occurring missing data areas, via spatial interpolation using a similar but improved approach as the O3MAP preprocessor. The improved interpolation approach maintains the zonal character of stratospheric ozone while limiting sudden large concentration jumps between valid and interpolated data. Figure 2-4 presents examples of ozone top concentrations for representative days in each of the four quarters of 2016.

AIRS data were completely missing during September 26-27, 2016 and ozone data were missing over large portions of the northern hemisphere on September 25 and 28 that exceeded the ability for the AIRS2CAMxTC interpolation scheme to fill. We developed a second Fortran program called AIRSaverage that serves two functions: (1) fill large areas of missing data with surrogate data from an adjacent day; (2) fill entirely missing days with averages from days on either side. We used this program to generate complete ozone top concentration input files for the September 25-28, 2016

⁴ Goddard Earth Sciences Data and Information Services Center,
<https://disc.gsfc.nasa.gov/datasets?page=1&source=AQUA%20AIRS&keywords=airs%20version%206>

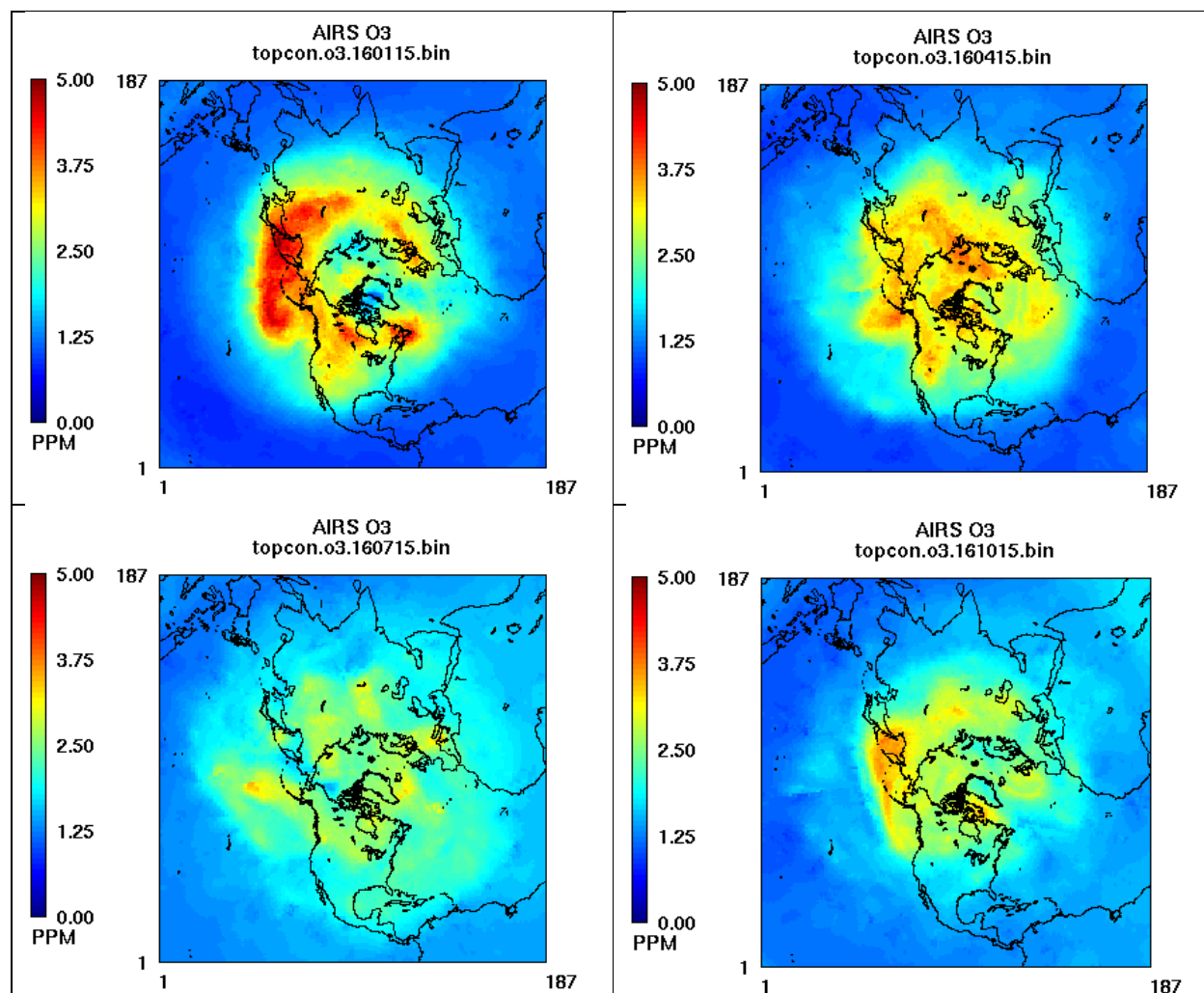


Figure 2-4. Daily H-CAMx ozone top concentrations derived from AIRS ozone retrievals at 50 mb. Individual plots are shown for January 15 (top left), April 15 (top right), July 15 (bottom left) and October 15 (bottom right).

period. Specifically, data from September 24 were used to fill missing areas on September 25; data from September 29 were used to fill missing areas on September 28; and averages of resulting fields on September 25 and 28 were used to fill September 26 and 27 (i.e., top BCs on the 26th and 27th are identical). Figure 2-5 shows the progression of the filling procedure.

We generated top BC input files for all days spanning October 1, 2015 to December 31, 2016, where the beginning date represents the start of our fourth quarter 2015 spin-up period from ICs. Ramboll delivered the AIRS2CAMxTC and AIRSaverage programs to TCEQ with operating instructions (see Task 2 report) so that they may process AIRS data for years other than 2016. All data processing activities were reviewed for quality assurance. This included independently checking program configurations and scripts, reviewing message files, and spot-checking resulting variable fields graphically for obvious problems or flaws.

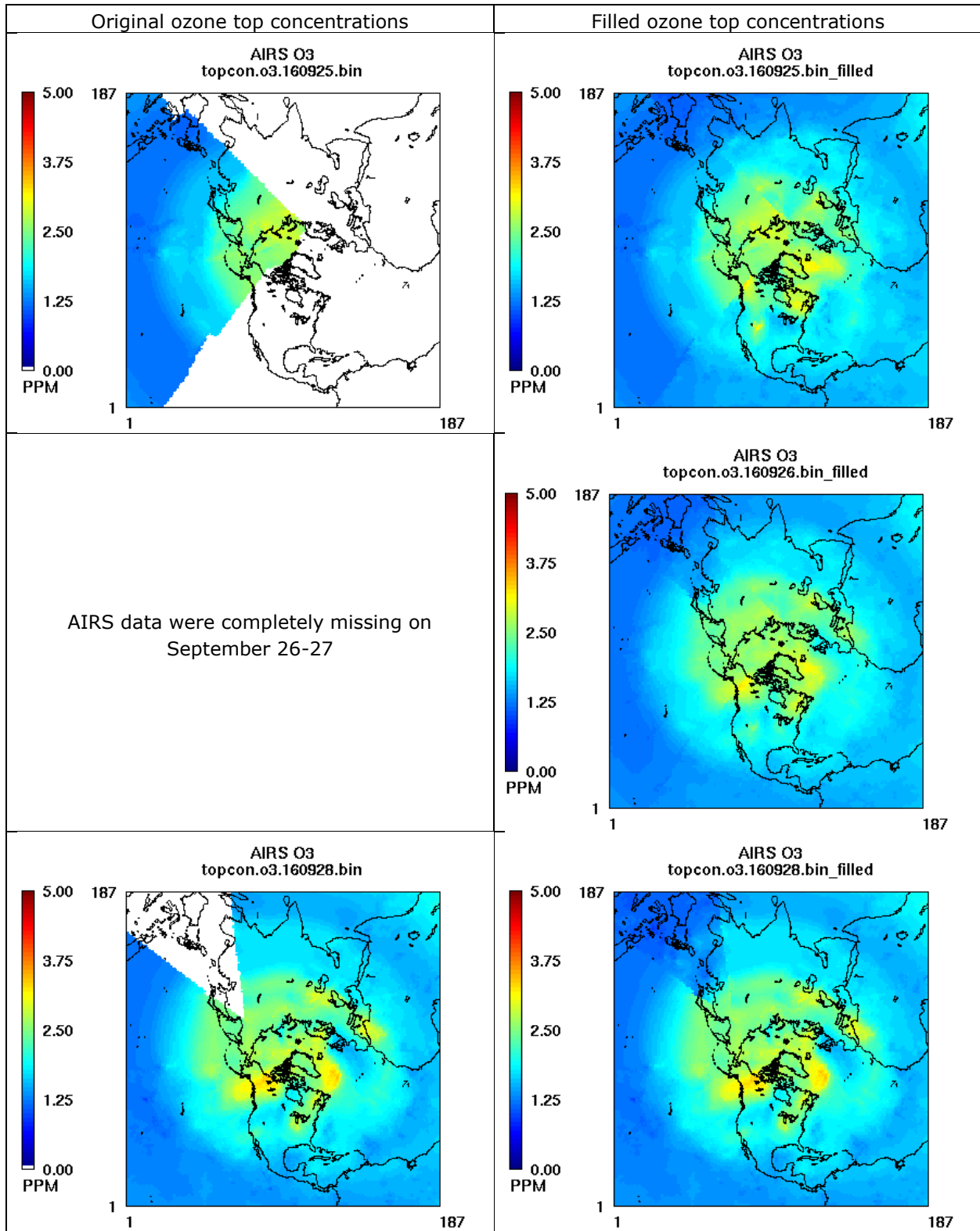


Figure 2-5. (Left) Original ozone top concentrations derived from AIRS 50 mb data on September 25-28 (top to bottom). (Right) Filled data fields for the same days. See text for details; filled top concentrations on the 26th and 27th are identical.

2.1.3 Initial and Lateral Boundary Concentrations

New considerations were necessary to address IC/BCs for ozone and other important and highly spatially/temporally variable compounds such as CO, NO_x, VOC and PM. These compounds are especially important when considering initial conditions, as we seek to characterize pollutant concentration distributions throughout the domain in a manner that reduces model spin-up times. Starting H-CAMx from simple profile assumptions that are out of chemical balance with each other would require excessive model spin-up of up to a year to achieve a chemically-equilibrated atmosphere.

Our initial thinking was to scale concentrations of these additional species from gridded AIRS ozone and/or CO data. However, this approach would result in little temporal or zonal variability in the lower troposphere where the AIRS data tend toward the monthly climatological a-priori. Additionally, we needed to develop scaling ratios to characterize the ~30 individual species that comprise VOC and PM. In the end, a rather complex procedure would be needed to reduce well-resolved CAMx-speciated concentration fields from GOES-Chem to simplistic, nearly time/space uniform IC/BCs, which ultimately would be similar to specifying climatological profiles as initially proposed. Therefore, we reverted back to GEOS-Chem data from which to develop a representative monthly set of spatially-varying IC/BCs for all species that may also be used for other years.

We developed a library of monthly-averaged ICs (three-dimensional) and lateral BCs (two-dimensional) for all CAMx species. This approach partially alleviates the dependence of H-CAMx on third-party global models because the monthly inputs can be used to represent a recent global climatology within a reasonable interval (arguably ± 5 years) from 2016. Therefore, it removes the need to run a global model for a specific H-CAMx simulation year within that period. Since these spatially-varying concentrations are model-derived, all species are chemically consistent with each other. We believe this solution provides the best balance among flexibility and representativeness and will allow for a shortened hemispheric spin-up period.

The development of the IC/BC library involved three steps. First, daily three-dimensional ICs and 3-hourly lateral BCs were extracted from the 2016 GEOS-chem global model output originally used in the FY19 H-CAMx project. We employed our Python tool called GEOS2AQM to read GEOS-Chem netCDF output, map chemical species to CB6r4/CF, horizontally interpolate data to the H-CAMx polar stereographic grid, vertically interpolate data to the H-CAMx layer structure (in terms of the WRF eta level definition), and generate H-CAMx IC/BC files in the new CAMx v7 netCDF input formats. The resulting daily IC files each included only a single timestamp corresponding to the first time in each GEOS-Chem output file. The daily BC files each included data every 3 hours. Second, these daily files were further postprocessed with the netCDF NCO operator tool⁵ to generate gridded, monthly averaged species concentrations. Third, the netCDF metadata records were modified to reflect a start time of January 1, 2000 (TFLAG) and an end time of January 1, 2050 (ETFLAG) so the files could be used for any simulation within that period.

These tools and scripts can be used to process any year of IC/BC data from GEOS-Chem. Although TCEQ will likely not need to run this tool for some time, we have delivered the tool with user instructions and can assist TCEQ with installing and testing it on their system. IC/BC data processing activities were reviewed for quality assurance. This included independently checking program configurations and scripts, reviewing message files, and spot-checking resulting variable fields graphically for obvious problems or flaws.

⁵ <http://nco.sourceforge.net/>

3.0 WRF SIMULATIONS

The availability of EPA’s single realization of 2016 hemispheric meteorological fields limited the FY19 project in two ways: inability to assess H-CAMx sensitivity to vertical resolution; and inability for H-CAMx to account for deep convective mixing, which is recognized as a significant vertical transport mechanism over the northern hemisphere that must be parameterized as a sub-grid process at 108 km grid scale. Employing the same version of WRF (v3.8; NCAR, 2017) as used by EPA, we first ran a replication of EPA’s configuration and then ran two alternative WRF configurations over the hemispheric grid for the year 2016, including a spin-up period for H-CAMx covering October 1 – December 31, 2015. Key changes in the WRF configuration included: (1) increasing vertical resolution in the mid-troposphere through the lower stratosphere to the extent that is similar to or better than the GOES-Chem global model (Harvard, 2020); (2) invoking the multi-scale Kain-Fritsch (MSKF; Zheng et al., 2016) sub-grid cumulus option, which supports the CAMx cloud-in-grid (CiG) convective sub-model. We then conducted a qualitative (graphical) comparison among our EPA replication run and our alternative WRF runs.

3.1 EPA WRF Configuration

The EPA’s configuration for their 2016 hemispheric WRF application followed from the original set of hemispheric runs reported by Mathur et al. (2017). We refer to this set of WRF data as “Run0”, and it was this dataset that we used in our FY19 H-CAMx modeling project and for the initial full annual H-CAMx run in this project. Table 3-1 lists the EPA’s WRF configuration.

Table 3-1. EPA 2016 hemispheric WRF v3.8 model configuration (Run0).

WRF Configuration Option	Selection
WRF version	3.8
Horizontal Resolution	108 km
Resolved Cloud Microphysics	Morrison
Longwave Radiation	Rapid Radiative Transfer Model for GCMs
Shortwave Radiation	RRTMG
Surface Layer Physics	Pleim-Xiu (P-X)
Land Surface Model (LSM)	P-X
Planetary Boundary Layer (PBL)	Asymmetric Convective Model, version 2 (ACM2)
Cumulus Parameterization	Kain-Fritsch (K-F)
Boundary and Initial Conditions Data Source	Global Forecast System (GFS) analysis
Observation Nudging	None
Analysis Nudging Coefficients (s^{-1})	
Winds	1×10^{-4} (above PBL only)
Temperature	1×10^{-4} (above PBL only)
Mixing Ratio	1×10^{-5} (above PBL only)
P-X Deep Soil Moisture/Temperature	On
Initialization	Single initialization from Dec 21, 2015

3.2 Ramboll WRF Configuration/Application Strategy

We configured our first WRF simulation (Run1) to replicate EPA’s Run0 as closely as possible but with one key difference: we ran the simulation as a series of independently initialized overlapping 5.5-day segments starting from October 1, 2015 instead of a single continuous year-long simulation from an initialization on December 21, 2015. EPA ran WRF as a single simulation to accommodate the continuous P-X deep soil nudging procedure, which benefits from a memory of soil moisture and

temperature throughout the run. Ramboll's segmented approach re-initialized deep soil moisture and temperature every 5 days from the input GFS analyses, which impacted near-surface model performance relative to Run0 to a certain extent. EPA ran their continuous WRF simulation in their high-performance computing center with hundreds of available cores connected via fast InfiniBand network. We estimated that running a single continuous WRF simulation over five quarters given the number of computer cores available on our system would have required at least a month to complete. Given that we had three WRF runs to conduct, our segmented parallelization approach allowed us to complete the replication run (Run1) and our two WRF sensitivity runs (Run2 and Run3) within a month.

3.2.1 Increased Vertical Resolution

Vertical resolution is important to resolve boundary layers, free tropospheric transport with minimal numerical diffusion, and stratosphere-troposphere exchange of ozone. Mathur et al. (2017) found much improved performance using 44 layers, particularly around the tropopause, and recommended the use of as many layers as practical to resolve the free troposphere and lower stratosphere. The 44 layers resolve the mid and upper troposphere with layer depths typically 500-700 m ($\Delta x/\Delta z \approx 150-200$) like the GEOS-Chem configuration of Eastham and Jacob (2017). However, this is less than the optimal range of 700-1500 later reported by Zhuang et al. (2017), which according to the authors better preserve intercontinental plume coherence up to a week or more. Based on the findings of Zhuang et al., vertical layers should be at most ~ 150 m thick in the mid-troposphere for horizontal resolution of $\sim 1^\circ$ (100 km).

WRF Run2 was identical to Run1 but with 9 additional layers to improve vertical resolution in the mid-troposphere through the lower stratosphere (5-10 km; Table 3-2). Our goal was to improve upper tropospheric resolution with a minimum of additional layers, which required some degradation of layer resolution near the surface. For example, in Run1 the lowest 12 layers span depths of 20-100 m up to about 600 m, whereas in Run2 the lowest 5 layers span depths of 100-150 m up to 650 m. In Run2, however, layers in the upper troposphere range 235-435 m (40-50% thinner than Run1) and lead to $\Delta x/\Delta z \approx 250-460$. We believe the tradeoff with thicker near-surface layers is acceptable since 20 m depths represent a false resolution given typical terrain variability over 108 km scale and the fact that boundary layer mixing tightly couples layers in the lower PBL. More importantly at global scales, higher resolution aloft better resolves jet streams, and should minimize numerical diffusion of transported plumes aloft and improve the characterization of tropopause folding and associated stratospheric intrusions.

3.2.2 Multi-Scale Kain-Fritsch Convection

The configuration of WRF Run3 was based on Run2 but replaced the K-F sub-grid convective scheme with the MSKF scheme. As shown in Table 3-3, the choice of MSKF also required the use of the Yonsei University (YSU) PBL parameterization, which in turn required the use of the MM5 surface layer physics. All three changes are potentially important deviations from EPA's configuration and could alter near-surface WRF wind, temperature and humidity fields to a certain extent.

3.3 Results

We conducted a qualitative comparison of wind speed, temperature and humidity fields over the modeling domain at two levels (near-surface and near-tropopause) and for two months (January and July) among the four WRF runs. Figures 3-1 through 3-12 display graphical results of monthly-average variable fields: Figures 3-1 through 3-4 compare Run0 (EPA run) and Run1 (our replication of EPA's configuration); Figures 3-5 through 3-8 compare Run1 and Run2 (additional layers); and Figures 3-9 through 3-12 compare Run2 and Run3 (MSKF with YSU and MM5 schemes). Plots comparing

Table 3-2. Vertical layer structures for EPA and Ramboll WRF simulations. EPA Run0 and Ramboll Run1 are shown in the left 5 columns; Ramboll Run2 and Run3 are shown in the right 5 columns.

Layer	eta	Pressure (mb)	Height (m)	Thickness (m)		Layer	eta	Pressure (mb)	Height (m)	Thickness (m)
44	0.0000	50	20576	1943		53	0.0000	50	20576	2203
43	0.0186	67	18632	1583		52	0.0216	70	18372	1631
42	0.0386	87	17049	1323		51	0.0431	91	16741	1296
41	0.0596	107	15726	1141		50	0.0647	112	15444	1076
40	0.0816	128	14584	1012		49	0.0862	133	14368	919
39	0.1047	150	13572	911		48	0.1078	153	13449	803
38	0.1289	174	12661	833		47	0.1293	174	12646	712
37	0.1543	198	11827	772		46	0.1509	195	11933	640
36	0.1810	224	11055	724		45	0.1724	216	11292	583
35	0.2089	251	10331	698		44	0.1940	236	10709	459
34	0.2383	279	9633	670		43	0.2122	254	10250	434
33	0.2690	309	8963	651		42	0.2304	271	9815	412
32	0.3013	340	8311	633		41	0.2485	289	9403	392
31	0.3352	372	7678	618		40	0.2667	306	9010	374
30	0.3708	407	7059	604		39	0.2849	324	8636	358
29	0.4081	443	6455	566		38	0.3031	342	8277	344
28	0.4454	479	5889	532		37	0.3213	359	7932	330
27	0.4827	515	5356	503		36	0.3395	377	7602	318
26	0.5200	550	4853	477		35	0.3576	394	7283	307
25	0.5573	586	4375	454		34	0.3758	412	6975	297
24	0.5946	622	3921	434		33	0.3940	429	6678	287
23	0.6320	658	3486	414		32	0.4122	447	6391	278
22	0.6693	694	3071	397		31	0.4304	464	6113	270
21	0.7066	730	2674	382		30	0.4485	482	5842	262
20	0.7439	766	2291	351		29	0.4667	499	5580	254
19	0.7795	800	1940	295		28	0.4849	517	5325	248
18	0.8104	830	1645	250		27	0.5031	534	5077	241
17	0.8373	856	1394	212		26	0.5213	552	4836	235
16	0.8607	879	1182	181		25	0.5395	569	4601	235
15	0.8810	898	1001	155		24	0.5578	604	4417	218
14	0.8987	915	845	133		23	0.5940	622	3928	214
13	0.9141	930	712	114		22	0.6122	639	3714	209
12	0.9275	943	598	98		21	0.6304	657	3505	204
11	0.9391	954	500	84		20	0.6485	674	3300	200
10	0.9492	964	415	73		19	0.6667	692	3099	196
9	0.9580	972	342	63		18	0.6849	709	2903	192
8	0.9657	980	278	54		17	0.7031	727	2710	188
7	0.9723	986	224	47		16	0.7213	744	2522	185
6	0.9781	992	177	40		15	0.7395	762	2336	181
5	0.9831	997	136	35		14	0.7576	779	2154	178
4	0.9875	1001	100	30		13	0.7758	797	1976	175
3	0.9913	1004	70	26		12	0.7940	814	1800	172
2	0.9946	1008	43	23		11	0.8122	832	1628	169

Layer	eta	Pressure (mb)	Height (m)	Thickness (m)		Layer	eta	Pressure (mb)	Height (m)	Thickness (m)
1	0.9975	1010	20	20		10	0.8304	849	1458	166
0	1.0000	1013	0	0		9	0.8485	867	1292	164
						8	0.8667	884	1128	161
						7	0.8849	902	966	158
						6	0.9031	919	807	156
						5	0.9213	937	651	154
						4	0.9395	954	497	151
						3	0.9576	972	345	149
						2	0.9758	990	195	99
						1	0.9880	1001	96	96
						0	1.0000	1013	0	0

Table 3-3. WRF physics options used in Run0 through Run3.

WRF Physics	Run0/1/2	Run3
Surface Layer Physics	P-X	MM5
PBL	ACM2	YSU
Sub-Grid Convection	K-F	MSKF

“near-surface” fields are extracted from WRF layer 11 (Run0 and Run1) and layer 4 (Run2 and Run3), which are at roughly 500 m MSL or 950 mb over oceans. We did not plot pressure-level data per se as 950 mb extends below topography over continents. By evaluating model differences slightly above the surface layer, we smooth out spuriously large details in surface conditions that may occur between simulations and better accommodate differing model layer structures. Plots comparing near-tropopause fields are extracted from the WRF layers 33 and 41, respectively, which contain the 300 mb pressure level (roughly 9 km MSL) where jet stream winds are often at peak strength.

Comparing EPA’s results and our replication in Run1 (Figures 3-1 through 3-4), small differences are apparent in the January and July monthly averaged fields, both near the surface and aloft, as expected. The largest differences occur for near-surface temperature and humidity. In January, portions of the continents are slightly warmer by ~0.5 C and sub-tropical areas of Africa and India are slightly drier. In July, the continents exhibit more widespread patterns of slightly warmer and cooler areas while larger areas exhibit drier conditions. These differences in near-surface humidity and temperature are likely related to our parallelization over individual 5-day simulation periods, causing discontinuities in the soil moisture nudging.

We find larger differences among winds, temperature and humidity between Run1 and Run2 (Figures 3-5 through 3-8). Run2 near-surface fields are cooler and drier, whereas high-latitude areas are warmer in the winter where there is snow and ice cover. Near-surface winds are slightly stronger in equatorial and mid-latitude regions. These differences are consistent with expectations because of the deeper layers resolving the lower PBL in Run2. Aloft, jet stream speeds are higher by an average of a couple of meters per second, and temperatures are cooler across the domain by 1-2 C (humidity is very low at such altitudes and differences are below the resolution of the color scale). As expected, the Run2 layer structure aloft leads to better resolution of the jet stream’s vertical structure and thus higher speeds. It also improves resolution of the temperature profile near the tropopause, leading to lower temperatures than the temperature resolved by thicker layers in Run1.

Relative to Run2, Run3 with modified sub-grid convection, PBL and surface layer schemes leads to slightly stronger near-surface winds in the equatorial convergence zone in both seasons, and slightly weaker mid-latitude winds in winter (Figures 3-9 through 3-12). January near-surface temperatures are slightly cooler over the subtropical oceans and slightly warmer over sub-Saharan Africa, while subtropical July temperatures tend to be cooler globally (especially Africa and India). Near-surface humidity tends to be higher in these same areas and in both seasons indicating effects from the alternative mixing and surface layer schemes, and perhaps from modified sub-grid precipitation, at equatorial and sub-tropical latitudes. Very little near-surface impacts occur in mid or higher latitudes or at tropopause altitudes, as expected given the low-altitude/low-latitude sensitivity to PBL and cumulus mixing.

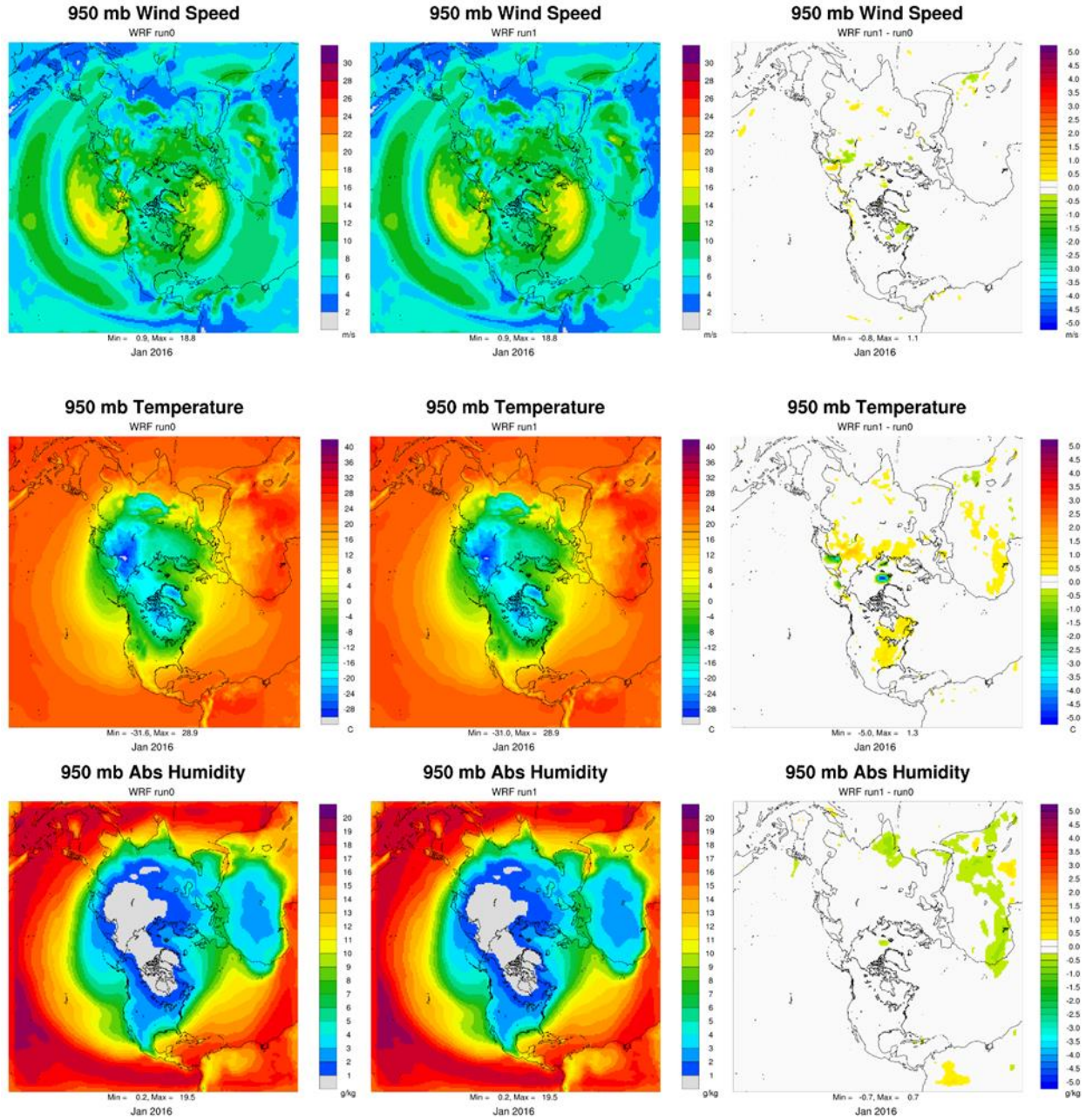


Figure 3-1. Comparisons of January-average near-surface wind speed (top row), temperature (middle row) and absolute humidity (bottom row) between WRF Run0 (left), Run1 (middle) and their differences (right). Fields are extracted from the WRF layer containing 950 mb over oceans.

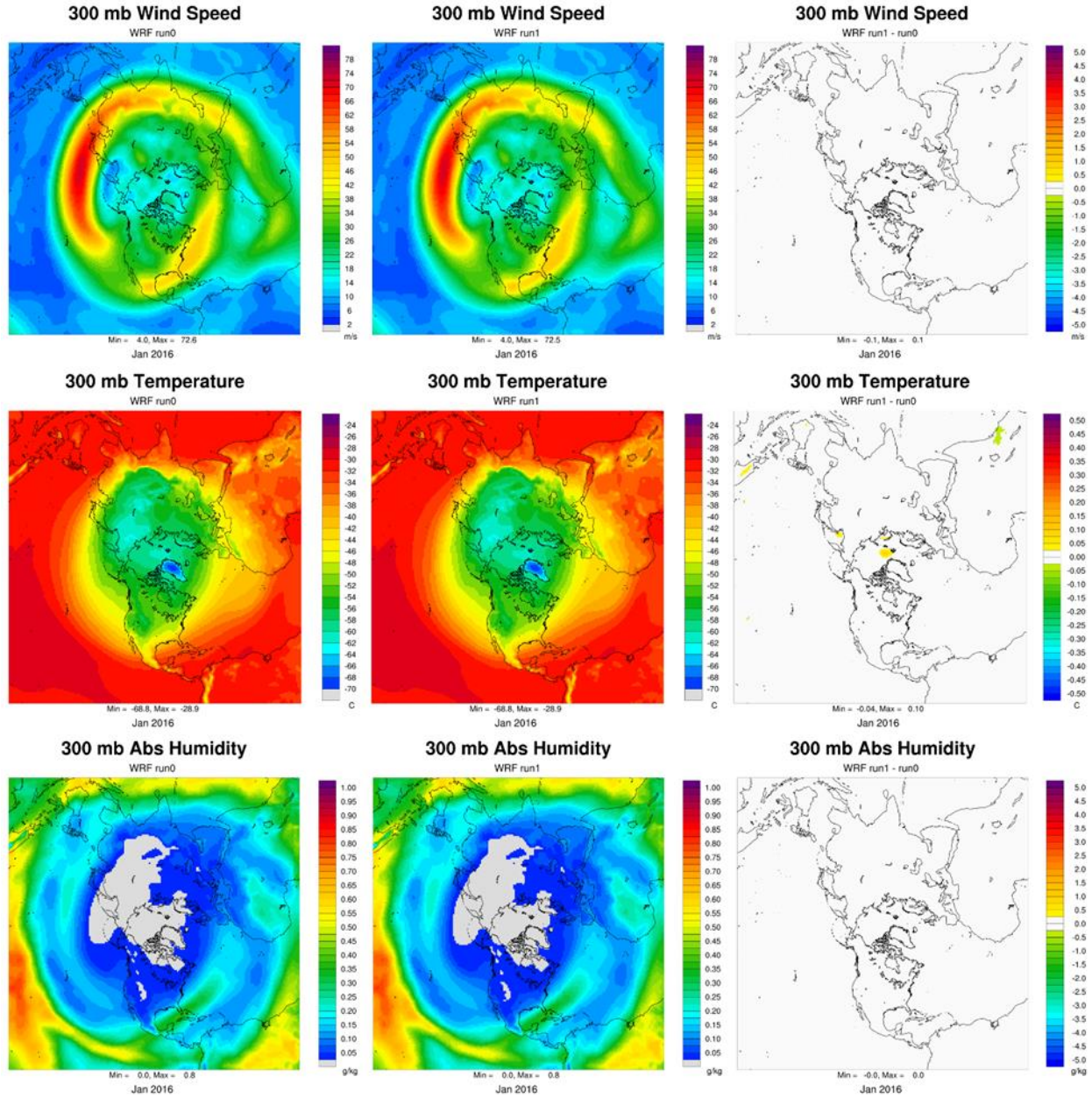


Figure 3-2. Comparisons of January-average near-tropopause wind speed (top row), temperature (middle row) and absolute humidity (bottom row) between WRF Run0 (left), Run1 (middle) and their differences (right). Fields are extracted from the WRF layer containing 300 mb over oceans.

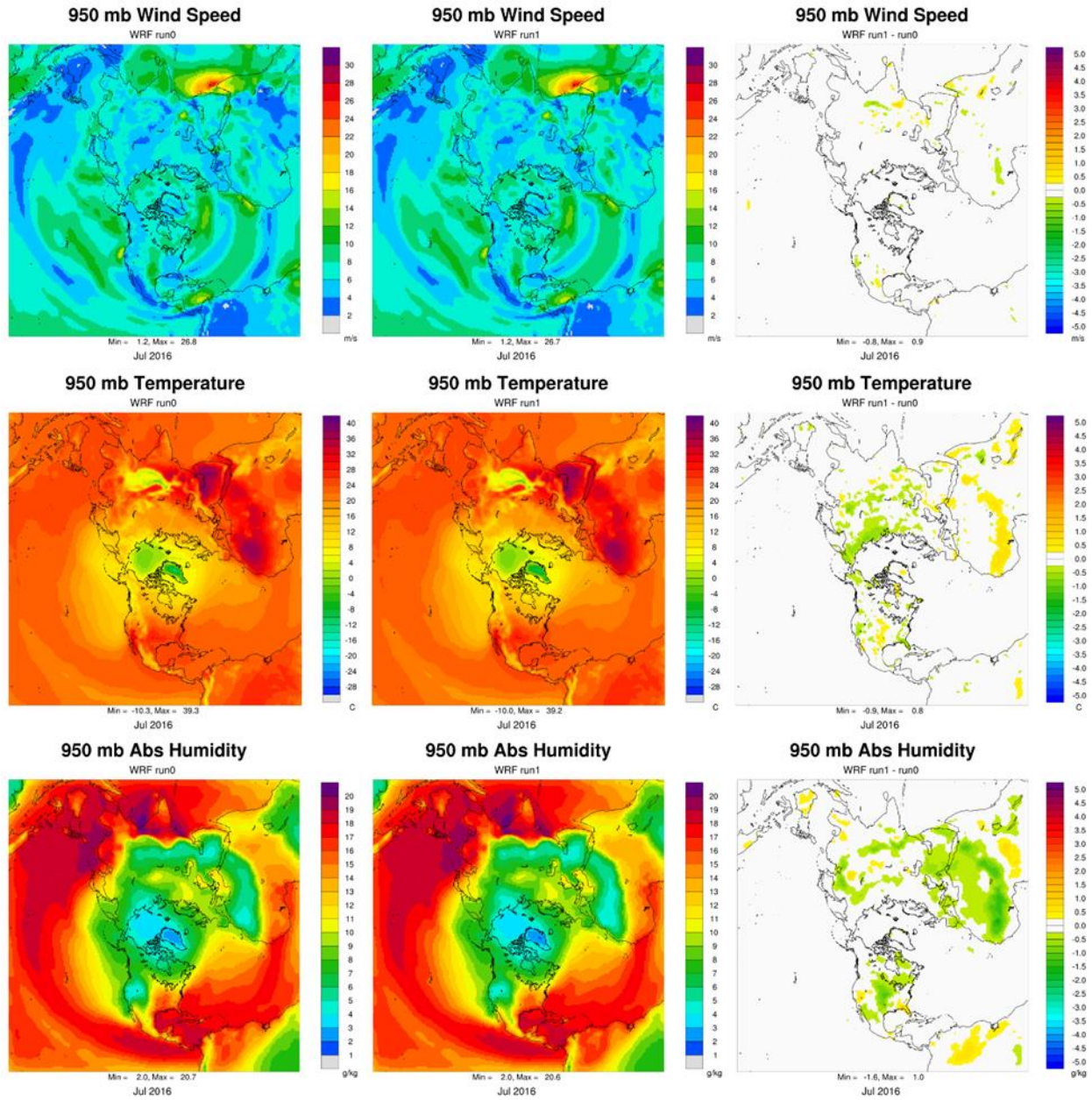


Figure 3-3. Comparisons of July-average near-surface wind speed (top row), temperature (middle row) and absolute humidity (bottom row) between WRF Run0 (left), Run1 (middle) and their differences (right). Fields are extracted from the WRF layer containing 950 mb over oceans.

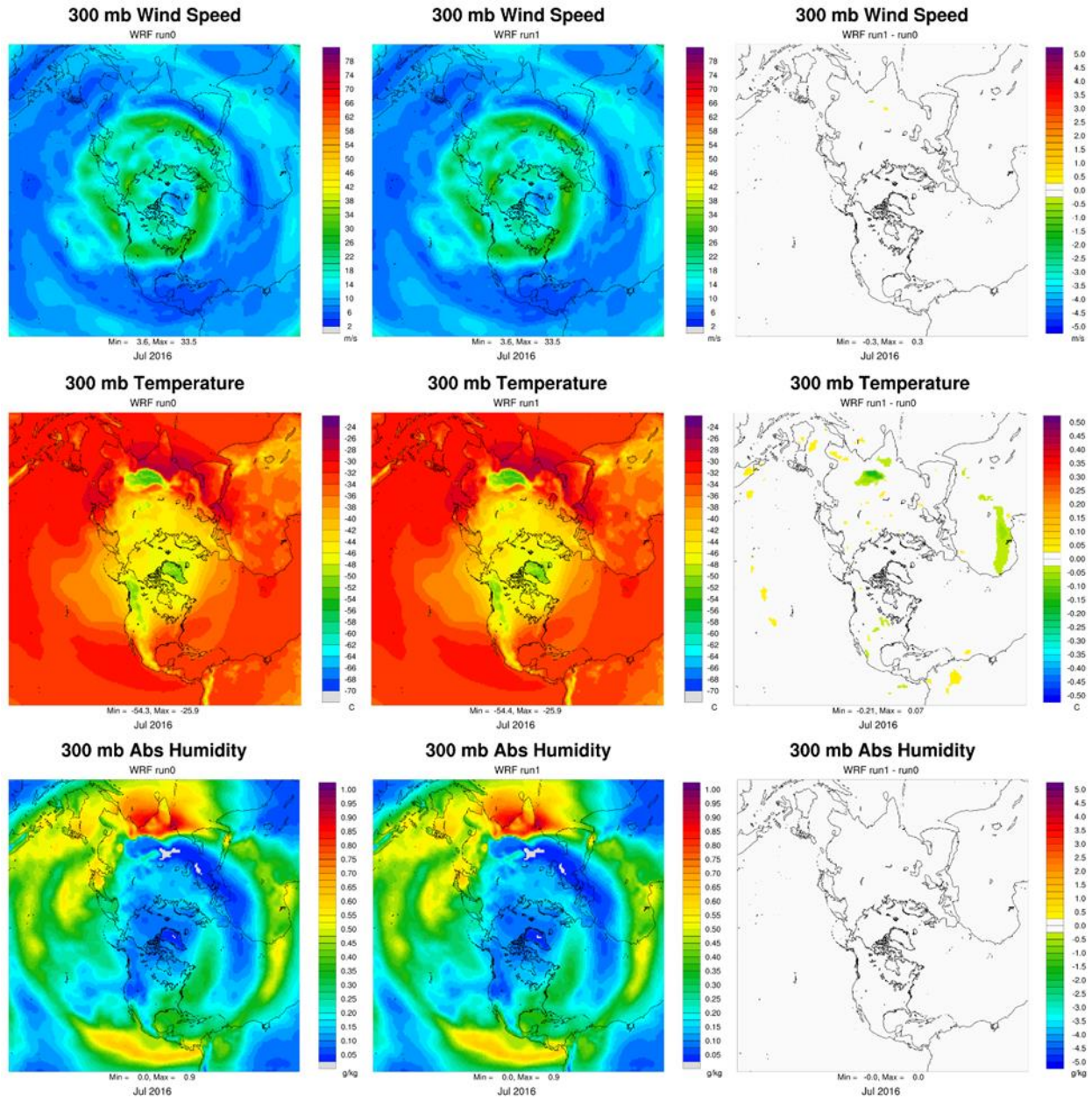


Figure 3-4. Comparisons of July-average near-tropopause wind speed (top row), temperature (middle row) and absolute humidity (bottom row) between WRF Run0 (left), Run1 (middle) and their differences (right). Fields are extracted from the WRF layer containing 300 mb over oceans.

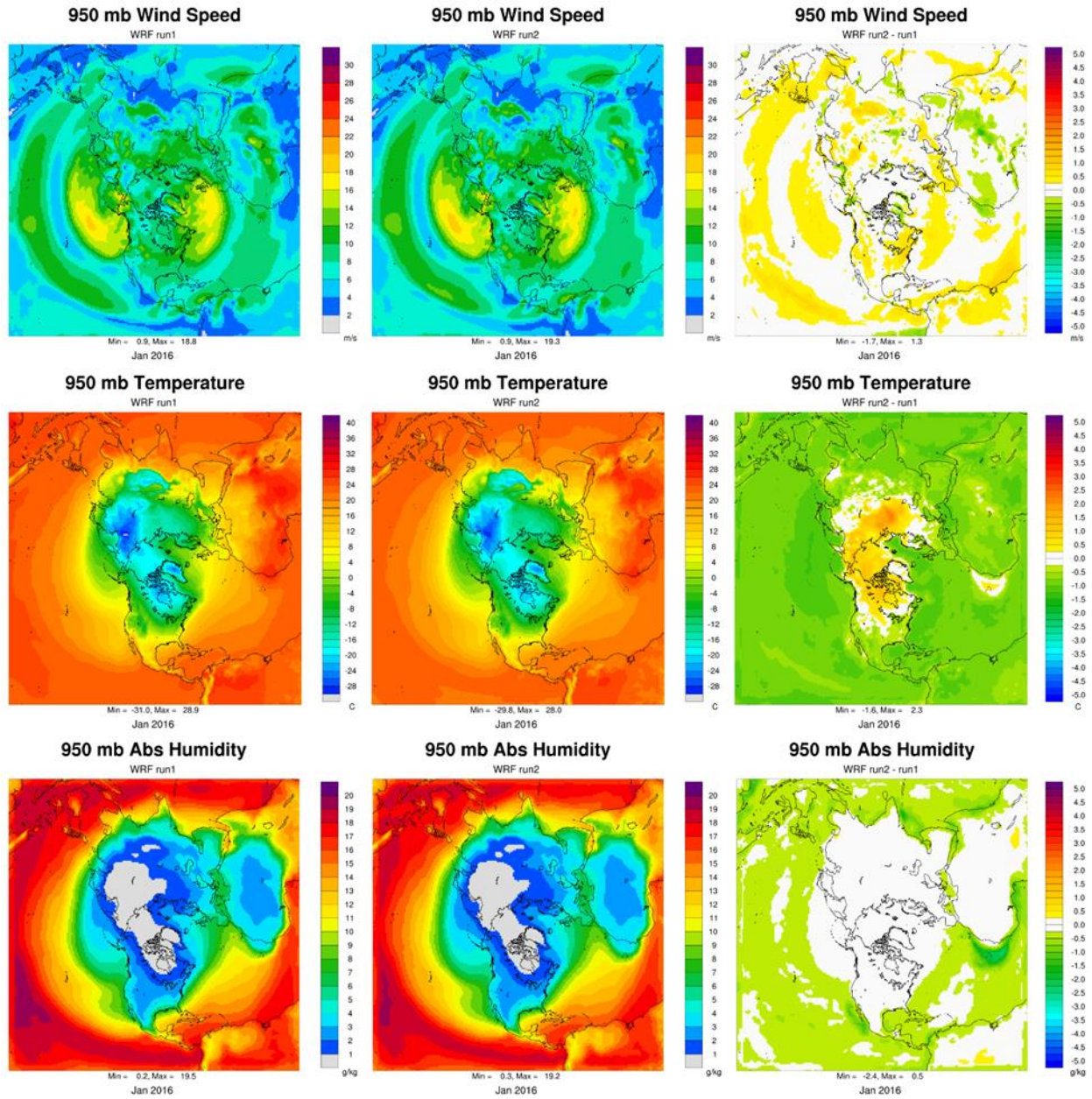


Figure 3-5. Comparisons of January-average near-surface wind speed (top row), temperature (middle row) and absolute humidity (bottom row) between WRF Run1 (left), Run2 (middle) and their differences (right). Fields are extracted from the WRF layer containing 950 mb over oceans.

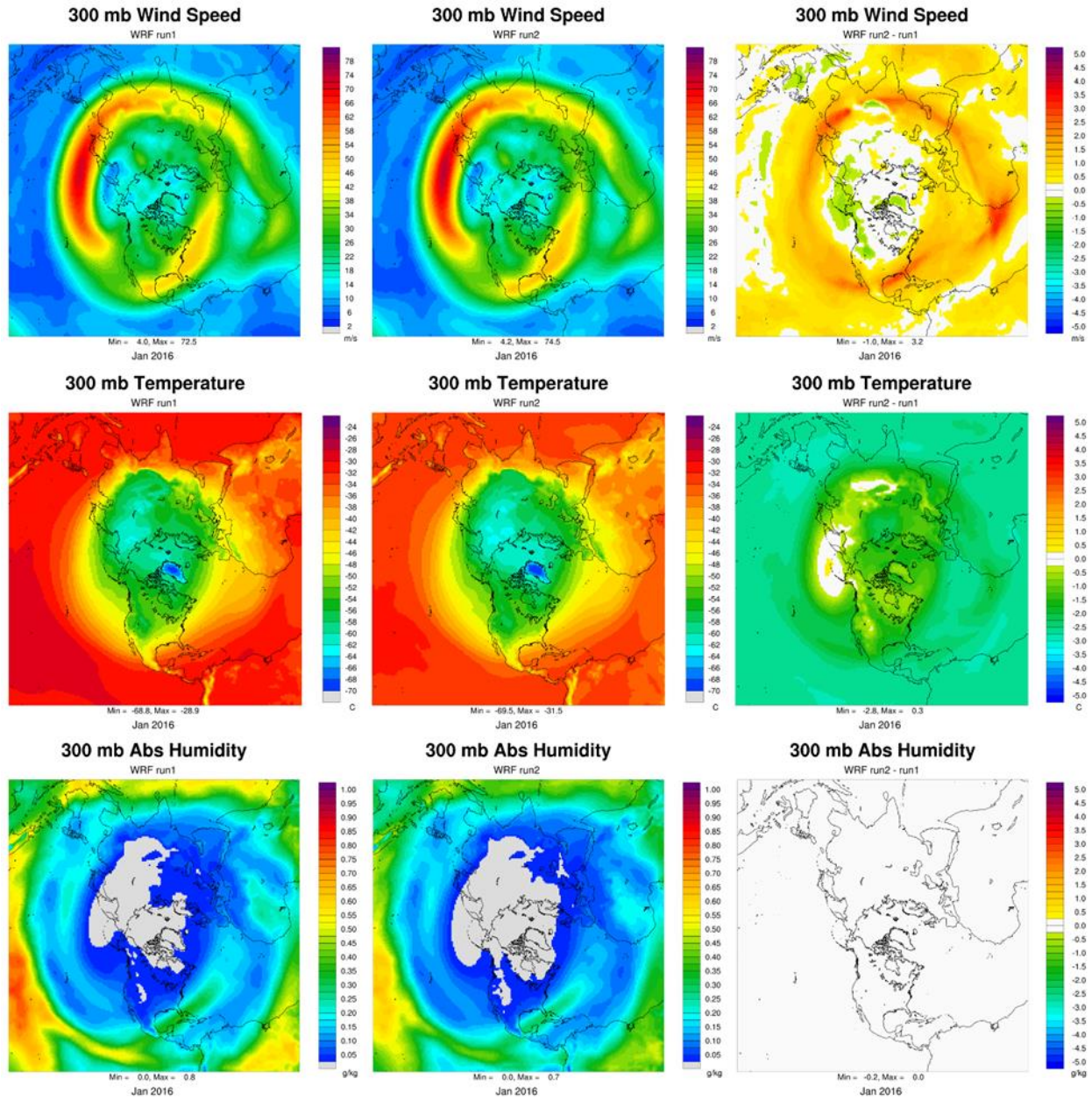


Figure 3-6. Comparisons of January-average near-tropopause wind speed (top row), temperature (middle row) and absolute humidity (bottom row) between WRF Run1 (left), Run2 (middle) and their differences (right). Fields are extracted from the WRF layer containing 300 mb over oceans.

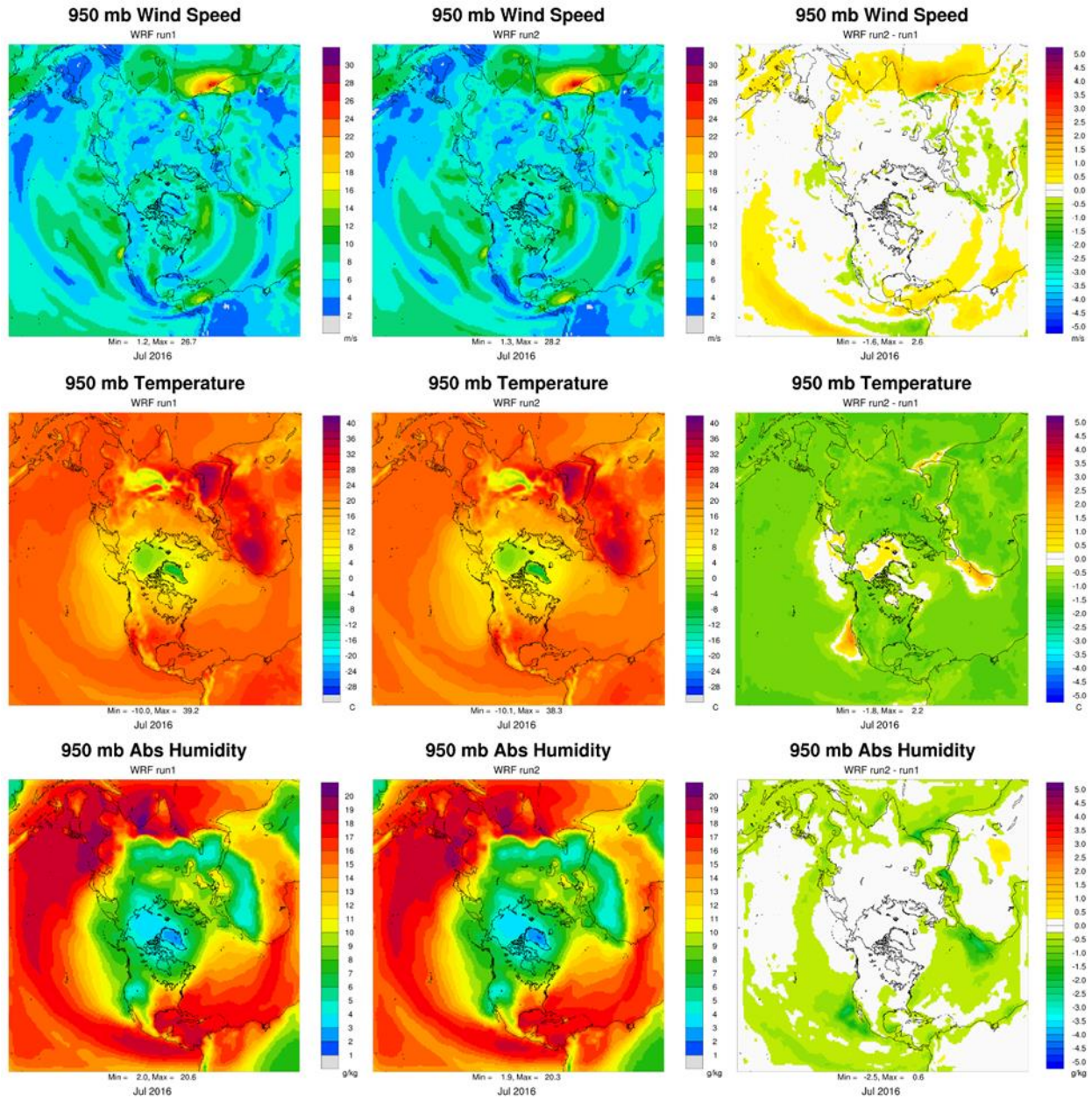


Figure 3-7. Comparisons of July-average near-surface wind speed (top row), temperature (middle row) and absolute humidity (bottom row) between WRF Run1 (left), Run2 (middle) and their differences (right). Fields are extracted from the WRF layer containing 950 mb over oceans.

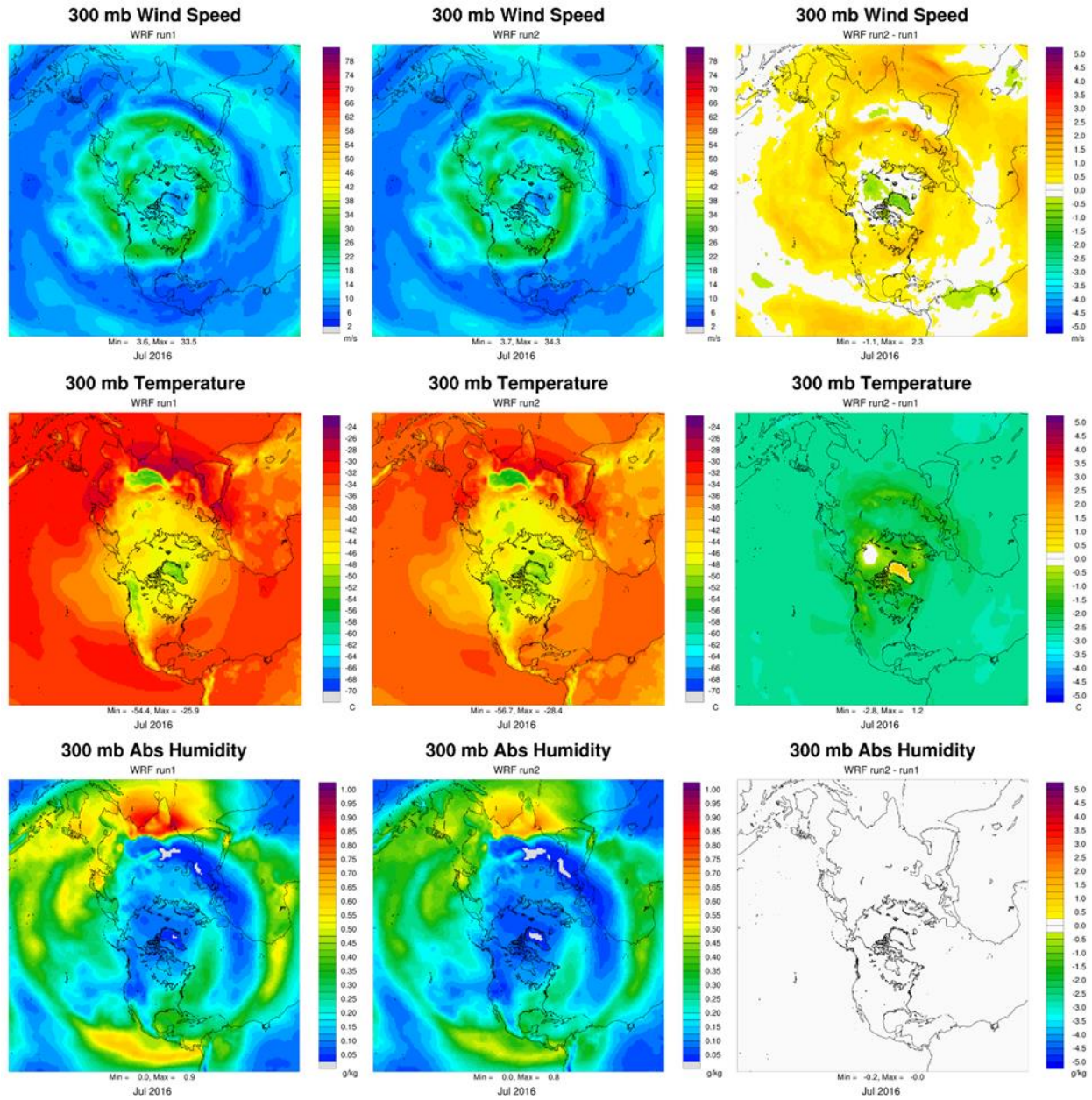


Figure 3-8. Comparisons of July-average near-tropopause wind speed (top row), temperature (middle row) and absolute humidity (bottom row) between WRF Run1 (left), Run2 (middle) and their differences (right). Fields are extracted from the WRF layer containing 300 mb over oceans.

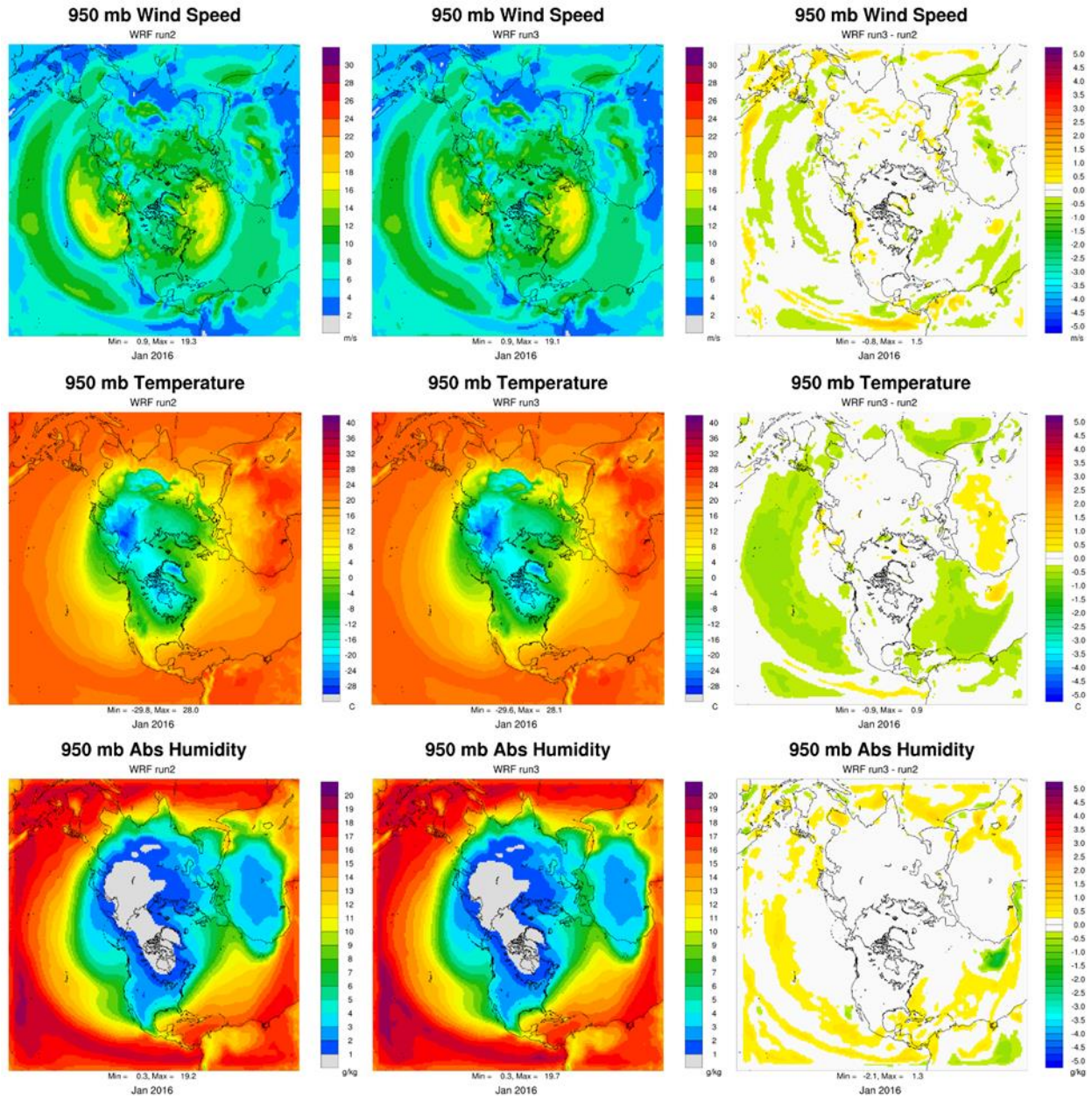


Figure 3-9. Comparisons of January-average near-surface wind speed (top row), temperature (middle row) and absolute humidity (bottom row) between WRF Run2 (left), Run3 (middle) and their differences (right). Fields are extracted from the WRF layer containing 950 mb over oceans.

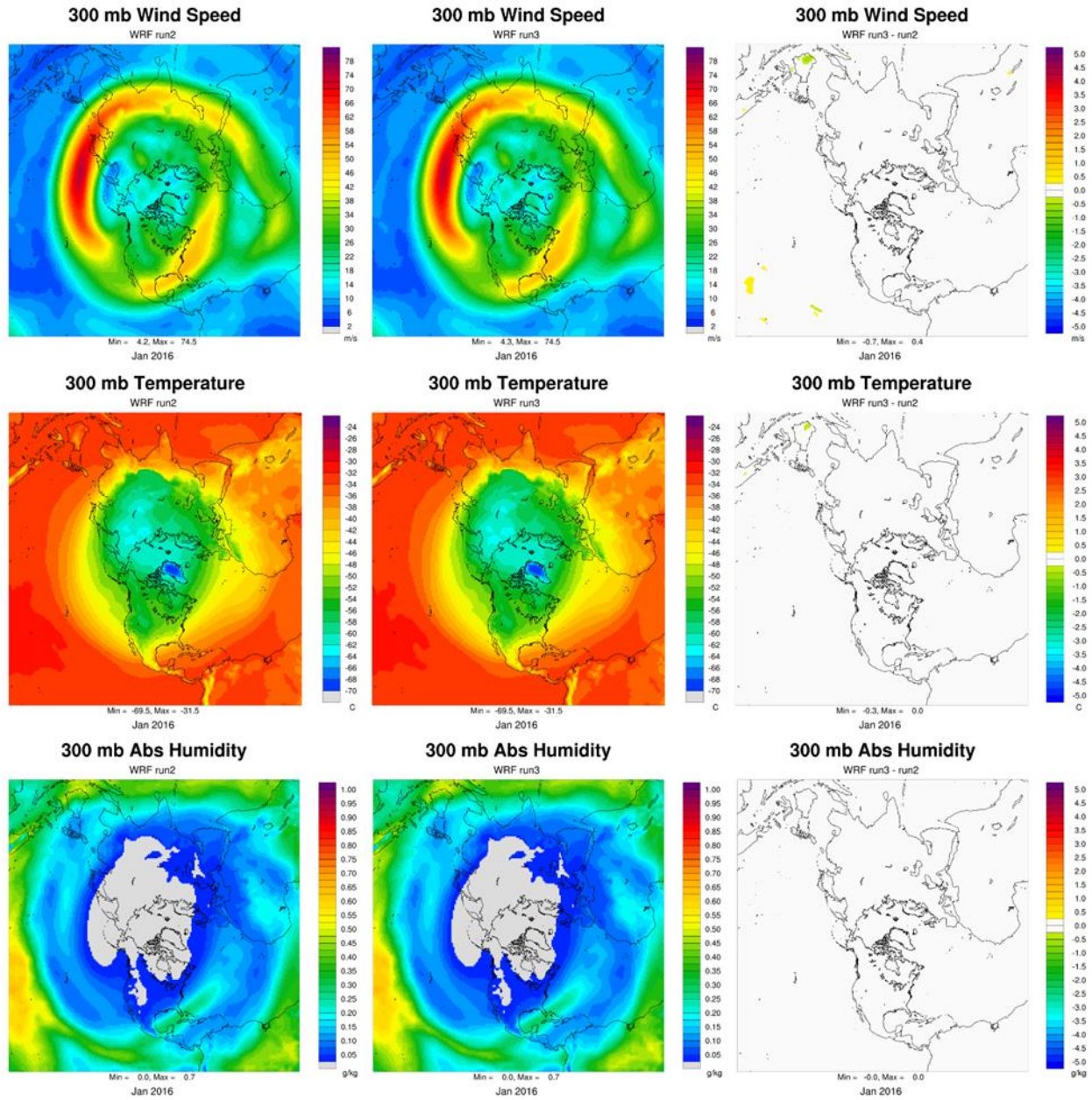


Figure 3-10. Comparisons of January-average near-tropopause wind speed (top row), temperature (middle row) and absolute humidity (bottom row) between WRF Run2 (left), Run3 (middle) and their differences (right). Fields are extracted from the WRF layer containing 300 mb over oceans.

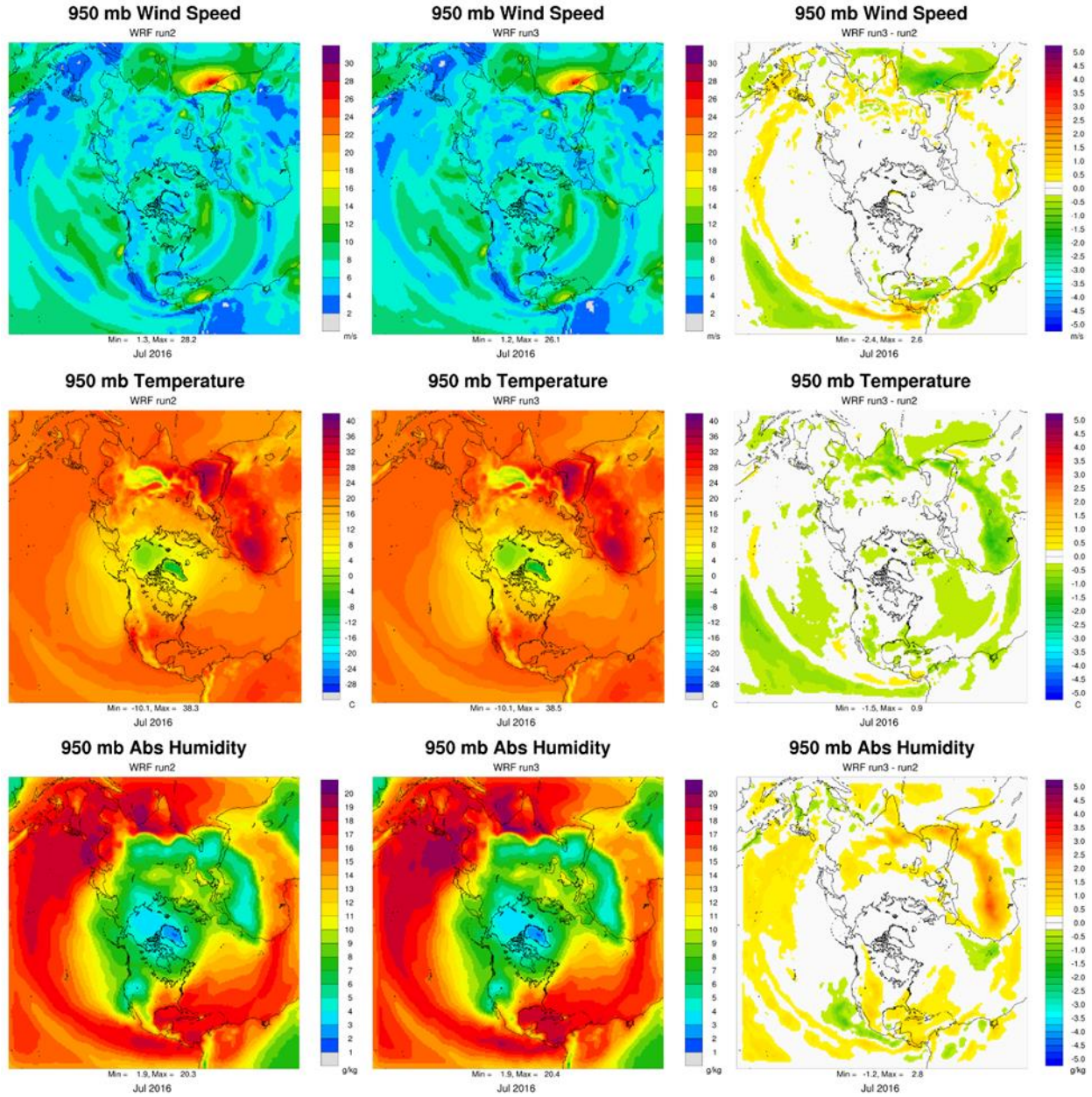


Figure 3-11. Comparisons of July-average near-surface wind speed (top row), temperature (middle row) and absolute humidity (bottom row) between WRF Run2 (left), Run3 (middle) and their differences (right). Fields are extracted from the WRF layer containing 950 mb over oceans.

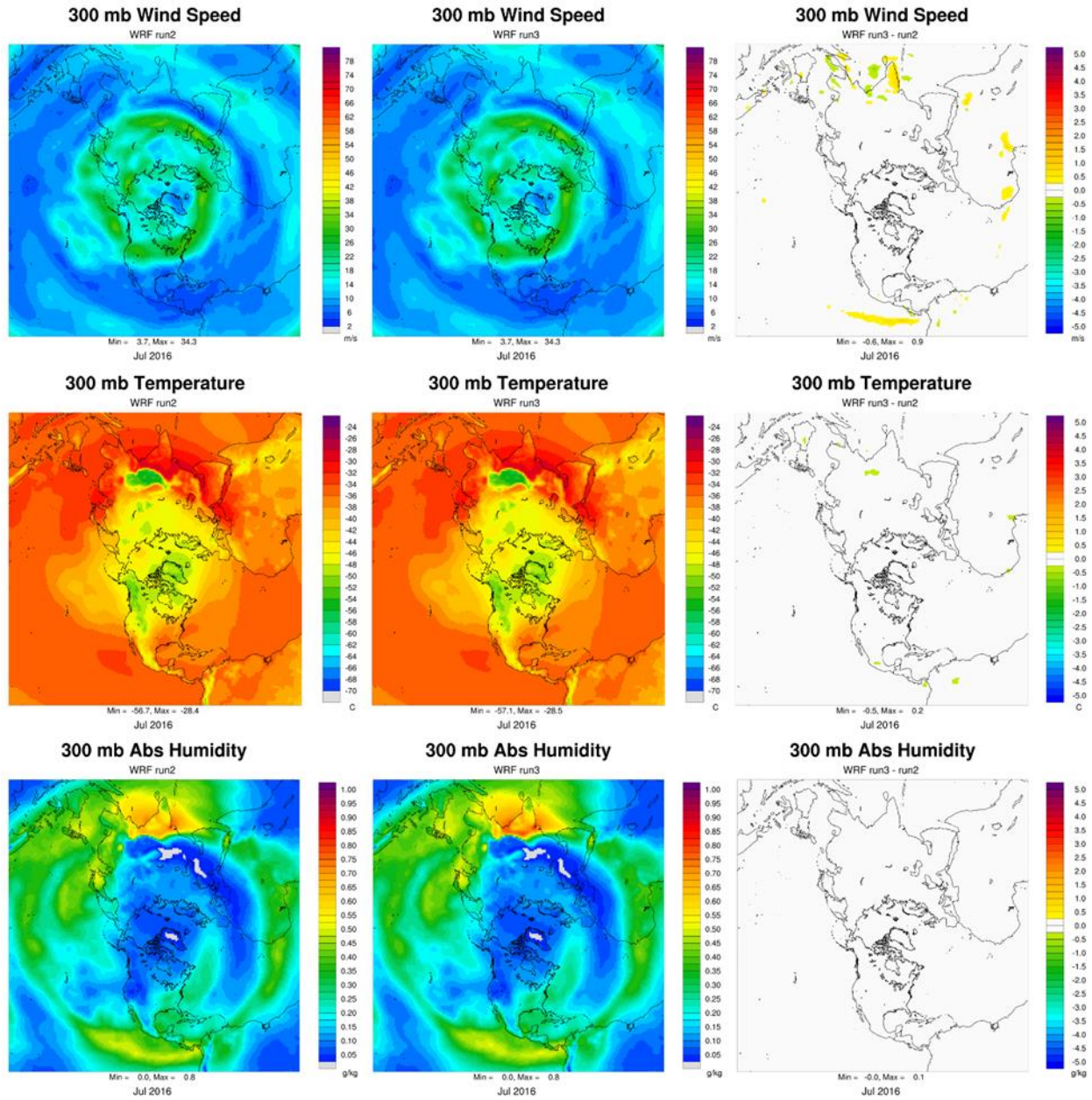


Figure 3-12. Comparisons of July-average near-tropopause wind speed (top row), temperature (middle row) and absolute humidity (bottom row) between WRF Run2 (left), Run3 (middle) and their differences (right). Fields are extracted from the WRF layer containing 300 mb over oceans.

4.0 H-CAMx SENSITIVITY TESTING AND PERFORMANCE EVALUATION

4.1 Configurations for Annual 2016 H-CAMx Runs

The FY19 modeling was run for the period of May-September 2016, with the month of April serving as a spin-up period from initial conditions. Table 4-1 lists the new H-CAMx cases developed in the current project. Ramboll first expanded the original H-CAMx simulation to the full year of 2016 (Run0), including a brief spin up period over December 2015 from initial conditions derived by the same GEOS-Chem output as used in the FY19 project. All sources of input data remained consistent with the FY19 project with no modifications, thereby establishing our baseline simulation. We compared Run0 performance against observed vertical ozonesonde profiles and surface ozone monitoring data, as well as to existing output from our 2016 GEOS-Chem run and EPA’s 2016 H-CMAQ run (described below).

Table 4-1. List and description of H-CAMx simulations conducted in this project.

H-CAMx Run	Description/Inputs
Run0	As in FY19 modeling, expanded to full 2016 year with December 2015 spin up: <ul style="list-style-type: none"> • EPA-derived WRF meteorology; with deep cloud Kv patching • EPA-derived global anthropogenic, biogenic, fire, and lightning NOx emissions • Ramboll-derived natural emissions (oceanic, windblown dust) • Ramboll-derived hourly, day-specific IC/BC from GEOS-Chem • Ramboll-derived photolysis input files • H-CAMx stratospheric ozone parameterization developed in FY19 project
Run1	As in Run0, but expanded to October 2015-December 2016: <ul style="list-style-type: none"> • Ramboll-generated WRF meteorology • Monthly-averaged IC and lateral BC from GEOS-Chem • Satellite-derived daily ozone top BC • Updated natural emissions (oceanic, windblown dust) for new meteorology and extended photolysis inputs over longer spin-up period • Minor updates to stratospheric ozone treatment to reduce consistent ozone bias above 10 km.
Run2	As in Run1, but: <ul style="list-style-type: none"> • New WRF meteorology with expanded vertical grid (44 to 53 layers) • Re-extracted monthly IC and lateral BC from GEOS-Chem for new vertical grid
Run3	As in Run2, but: <ul style="list-style-type: none"> • Modified WRF configuration to use Multi-Scale Kain-Fritsch (MSKF) sub-grid convection algorithm, YSU boundary layer and MM5 surface layer schemes • Invoked CAMx Cloud-in-Grid mixing scheme • Modified Kv inputs to remove deep cloud patching to avoid double-counting of cloud mixing

H-CAMx Run1 represents a new 2016 annual model configuration using Ramboll’s new IC/BC input fields as described in Section 2, and Ramboll’s run of WRF as described in Section 3. The grid configuration remained identical to Run0 but the spin-up period was extended back to October 2015 to allow for a full quarter of H-CAMx spin-up time prior to January 1, 2016. Ramboll-generated ozone top BCs and natural emissions (oceanic and windblown dust) were developed to span October 2015 – December 2016. ICs, lateral BCs and other emission inputs for the spin-up period were taken from

the coinciding dates in 2016. A minor update to the stratospheric ozone treatment was introduced in Run1, as further detailed below.

H-CAMx Run2 was identical to Run1 but involved a new WRF run that expanded the vertical grid system from 44 layers to 53 layers. IC and lateral BC inputs were reextracted from GEOS-Chem for the new layer structure and reprocessed to monthly averages, as described in Section 2, but otherwise unmodified. No other inputs were modified.

H-CAMx Run3 was identical to Run2 but involved changes to the WRF sub-grid convective algorithm and surface/boundary layer schemes to support the CAMx Cloud-in-Grid (CiG) mixing parameterization. CiG was invoked in this run while vertical patching of vertical diffusivity (Kv) to account for clouds was removed to avoid double-counting effects of cloud mixing. No other inputs were modified.

In all cases, we applied H-CAMx on a dual 14-core hyperthreaded Linux workstation (56 physical and virtual cores total). The 2015 spin-up period and the entire year of 2016 was run sequentially for each case. It was therefore important to minimize runtimes for such a long model integration. We assessed single-day model runtimes for several combinations of distributed-memory Message Passing Interface (MPI) and shared-memory Open Multi-Processor (OMP) parallelization. We found that a combination of 9 MPI cores (1 master, 8 workers) by 6 OMP threads (48 worker virtual cores total) resulted in the fastest runtime for the test day: 13 minutes. We applied this combination for all H-CAMx runs. Table 4-2 presents total H-CAMx run times for each of the scenarios evaluated in this project.

Table 4-2. Runtimes for each H-CAMx scenario using the parallelization noted in the text and the model configuration listed in Table 4-1.

H-CAMx Run	Run Duration	Run Dates (Total # Days)
Run0	4 days, 11 hr, 46 mins	12/22/2015 - 12/30/2016 (375 days)
Run1	5 days, 3 hr, 46 mins	10/01/2015 - 12/31/2016 (458 days)
Run2	5 days, 23 hrs 21 mins	10/01/2015 - 12/31/2016 (458 days)
Run3	6 days, 9 hr, 15 mins	10/01/2015 - 12/31/2016 (458 days)

All modeling activities were reviewed for quality assurance. This included independently checking program configurations and scripts, reviewing message files, and spot-checking resulting variable fields graphically for obvious problems or flaws.

4.2 Global Measurement Data Selection

4.2.1 Surface Ozone Measurements

4.2.1.1 World Data Centre for Reactive Gases

The World Data Centre for Reactive Gases (WDCRG)⁶ is part of the World Meteorological Organization's (WMO) Global Atmosphere Watch (GAW)⁷ program, and consists of a data repository and archive for global monitoring of ambient gas concentrations. The archive includes SO₂, oxidized nitrogen species (NO_x), ozone and volatile organic compounds (VOCs). Ramboll used ozone data for

⁶ <https://www.gaw-wdcrq.org/>

⁷ <https://community.wmo.int/activity-areas/gaw>

the H-CAMx model performance evaluation (MPE). We accessed the data through a dissemination website operated by the Norwegian Institute for Air Research (NILU)⁸. Figure 4-1 shows the northern hemispheric WDCRG monitor locations that include surface ozone data. Note that there are a large number of sites in Europe (~25), several in remote northern latitudes, several across east Asia, a few in oceanic areas, and two in the conterminous US.

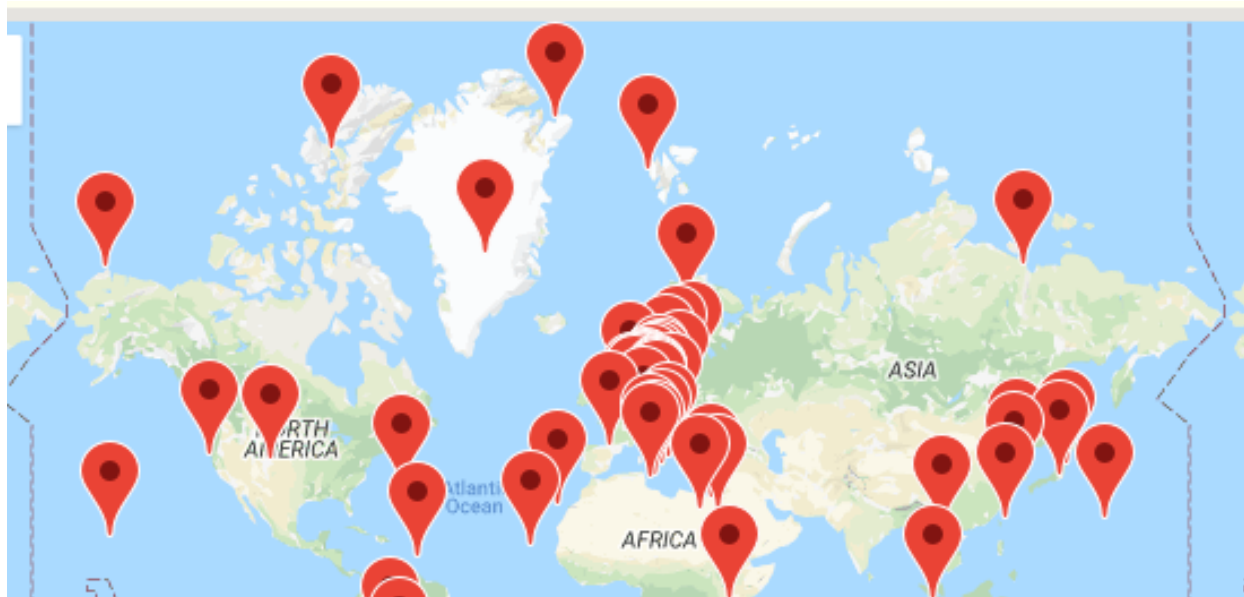


Figure 4-1. Northern hemispheric WDCRG ozone monitor locations. Note that ozone data may not be available for all locations for 2016.

4.2.1.2 Clean Air Status and Trends Network

Due to the sparsity of North American sites in the WDCRG database, we supplemented the dataset with ozone data from the US Clean Air Status and Trends Network (CASTNET)⁹. CASTNET comprises 97 sites that are part of a long-term environmental monitoring program for ambient gases, particulates and atmospheric deposition. Site locations are shown in Figure 4-2. CASTNET measures hourly ozone at 85 sites and is the primary network for measuring rural, regionally representative ozone concentrations. This makes it suitable for H-CAMx MPE since grid resolution is insufficient for local and urban-scale analyses but better suited for regional scale analyses. We reduced the extensive number of CASTNET ozone sites to approximately match the number of European sites, by selecting an unbiased and reasonably uniform spatial distribution of sites across the conterminous US. We followed a 4-step procedure: (1) select remote sites that are not near others; (2) balance the number of sites east and west of the Mississippi River (approximately 12 sites in each region); (3) given the different densities of monitors in each region, randomly select roughly 1 in 3 in the west and roughly 1 in 8 in the east; (4) manually adjust for a small number of sites to improve spatial uniformity. This procedure resulted in 24 uniformly distributed CASTNET sites.

⁸ <http://ebas.nilu.no/ResourcesATMOS/AboutEBAS.pdf>

⁹ <https://www.epa.gov/castnet>

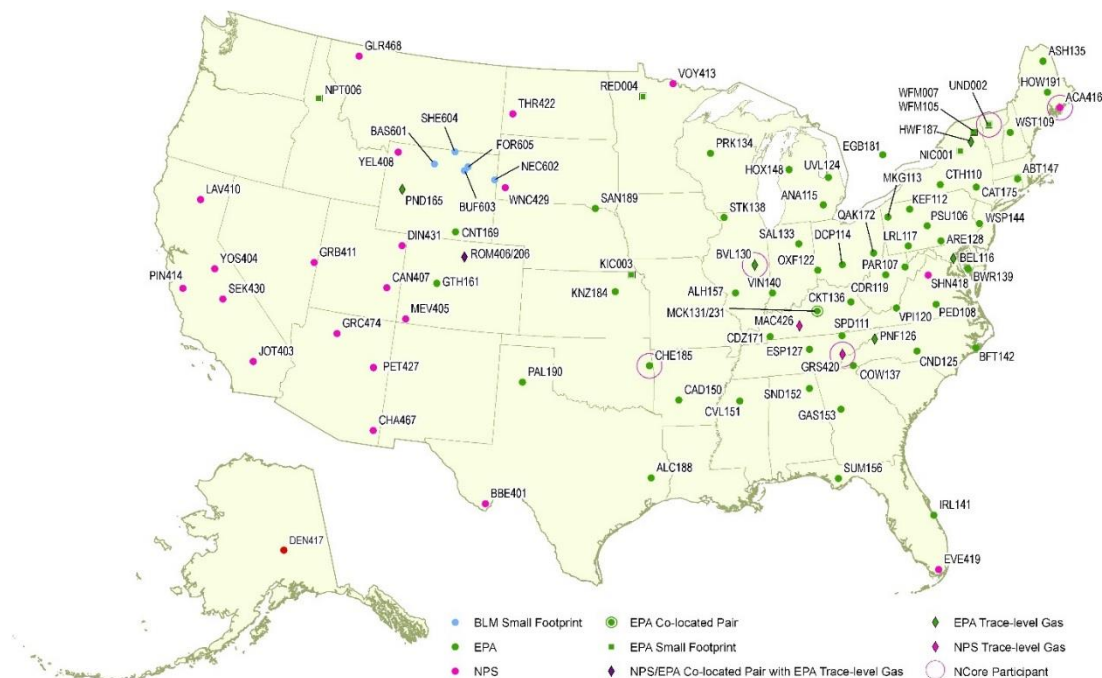


Figure 4-2. US CASTNET sites operating during 2016¹⁰. Ozone is monitored at a majority subset of sites.

4.2.1.3 Combining WDCRG and CASTNET Surface Ozone Data

Figure 4-3 presents a map of the combined WDCRG and CASTNET sites, presented on the H-CAMx polar map projection. To evaluate model performance characteristics over different regions we arranged the sites into five groups:

1. Europe (26 sites)
2. US (24 sites)
3. Asia (4 sites)
4. Northern Latitudes (7 sites)
5. Oceanic (6 sites)

The groups are color-coded on the map in Figure 4-3; sites outside the densely distributed European and US sites are labelled. Figures 4-4 and 4-5 zoom in to focus on the US and Europe, respectively, with labels for each site. Table 4-3 lists all selected surface ozone sites grouped by region and noting county code, latitude/longitude coordinates and specified time zone.

¹⁰ <https://www3.epa.gov/castnet/docs/CASTNET2016/AR2016-main.htm#chapter1-3>

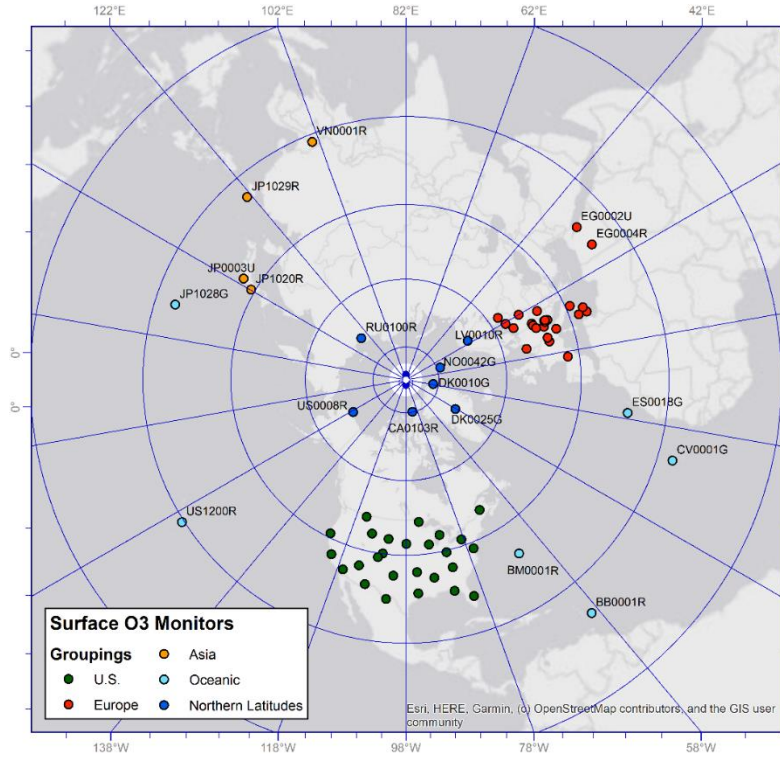


Figure 4-3. All surface monitors with 2016 ozone data selected for H-CAMx MPE, color-coded by evaluation region.

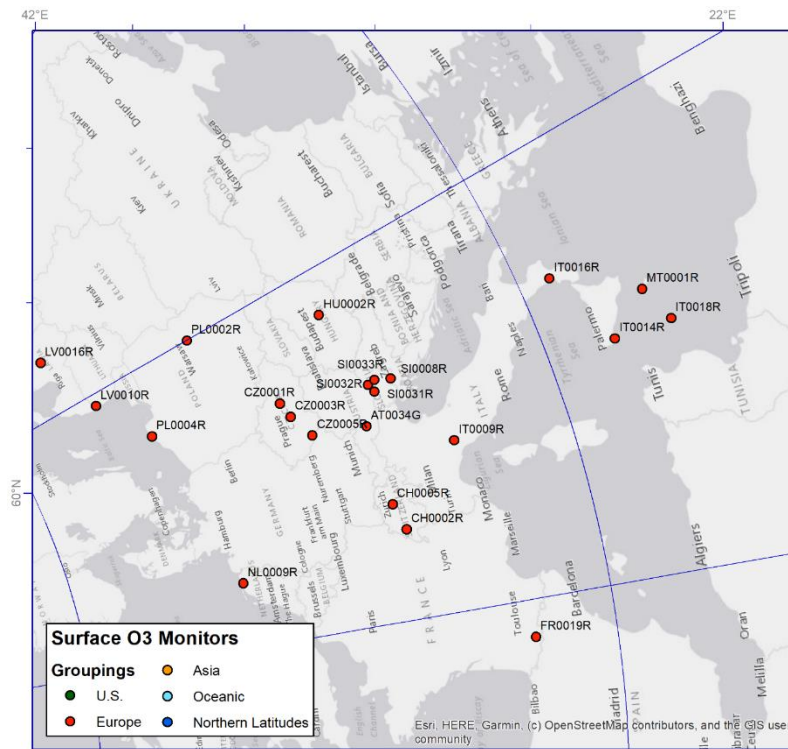


Figure 4-4. European monitors with 2016 ozone data selected for H-CAMx MPE.

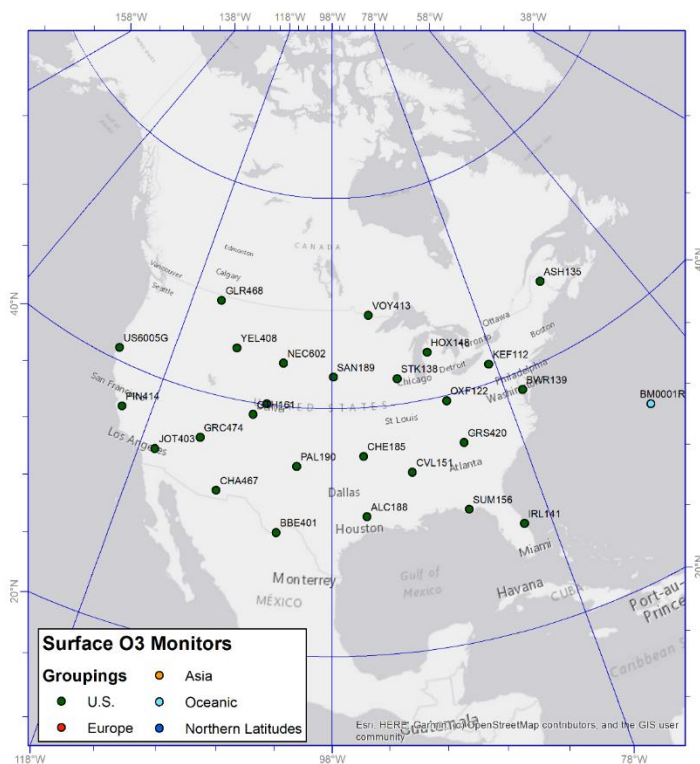


Figure 4-5. US monitors with 2016 ozone data selected for H-CAMx MPE.

Table 4-3. List of all surface ozone monitoring sites selected for H-CAMx MPE.

Region	Site	Country Code	Latitude	Longitude	Time Zone
Oceanic	CV0001G	CV	16.8640	-24.8675	-2
Oceanic	ES0018G	ES	28.3090	-16.4994	-1
Oceanic	US1200R	US	19.5362	-155.5762	-10
Oceanic	JP1028G	JP	24.2883	153.9833	10
Oceanic	BB0001R	BB	13.1700	-59.4300	-4
Oceanic	BM0001R	BM	32.2700	-64.8800	-4
Europe	AT0034G	AT	47.0541	12.9579	1
Europe	CH0002R	CH	46.8131	6.9447	0
Europe	CH0005R	CH	47.0675	8.4639	1
Europe	CZ0001R	CZ	49.7351	16.0342	1
Europe	CZ0003R	CZ	49.5734	15.0803	1
Europe	CZ0005R	CZ	49.0667	13.6000	1
Europe	FR0019R	FR	42.9367	0.1419	0
Europe	HU0002R	HU	46.9667	19.5833	1
Europe	IT0009R	IT	44.1833	10.7000	1
Europe	IT0014R	IT	37.5711	12.6597	1
Europe	IT0016R	IT	38.8763	16.2322	1
Europe	IT0018R	IT	35.5182	12.6305	1
Europe	LV0010R	LV	56.1619	21.1731	1
Europe	LV0016R	LV	57.1353	25.9056	2

Region	Site	Country Code	Latitude	Longitude	Time Zone
Europe	MT0001R	MT	36.0722	14.2184	1
Europe	NL0009R	NL	53.3339	6.2772	0
Europe	PL0002R	PL	51.8144	21.9724	1
Europe	PL0004R	PL	54.7539	17.5343	1
Europe	SI0008R	SI	45.5667	14.8667	1
Europe	SI0031R	SI	46.4286	15.0033	1
Europe	SI0032R	SI	46.2994	14.5386	1
Europe	SI0033R	SI	46.1286	15.1139	1
Europe	EG0002U	EG	27.2900	33.7499	2
Europe	EG0004R	EG	27.0582	27.9903	2
Polar	DK0010G	DK	81.6000	-16.6700	-1
Polar	DK0025G	DK	72.5800	-38.4800	-3
Polar	FI0096G	FI	67.9733	24.1161	2
Polar	NO0042G	NO	78.9072	11.8867	1
Polar	CA0103R	CA	80.0500	-86.4167	-6
Polar	RU0100R	RU	71.5862	128.9188	9
Polar	US0008R	US	71.3230	-156.6115	-10
Asia	JP0003U	JP	36.0581	140.1258	9
Asia	JP1020R	JP	39.0319	141.8222	9
Asia	JP1029R	JP	24.4669	123.0109	8
Asia	VN0001R	VN	21.5731	103.5157	7
US	US0204R	US	40.0500	-105.5900	-7
US	US6005G	US	41.0541	-124.1510	-8
US	ALC188	US	30.7016	-94.6740	-6
US	ASH135	US	46.6038	-68.4132	-5
US	BBE401	US	29.3027	-103.1778	-6
US	CHA467	US	32.0094	-109.3891	-7
US	GLR468	US	48.5103	-113.9968	-7
US	IRL141	US	27.8492	-80.4556	-5
US	PAL190	US	34.8806	-101.6647	-6
US	PIN414	US	36.4832	-121.1569	-8
US	SAN189	US	42.8292	-97.8541	-6
US	SUM156	US	30.1102	-84.9904	-5
US	VOY413	US	48.4125	-92.8292	-6
US	CHE185	US	35.7508	-94.6698	-6
US	GRC474	US	36.0586	-112.1836	-7
US	GTH161	US	38.9563	-106.9859	-7
US	JOT403	US	34.0696	-116.3889	-8
US	NEC602	US	43.8730	-104.1919	-7
US	BWR139	US	38.4450	-76.1113	-5
US	CVL151	US	34.0028	-89.7992	-6
US	GRS420	US	35.6335	-83.9416	-5
US	HOX148	US	44.1809	-85.7390	-5
US	KEF112	US	41.5981	-78.7679	-5
US	STK138	US	42.2872	-90.0000	-6
US	OXF122	US	39.5311	-84.7236	-5
US	YEL408	US	44.5654	-110.4003	-7

4.2.2 Ozonesonde Measurements

Global ozonesonde measurements were obtained from the World Ozone and Ultraviolet Radiation Data Centre (WOUDC)¹¹, also part of the WMO GAW program. The WOUDC is operated by the Meteorological Service of Canada, a branch of Environment and Climate Change Canada. The National Oceanic and Atmospheric Administration's (NOAA) ozonesondes measurements¹² can also be retrieved from this data center. The temporal resolution for the ozonesondes profiles is generally every few days. This dataset is discussed in more detail in Ramboll's TCEQ project report summarizing data sources for evaluating GEOS-Chem model performance (Ramboll, 2019b). Figure 4-6 presents the global distribution of ozonesonde sites with data available in 2016. Figure 4-7 shows the location of northern hemispheric ozonesonde sites selected for H-CAMx evaluation, presented on the H-CAMx polar map projection. The process for selecting these sites was in large part determined by EPA's evaluation of H-CMAQ, as described in the next section. Table 4-4 lists the selected ozonesonde sites, their site ID, region, number of available sondes in 2016 and their latitude/longitude coordinates.

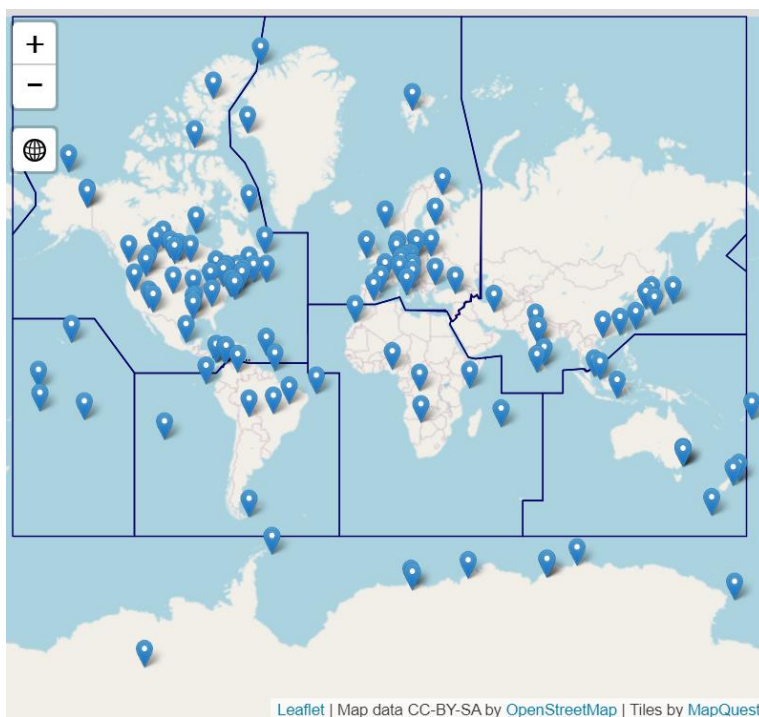


Figure 4-6. Global ozonesonde launch sites available in the WOUDC dataset with data available in 2016¹³.

¹¹ <https://woudc.org/home.php>

¹² <https://www.esrl.noaa.gov/gmd/ozwv/ozsondes/>

¹³ <https://woudc.org/data/explore.php>

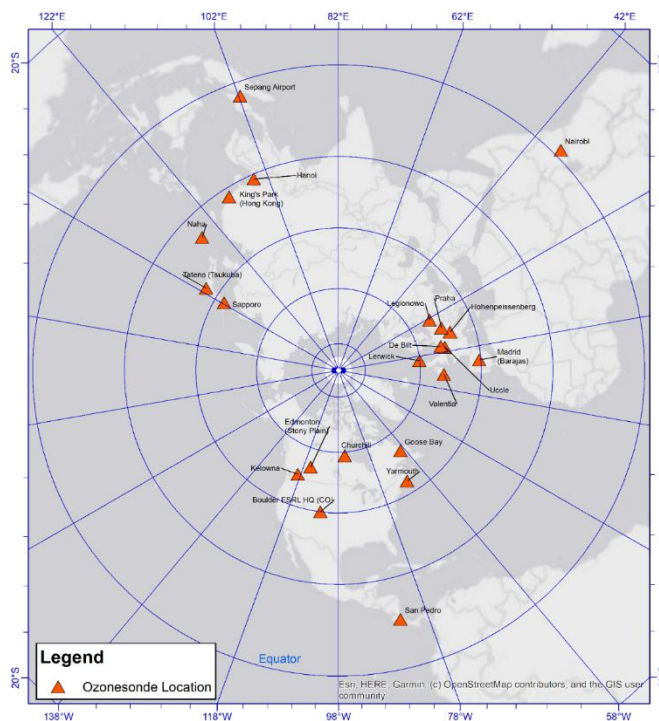


Figure 4-7. Northern hemispheric ozonesonde locations selected for H-CAMx MPE.

Table 4-4. List of ozonesonde sites selected for H-CAMx MPE.

Site Name	Site ID	Region	# Sondes in 2016	Latitude	Longitude
Sapporo	stn012	Asia	51	43.060	141.333
Tateno (Tsukuba)	stn014	Asia	48	36.050	140.133
Nairobi	stn175	Africa	48	-1.300	36.750
NAHA	stn190	Asia	48	26.200	127.683
Hanoi	stn330	Asia	21	21.200	105.800
King's Park (Hong Kong)	stn344	Asia	48	22.312	114.173
Sepang Airport	stn443	Asia	24	2.730	101.700
Lerwick	stn043	Europe	53	60.133	-1.183
UCCLE	stn053	Europe	138	50.798	4.359
Hohenpeissenberg	stn099	Europe	129	47.801	11.010
Legionowo	stn221	Europe	32	52.400	20.970
Praha	stn242	Europe	51	50.008	14.447
Madrid (Barajas)	stn308	Europe	51	40.450	-3.720
De Bilt	stn316	Europe	56	52.100	5.183
Valentia	stn318	Europe	29	51.938	-10.248
Kelowna	stn457	North America	37	49.970	-119.380
Yarmouth	stn458	North America	32	43.870	-66.100
Goose Bay	stn076	North America	48	53.290	-60.388
Edmonton (Stony Plain)	stn021	North America	42	53.550	-114.100
Boulder	stn067	North America	49	39.991	-105.261
Churchill	stn077	North America	18	58.738	-93.821
San Pedro	stn524	North America	47	10.000	-84.000

4.3 Postprocessing Methodology

4.3.1 Surface Ozone Data

The surface ozone MPE employed a tool called “evalwdcrg”, which Ramboll developed for a previous GEOS-CHEM MPE study for TCEQ in FY19 (Ramboll, 2019b). The tool comprises a set of python scripts that pairs GEOS-Chem model output and WDCRG observation data in time, saves the paired output to comma-delimited text files and then generates performance plots such as timeseries, scatter and Q-Q plots by site. We modified the tool to accommodate the model output formats of H-CAMx and H-CMAQ, to process CASTNET measurement data, and to calculate and generate plots for maximum daily 8-hr average ozone (MDA8). For reasons of consistency in our inter-model comparison, we calculated 24 running 8-hr ozone averages per day for the MDA8 calculation, as opposed to the newer EPA-recommended approach of 16 8-hour averages per day (avoiding multi-day MDA8 overlap), since that was the method employed by EPA to generate their 2016 H-CMAQ surface MDA8 dataset that they provided for this analysis. All site-specific timeseries, scatter and Q-Q plots from all models and H-CAMx cases have been provided to TCEQ at the close of the project.

Additional scripts were developed to calculate 2016 period-wide observed and model dataset statistics, including concentration means, 10th and 90th percentiles, normalized mean bias (NMB), normalized gross or unsigned error (NME), and correlation coefficient (R) for each surface site and for each of the three models for the inter-model performance comparison. Statistical definitions for NMB, NME and R are provided in Appendix A. All surface data processing and statistical calculation activities were reviewed for quality assurance. This included independently checking program configurations and scripts, reviewing message files, and spot-checking resulting variable fields graphically for obvious problems or flaws. Some issues with inconsistent data formats and units were found among several sites within the WDCRG dataset, which required special re-processing to ensure proper values were incorporated into the analyses described below.

4.3.2 Ozonesonde Data

EPA developed the “evalwoudc” tool to compare photochemical grid model output against vertical ozonesonde measurements from the WOUDC global database. The tool is compatible with model data output in Models3 IO-API/netCDF format (i.e., generated by CMAQ). The evalwoudc tool queries the WOUDC ozonesonde database to extract the measured data at runtime. Note the database appears to update periodically so available ozonesonde measurements can differ over time. EPA provided a dataset of modeled vertical ozone profiles extracted from their 2016 H-CMAQ run that correspond to ozonesonde sites with valid data in 2016 (Dr. Barron Henderson, personal communication). This constrained our choice of ozonesonde sites to use for the inter-model comparison. The resulting ozonesonde sites listed in Table 4-4 provide reasonable global coverage as shown in Figure 4-7. Furthermore, we selected ozonesonde sites according to the number days with valid data; i.e., we excluded sites with less than 15 ozonesonde measurements per year. We processed H-CAMx model output into the required netCDF format and then applied the evalwoudc tool to generate simulated ozone profiles at the global ozonesonde sites. We similarly processed our 2016 GEOS-Chem dataset for the inter-model comparison. All ozonesonde data processing activities were reviewed for quality assurance. This included independently checking program configurations and scripts, reviewing message files, and spot-checking resulting variable fields graphically for obvious problems or flaws.

4.4 Inter-Model Performance Comparison

We first compare annual H-CAMx Run0 ozone results to the 2016 GEOS-Chem output used previously to develop H-CAMx IC/BC inputs and to EPA’s 2016 H-CMAQ results. Qualitative comparisons are made graphically against measured ozonesonde profiles at the WOUDC sites described above.

Graphical and statistical comparisons are made against surface ozone measurements at the selected WDCRG and CASTNET sites.

4.4.1 Ozonesonde Comparisons

Figure 4-8 presents modeled ozone profiles against measurements at each ozonesonde site. The figures show the average profile over all days in 2016 for which data are available, and the annual minimum to maximum ozone range as a function of altitude. Ozonesonde measurements were interpolated to the vertical height coordinates of each model for plotting. Note that both pressure altitude and concentration axes are plotted logarithmically to better show details in the range of data.

Consistently, GEOS-Chem qualitatively best replicates stratospheric ozone at most sites around the world, though it tends toward a negative bias in the troposphere. H-CMAQ is often similar to GEOS-Chem but consistently exhibits more negative bias throughout the profile. Also, at many low-latitude sites H-CMAQ indicates occasional ozone gaps near zero around the tropopause, as seen in the minimum ozone range. The cause for this is not known, though we speculate that it could be related to the CMAQ potential vorticity stratospheric ozone scheme for low-latitude, high-altitude tropopauses. H-CAMx differs from the other models in that it consistently generates a negative bias in the stratosphere and a positive bias in the troposphere. All models generally exhibit narrower minimum-to-maximum ranges than the observations, except occasionally for H-CMAQ as noted above.

Stratospheric ozone in H-CAMx exhibits some puzzling features. For sites at middle and northern latitudes the annual-average stratospheric profile is nearly identical among sites, indicating a tropopause just above 250 hPa (10-11 km). While this is climatologically consistent with expectations, most of these higher latitude sites indicate tropopause heights at 300-400 mb (7-9 km) based on clear gradient discontinuities in the observed annual average ozone profiles. Note that for ozonesonde sites at lower latitudes, H-CAMx properly diagnoses higher tropopause altitudes at or above 100 mb (~16 km) and modeled and measured ozone profiles match rather well, often as good or better than the other models. It would appear that the stratospheric ozone treatment in H-CAMx is not allowing a tropopause diagnosis lower than about 10 km. If the stratospheric treatment were allowed to extend lower at these latitudes, H-CAMx performance in replicating stratospheric ozone profiles should improve. Since the diagnosis of tropopause height is based on a standard definition of temperature lapse rate according to the World Meteorological Organization (WMO, 1992), this apparent limitation may be related to inadequate vertical resolution or a bug or other limitation in the H-CAMx tropopause diagnostic algorithm. Sensitivity to vertical resolution is addressed in H-CAMx Run2. We reviewed the tropopause diagnostic algorithm and identified a few minor issues that we modified and verified are helpful based on short tests. These modifications were carried into the remaining H-CAMx runs described in Section 4.5.

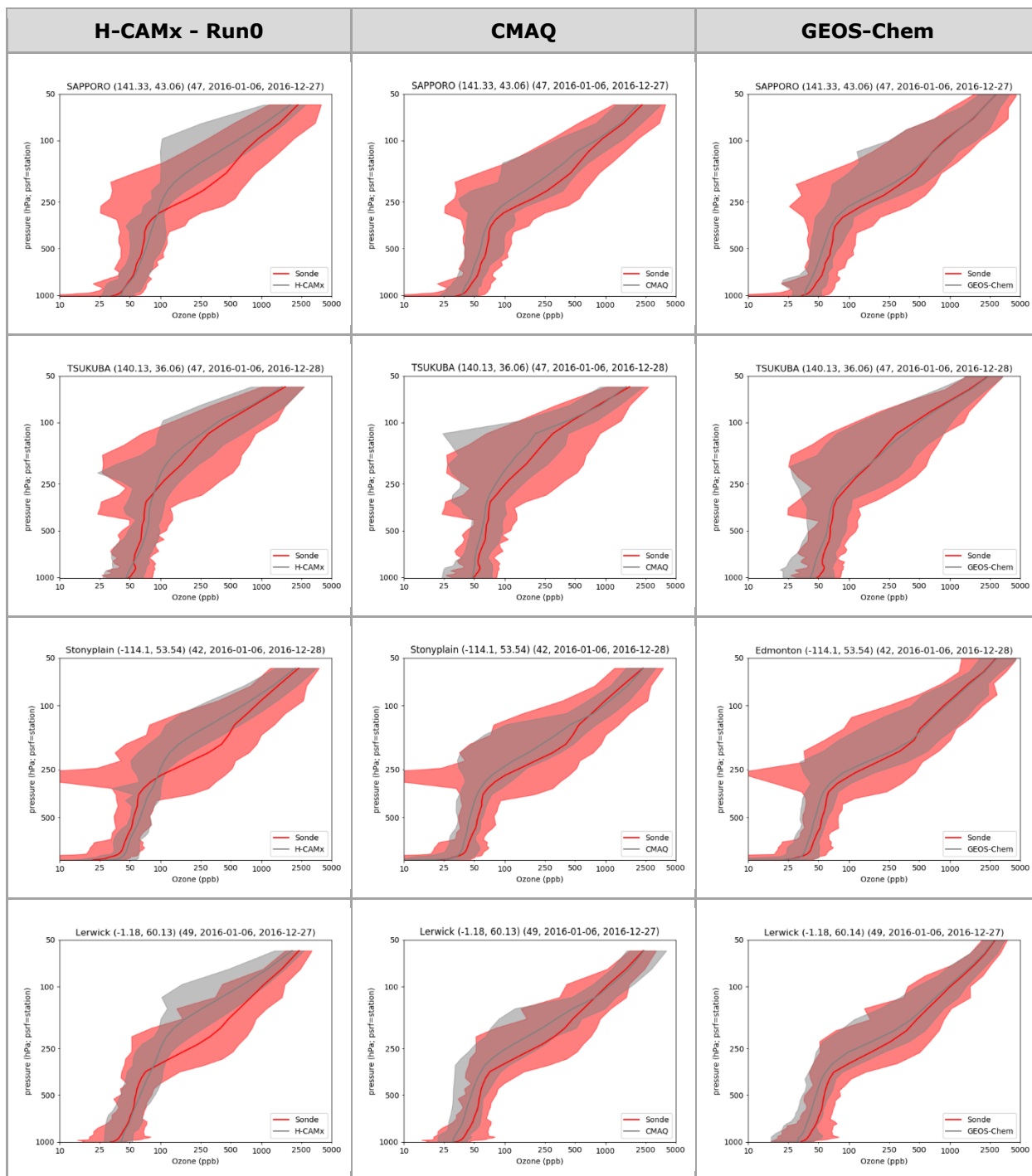


Figure 4-8. Modeled (grey) and observed (red) ozone profiles at global ozonesonde sites. The average over all 2016 profiles are shown as the solid lines, annual minimum to maximum ozone ranges are shaded. The number of profiles in 2016 and station latitude/longitude are noted above each plot.

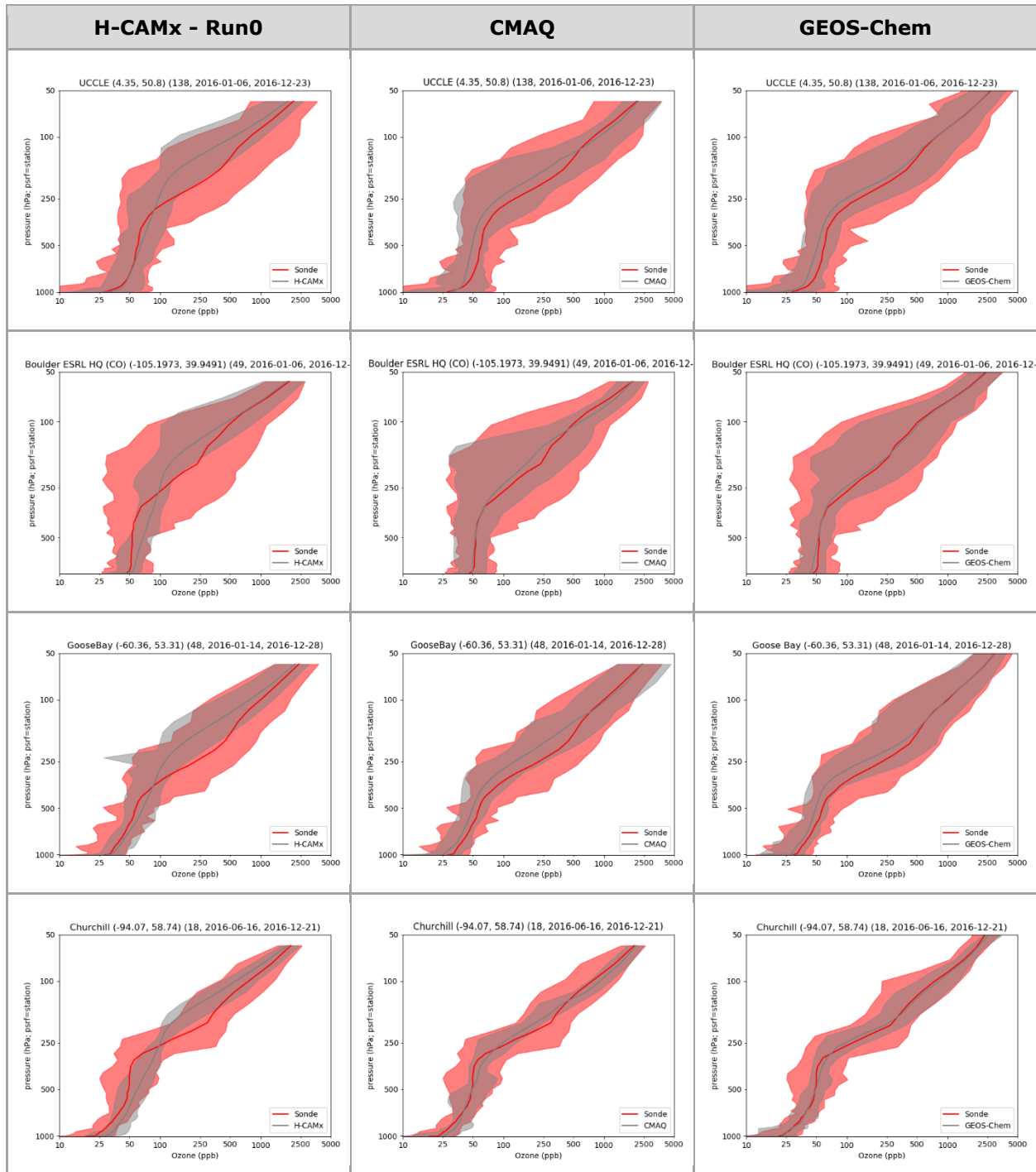


Figure 4-8 (continued).

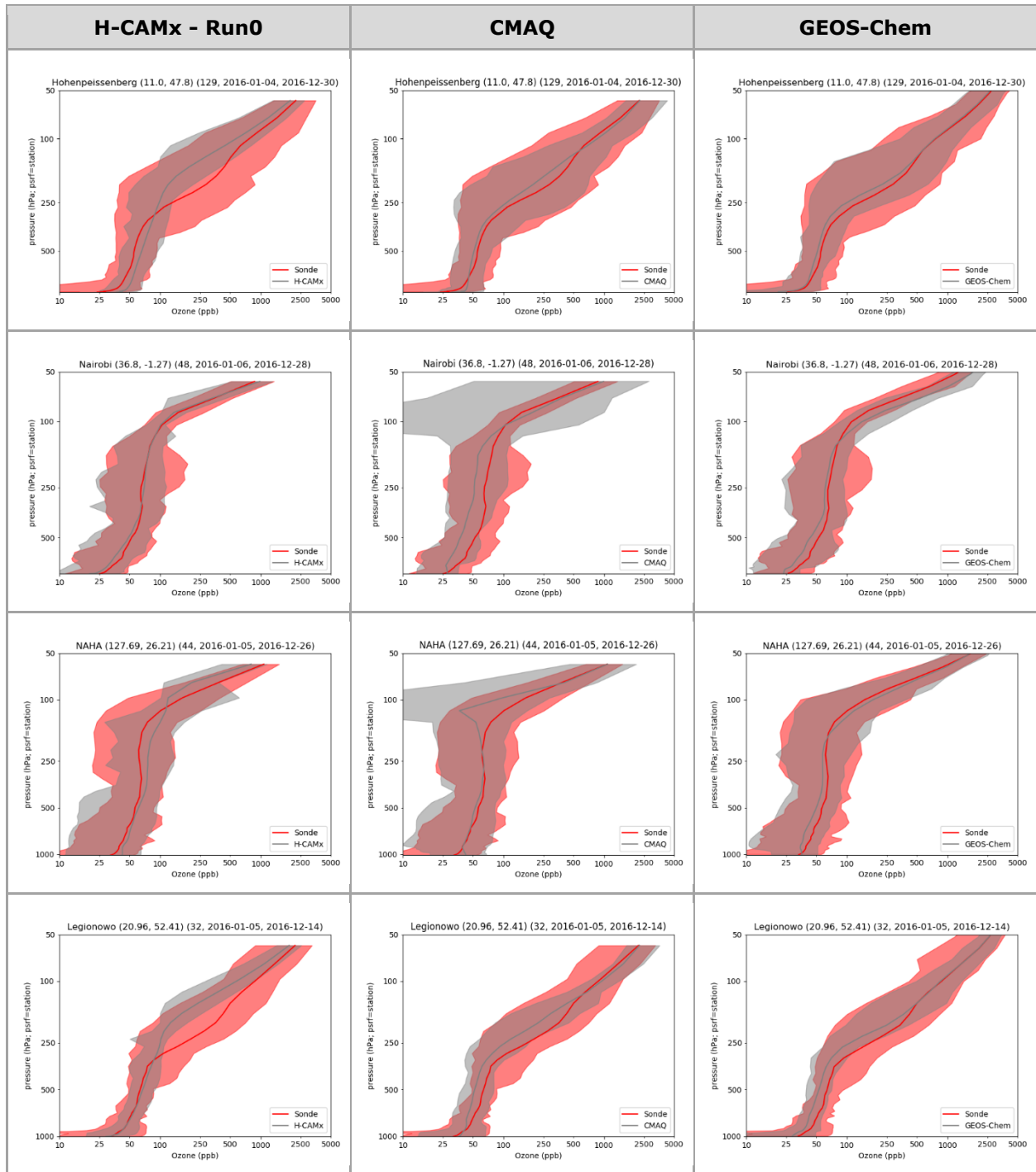


Figure 4-8 (continued).

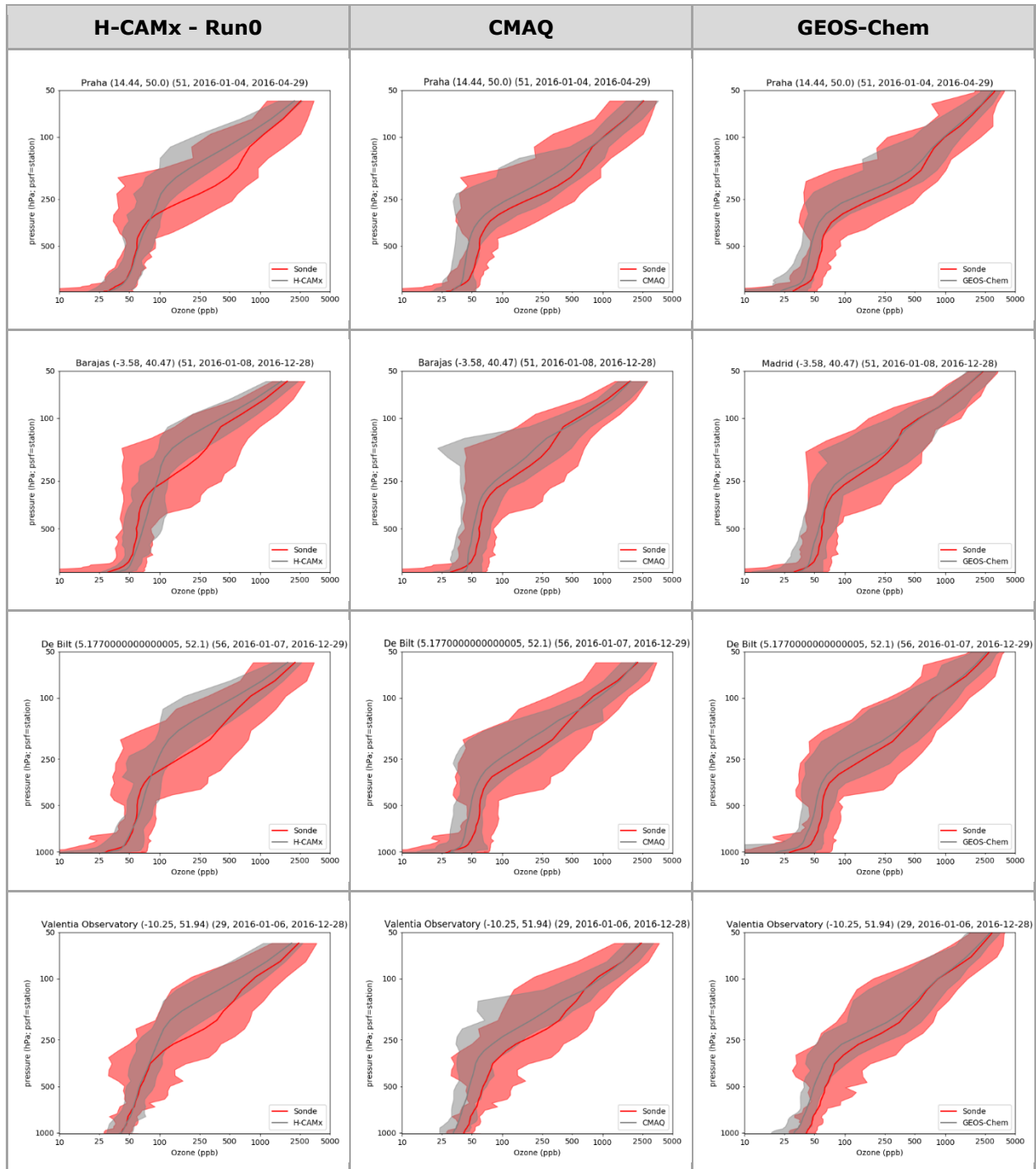


Figure 4-8 (continued).

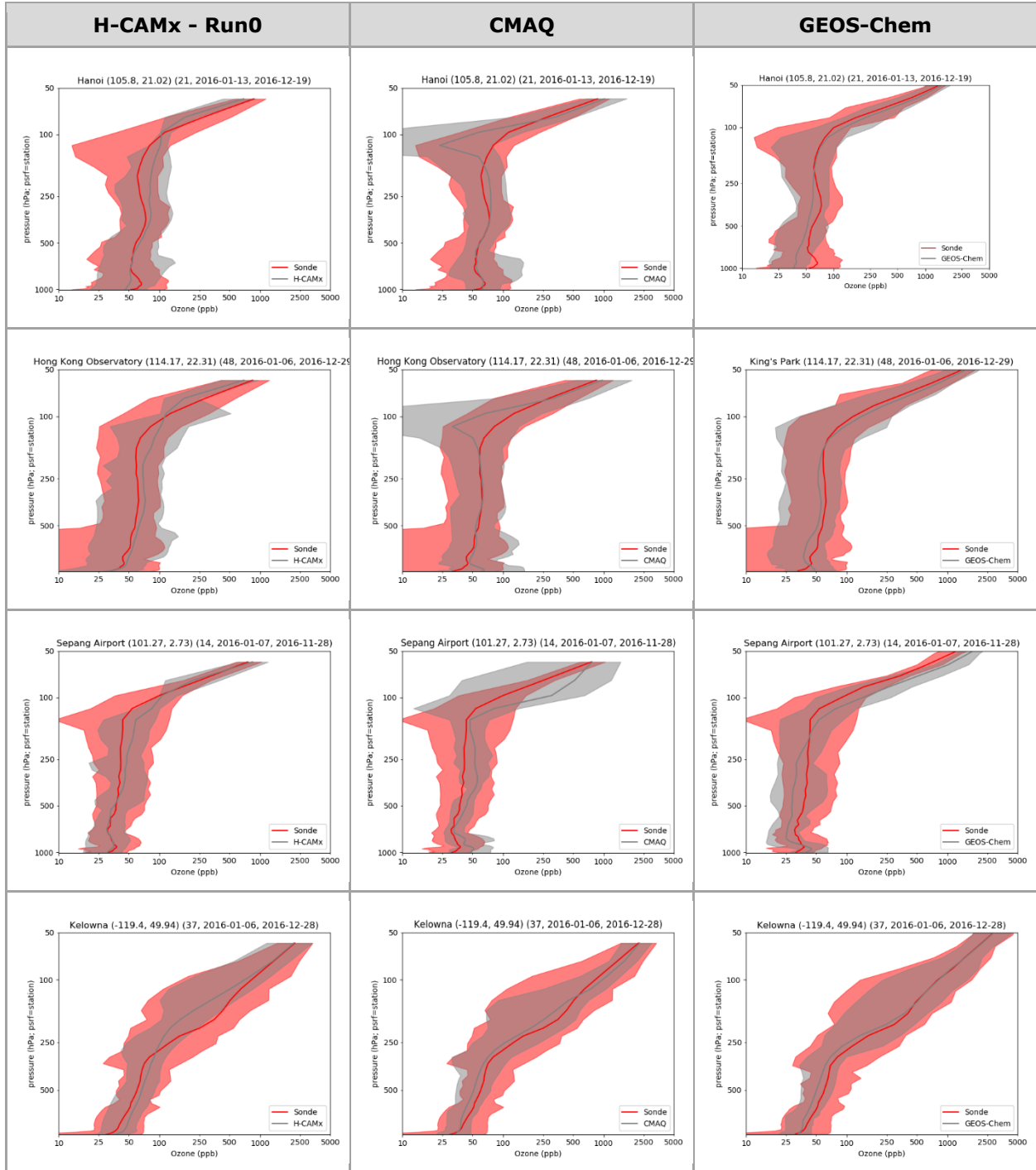


Figure 4-8 (continued).

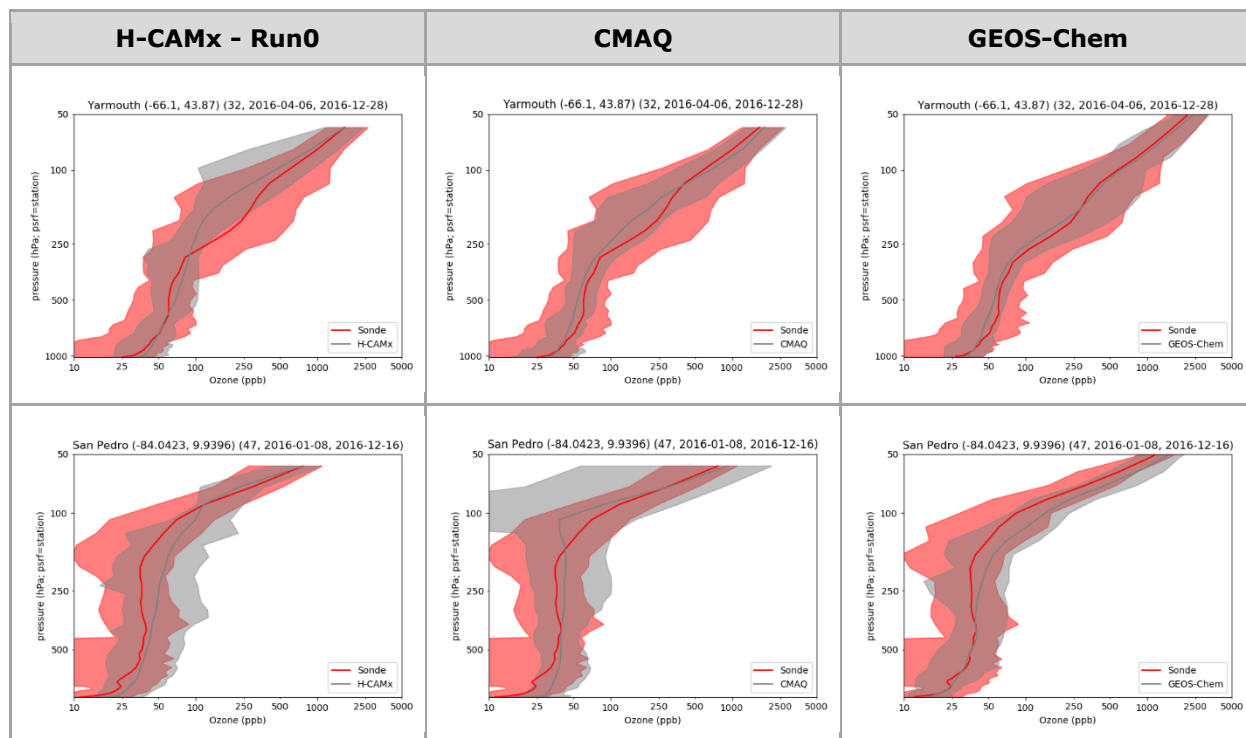


Figure 4-8 (concluded).

4.4.2 Surface Ozone Comparisons

Figures 4-9 through 4-13 compare measured and modeled surface ozone ranges and statistical performance metrics by site for each of the five site groups. Model results and statistics for H-CAMx Run0, H-CMAQ and GEOS-Chem are shown together to ease comparison.

Among the US sites (Figure 4-9) the models generally exhibit little bias (NMB) site-by-site and a range of gross error (NME) of 10-20%, which is rather good and consistent with regional modeling applications over the US. GEOS-Chem and H-CMAQ exhibit the lowest bias (positive or negative), whereas H-CAMx has a consistent positive bias and shows some rather large deviations from the other models at Glacier (GLR468, Montana), Pinnacles (PIN414, California) and Trinidad Head (US6005G). Causes for these deviations at just a few sites are not clear, but inspection of time series indicates that H-CAMx consistently overestimates ozone at these sites during much of the year, so this performance trait is not driven by a small set of specific seasonal events such as fires. While H-CAMx over predicts ozone all year long at Trinidad Head, it is especially high during the summer when observed ozone is suppressed but both H-CAMx and H-CMAQ maintain ozone near the annual mean (although H-CMAQ summer over predictions are not as large). However, GEOS-Chem can replicate the summer ozone suppression at Trinidad Head. We presume this observed feature is related to the influence of the summertime stable/shallow marine environment in the eastern Pacific, when elevated natural halogen emissions together with shipping NO_x emissions reduce surface-layer ozone in the absence of VOC. We initially thought the different model responses were caused by the alignment of the H-CAMx/CMAQ 108-km grid cell containing Trinidad Head, which might span over a larger proportion of land area than the corresponding GEOS-Chem grid cell, thereby reflecting more terrestrial influences such as biogenic and fire emissions. However, we found that this was not the

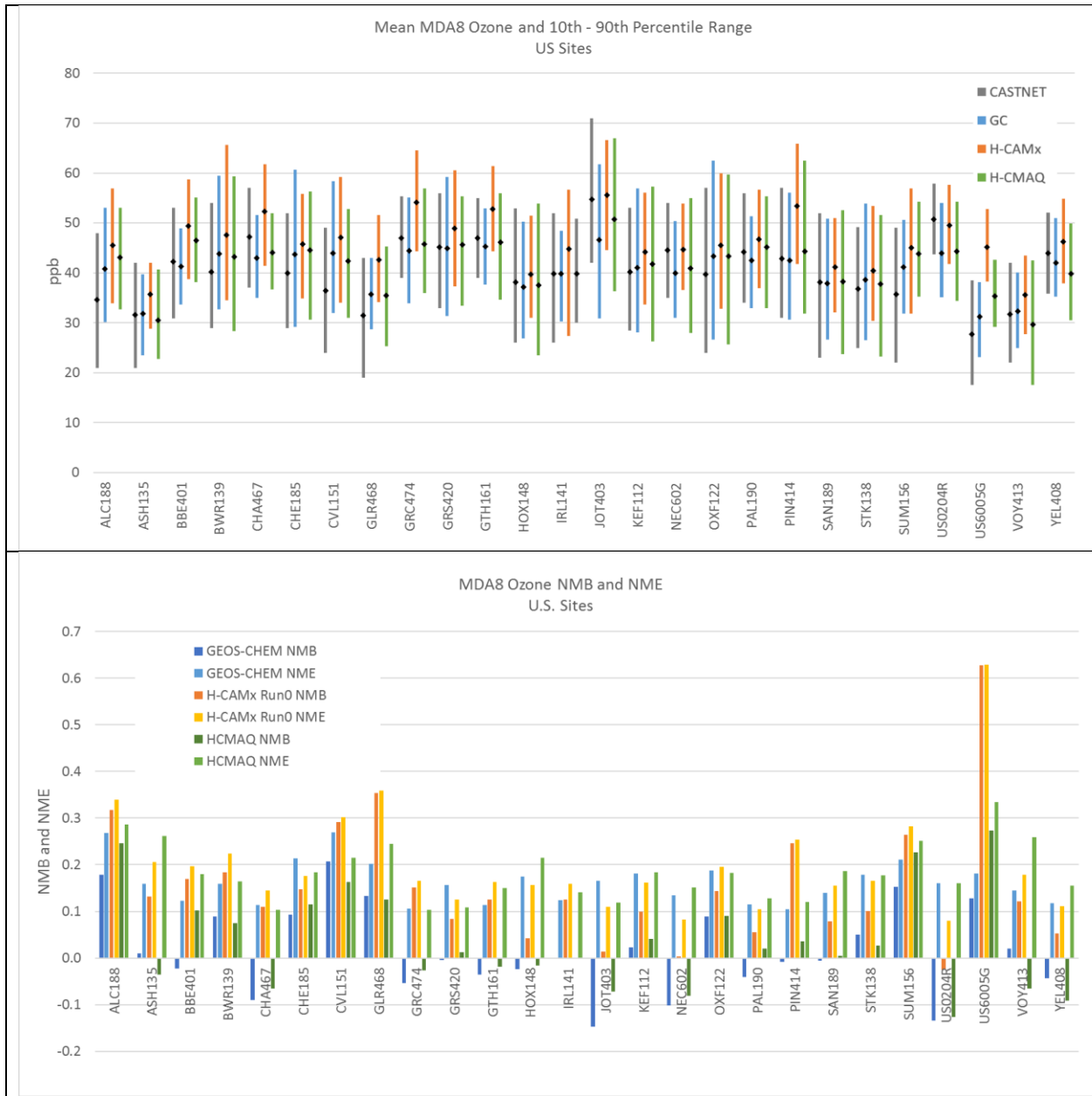


Figure 4-9. Measured and modeled annual average (black dots) and 10th-90th percentile ranges (vertical bars) of surface ozone by US site (top panel), and modeled statistical performance metrics for bias (NMB as decimal fraction) and gross error (NME as decimal fraction) by US site (bottom panel). Observations are shown in grey, GEOS-Chem results are shown in blue, H-CAMx Run0 results are shown in orange, and H-CMAQ results are shown in green.

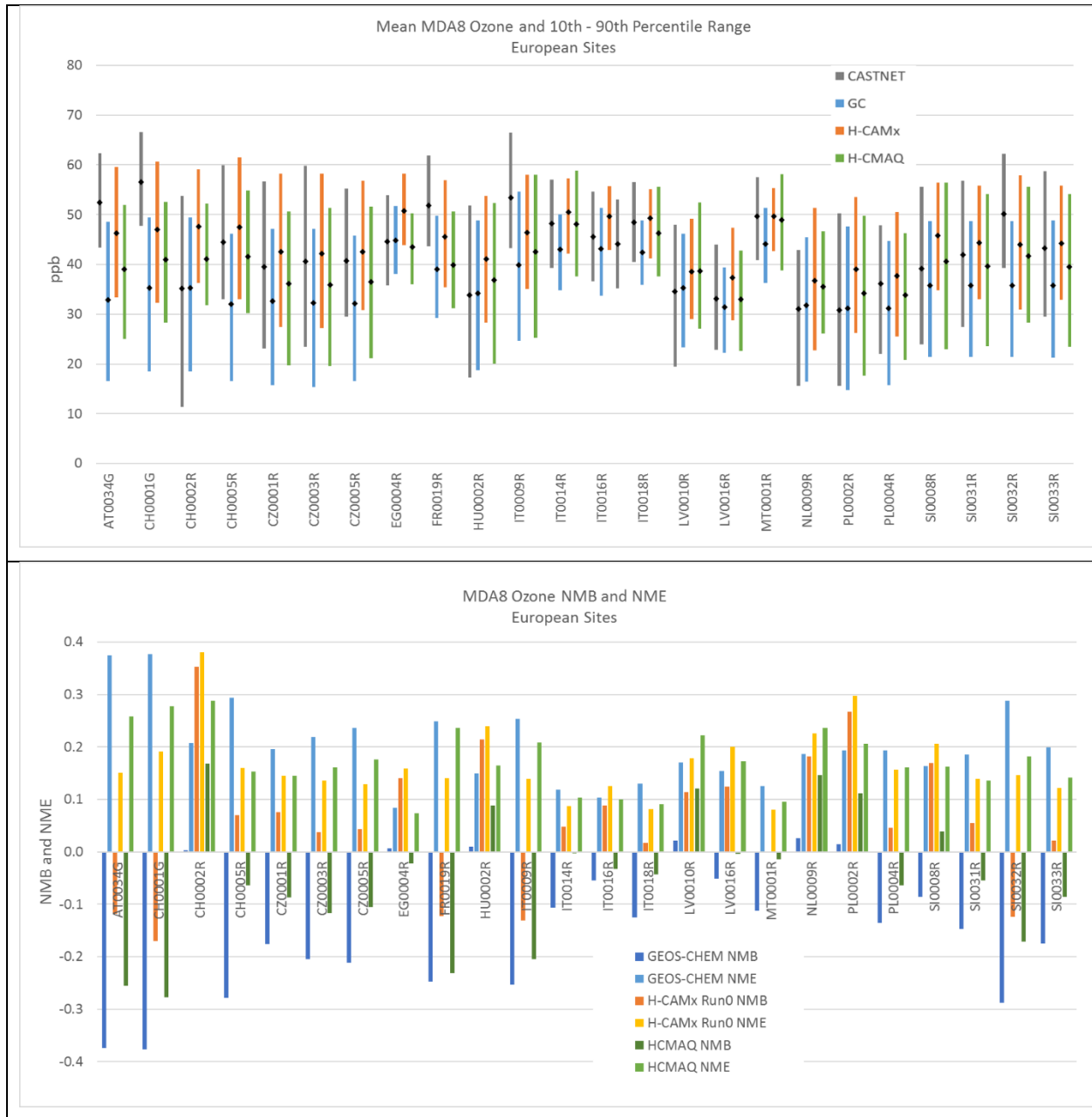


Figure 4-10. Measured and modeled annual average (black dots) and 10th-90th percentile ranges (vertical bars) of surface ozone by European site (top panel), and modeled statistical performance metrics for bias (NMB as decimal fraction) and gross error (NME as decimal fraction) by European site (bottom panel). Observations are shown in grey, GEOS-Chem results are shown in blue, H-CAMx Run0 results are shown in orange, and H-CMAQ results are shown in green.

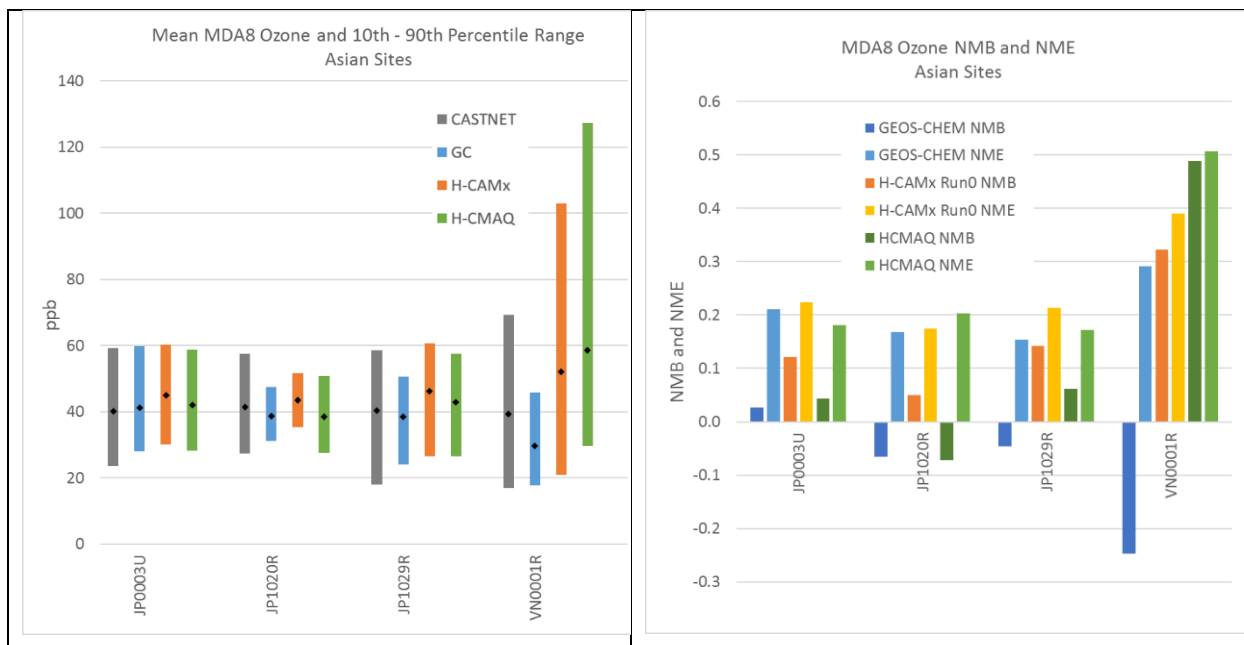


Figure 4-11. Measured and modeled annual average (black dots) and 10th-90th percentile ranges (vertical bars) of surface ozone by Asian site (left panel), and modeled statistical performance metrics for bias (NMB as decimal fraction) and gross error (NME as decimal fraction) by Asian site (right panel). Observations are shown in grey, GEOS-Chem results are shown in blue, H-CAMx Run0 results are shown in orange, and H-CMAQ results are shown in green.

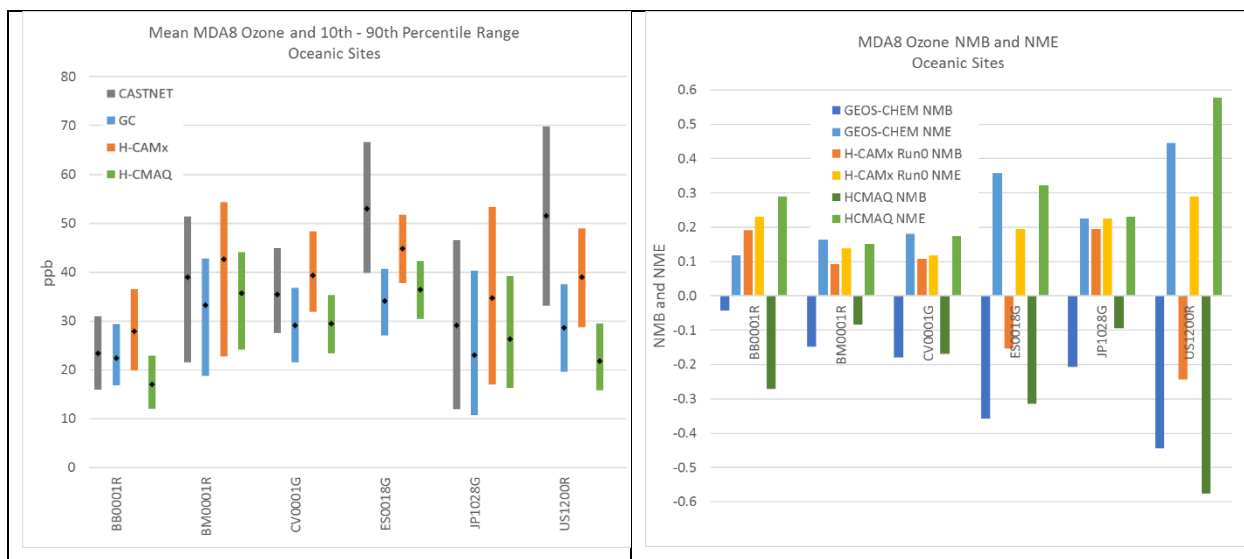


Figure 4-12. Measured and modeled annual average (black dots) and 10th-90th percentile ranges (vertical bars) of surface ozone by Oceanic site (left panel), and modeled statistical performance metrics for bias (NMB as decimal fraction) and gross error (NME as decimal fraction) by Oceanic site (right panel). Observations are shown in grey, GEOS-Chem results are shown in blue, H-CAMx Run0 results are shown in orange, and H-CMAQ results are shown in green.

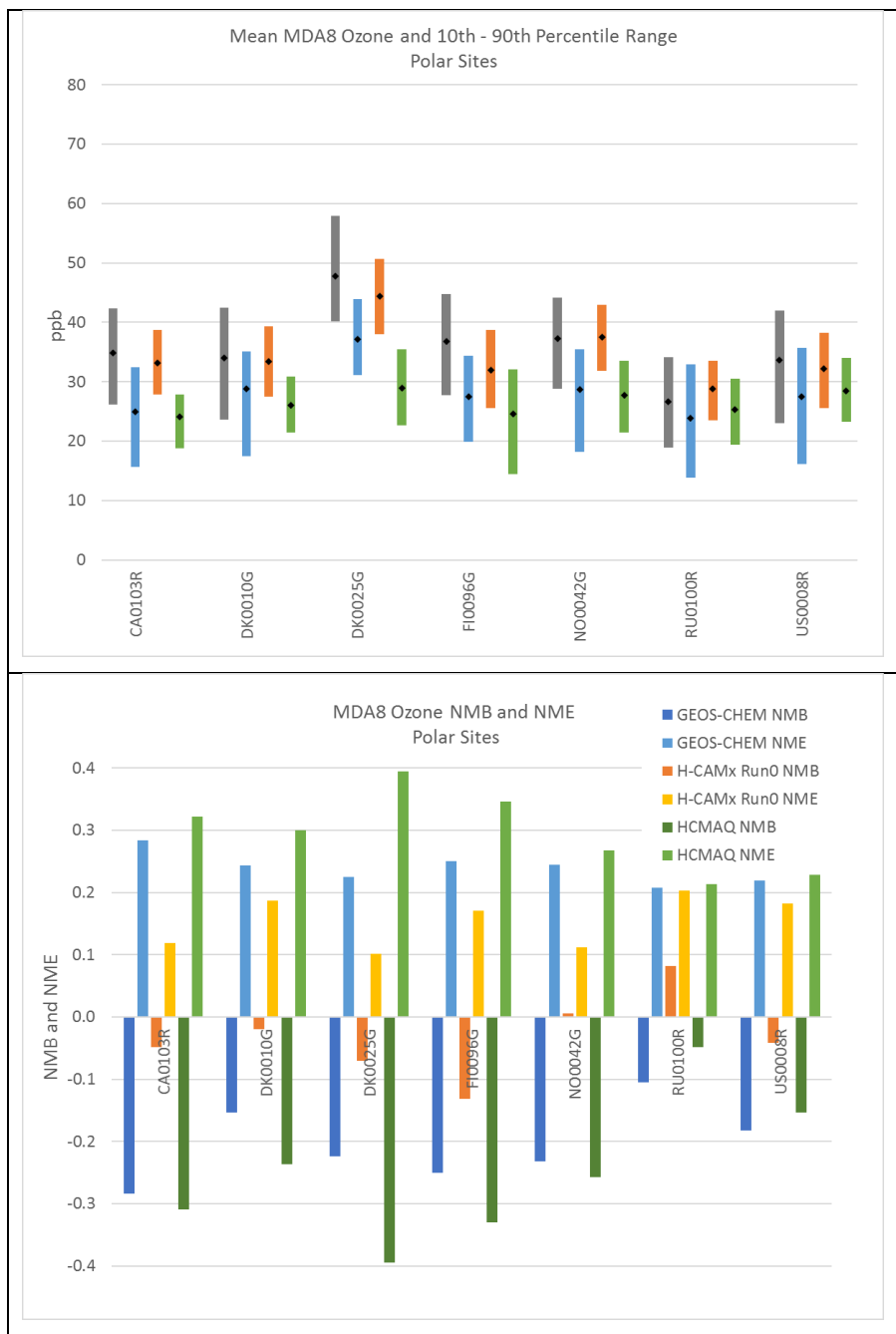


Figure 4-13. Measured and modeled annual average (black dots) and 10th-90th percentile ranges (vertical bars) of surface ozone by Polar site (left panel), and modeled statistical performance metrics for bias (NMB as decimal fraction) and gross error (NME as decimal fraction) by Polar site (right panel). Observations are shown in grey, GEOS-Chem results are shown in blue, H-CAMx Run0 results are shown in orange, and H-CMAQ results are shown in green.

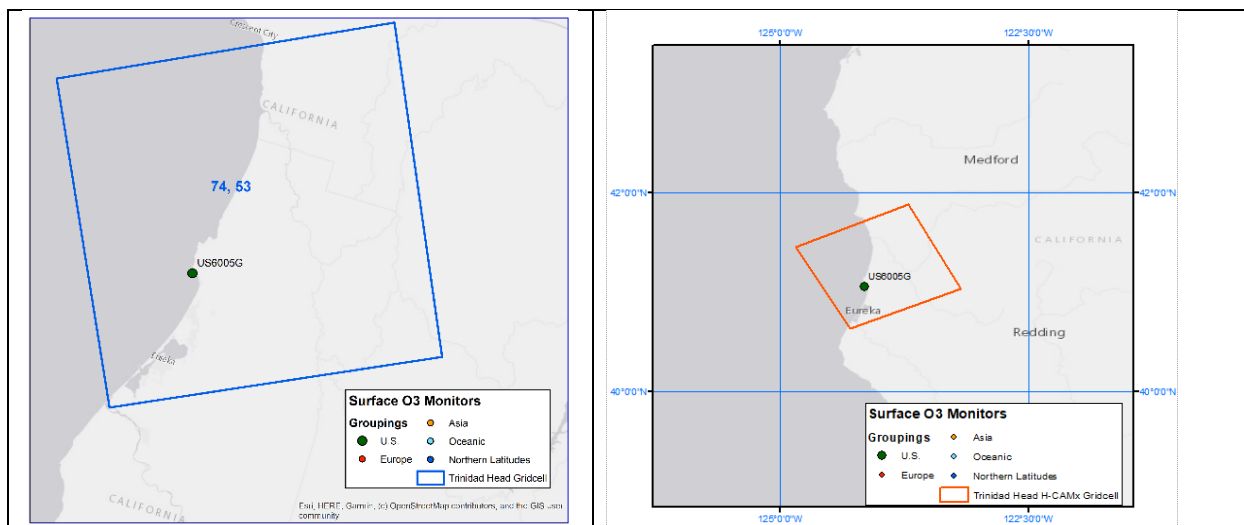


Figure 4-14. Alignment of the H-CAMx 108-km grid cell (left, blue and right, red) and GEOS-Chem grid cell (right, blue) containing the Trinidad Head monitoring site (green dot).

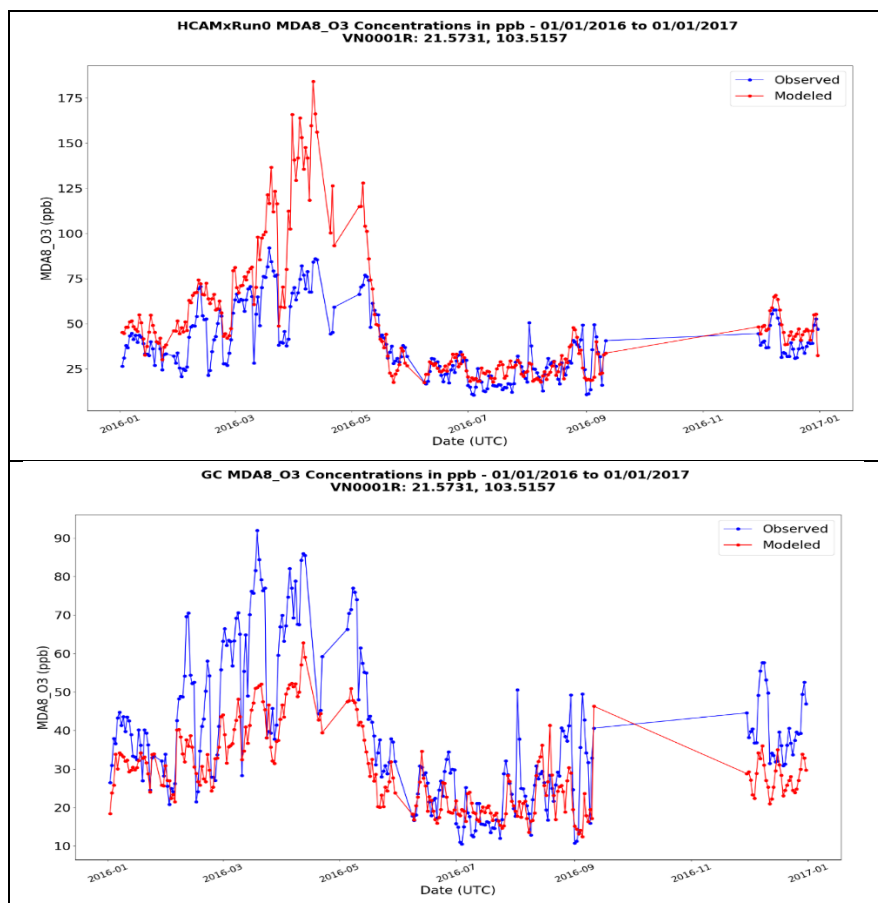


Figure 4-15. Time series over 2016 of monitored (blue) and simulated (red) MDA8 ozone at the WDCRG Hanoi, Vietnam site. Results for H-CAMx are in the top panel, GEOS-Chem in the bottom panel (not differences in vertical ozone scale in each). H-CMAQ results are similar to H-CAMx but present higher peak ozone.

case (Figure 4-14), as GEOS-Chem's grid cell extends much farther over northwestern California. Different natural emissions (biogenic, fires) and different wind fields (consistent onshore vs. variable directions) might also offer explanations. For now the cause for this performance issue remains unclear.

Performance trends among European sites are similar to those in the US (Figure 4-10). While GEOS-Chem exhibits a clear negative bias, H-CMAQ and H-CAMx performance is rather good with consistently near neutral bias and low gross error. H-CAMx again exhibits the most consistently positive bias while H-CMAQ exhibits a slight negative bias.

At the Asian sites (Figure 4-11), all models perform rather well for three of the four sites with low bias and gross error and high correlation (not shown). GEOS-Chem has the smallest bias (mostly negative) and H-CAMx the largest bias (entirely positive). All three models exhibit largest gross error at Hanoi, Vietnam (VN0001R), with H-CMAQ being particularly poor at that site. Based on time series at Hanoi (Figure 4-15) observed >90th percentile values (70-90+ ppb) all occur between February and April, indicating a tendency for episodic springtime ozone events. H-CAMx and H-CMAQ also produce their highest ozone values during this period but over predict dramatically, while they perform rather well over the remainder of the year. On the other hand, GEOS-Chem exhibits its largest under predictions at Hanoi during the spring, indicating an opposite problem. We initially thought that high simulated and observed ozone was associated with downward mixing of stratospheric ozone over the Himalayas, given that Hanoi is the closest site downwind. Analysis of daily spatial plots of ozone (not shown) do indicate some higher ozone in Southeast Asia extending back to the Himalayas during this time. However, a substantial local ozone peak is simulated over Hanoi that can only be caused by local emissions, as confirmed by analysis of NO_x emissions patterns (not shown) that are orders of magnitude higher than any other areas in east Asia, including the largest cities in China. We therefore believe that emission estimates for Hanoi are in error.

The characteristic model-to-model differences described above extend to the oceanic sites (Figure 4-12). Both GEOS-Chem and H-CMAQ exhibit consistent under predictions, while H-CAMx shows mostly over predictions. Bias and gross error statistics remain in the 20-30% range for all models except at Mauna Loa, Hawaii (US1200R) where GEOS-Chem and H-CMAQ exceed 40% due to extreme under predictions. We attribute this feature to the inability for the coarse resolution to resolve the altitude of the Mauna Loa site (3400 m), where the models characterize ozone near sea level and the monitor senses mid-tropospheric air with concentrations ranging 35-70 ppb with a mean of 52 ppb. The other oceanic site where all three models largely underestimate ozone is on a volcano in the Canary Islands (ES0018G, 2400 m), where a similar topographic bias is at play. Finally, we again see the same model-to-model differences in the polar region (Figure 4-13). Like we see for oceanic sites, polar ozone is under predicted by GEOS-Chem and H-CMAQ, whereas H-CAMx exhibits a very low bias and very good gross error over all sites. Unlike all other groups of surface monitors, model-to-model differences are more consistent across all sites.

Table 4-5 summarizes results described above by listing site-averaged annual bias (NMB), gross error (NME) and correlation coefficient (R) over each of the five monitoring groups and for each model. Statistics for Oceanic sites exclude Mauna Loa, Hawaii where all models were biased low because coarse resolution could not replicate high ozone at the high altitude of the monitor (but statistics at Canary Islands are included). Reported statistics are compared to the photochemical modeling benchmarks developed by Emery et al. (2016) to provide context for the range of values. Of the 15 metrics listed for each model (3 statistics over 5 monitoring groups), GEOS-Chem exceeds statistical benchmarks twice (large negative NMB), H-CAMx exceeds twice (large positive NMB and low R), and H-CMAQ exceeds five times (large positive and negative NMB, large NME and low R).

Table 4-5. Site-averaged annual bias (NMB, %), gross error (NME, %) and correlation coefficient (R) over five global monitoring groups for each model. Statistics are color coded according to whether they meet (green) or exceed (orange) ozone statistical performance criteria recommended by Emery et al. (2016) for regional photochemical modeling (NMB $\leq \pm 15\%$; NME $\leq 25\%$, R > 0.50).

Monitor Group	GEOS-Chem NMB	H-CAMx NMB	H-CMAQ NMB	GEOS-Chem NME	H-CAMx NME	H-CMAQ NME	GEOS-Chem R	H-CAMx R	H-CMAQ R
US	2%	15%	4%	16%	20%	18%	0.65	0.67	0.59
Europe	-14%	6%	-5%	20%	17%	17%	0.76	0.74	0.73
Asia	-8%	16%	13%	21%	25%	27%	0.78	0.74	0.76
Oceanic	-19%	9%	19%	21%	18%	23%	0.71	0.72	0.62
Polar	-20%	-3%	-25%	24%	15%	30%	0.68	0.43	0.22

4.5 H-CAMx Sensitivity Results

4.5.1 Ozonesonde Comparisons

Figure 4-16 presents modeled and measured ozone profiles from H-CAMx Run1 through Run3. All H-CAMx sensitivity cases exhibit improved performance over Run0 in replicating the mean and range of stratospheric ozone, a direct effect of the adjustments implemented in the stratospheric ozone scheme after the evaluation of Run0. However, H-CAMx continues to under predict ozone in the lower portion of the stratosphere at mid- and high-latitude locations by missing the consistent profile bowing just above ~ 250 mb (10-11 km). H-CAMx continues to perform well in replicating upper tropospheric and lower stratospheric ozone profiles at low-latitude sites, with the exception of two Asian sites (Hong Kong and Hanoi) downwind of the Himalayas where the model over predicts significantly at these high altitudes.

The higher stratospheric ozone in all sensitivity cases results in a slight increase in upper and mid-tropospheric ozone below ~ 250 mb. Somewhat surprisingly, this increase is further enhanced with the introduction of improved vertical resolution in Run2 and Run3. Therefore, the diffusive transport of stratospheric ozone into the upper troposphere is not so much a result of insufficient vertical resolution, but apparently caused by the numerically diffusive nature of the CAMx vertical transport solver in combination with the WRF terrain-following vertical coordinate structure and the CAMx vertical velocity calculation, which includes apparent motions induced by the time/space undulations in the vertical grid structure. This issue could be relieved, at least partially, by employing WRF's new hybrid vertical coordinate, which removes the terrain-following feature in upper atmospheric layers.

There is no obvious impact from introducing the CAMx Cloud-in-Grid sub-grid convection treatment in Run3. We note there are a few soundings in which the mean and range of ozone slightly differs from Run2, but there is no clear indication of any differences in replicating tropospheric ozone profiles. In fact, deep convection tends to slightly increase already over-predicted ozone near the surface relative to Run1 and Run2.

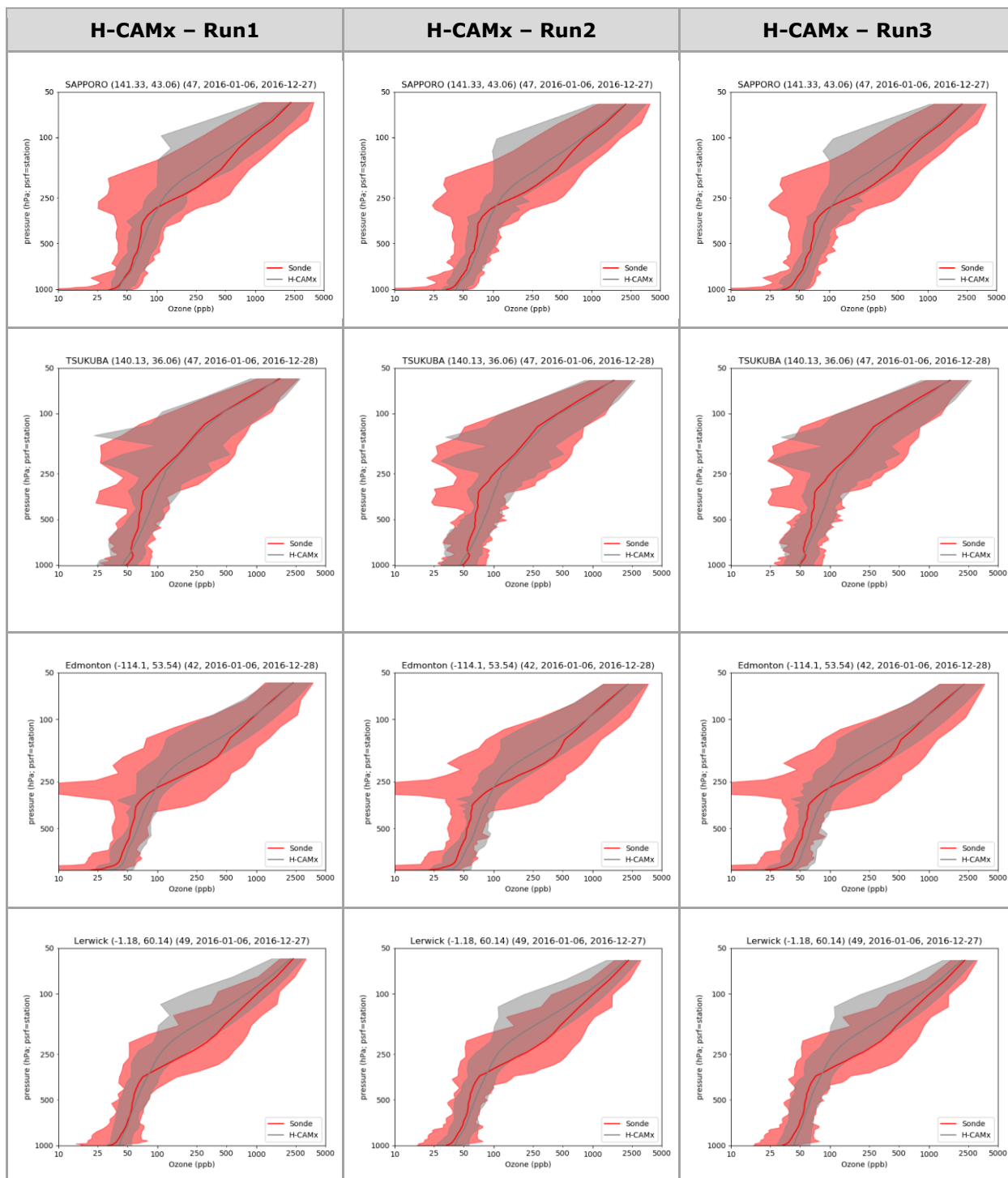


Figure 4-16. H-CAMx (grey) and observed (red) ozone profiles at global ozonesonde sites. The average over all 2016 profiles are shown as the solid lines, annual minimum to maximum ozone ranges are shaded. The number of profiles in 2016 and station latitude/longitude are noted above each plot.

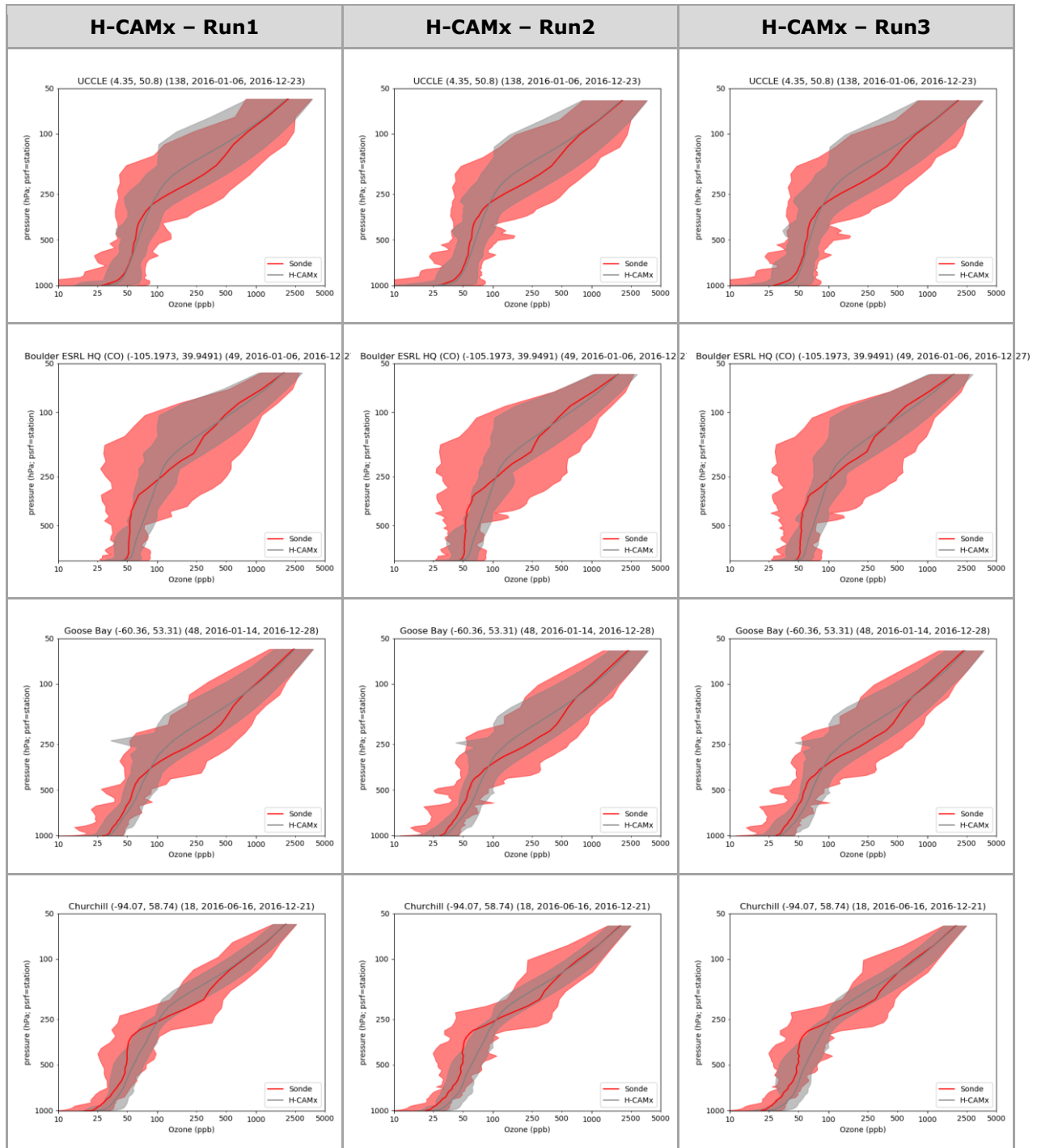


Figure 4-16 (continued).

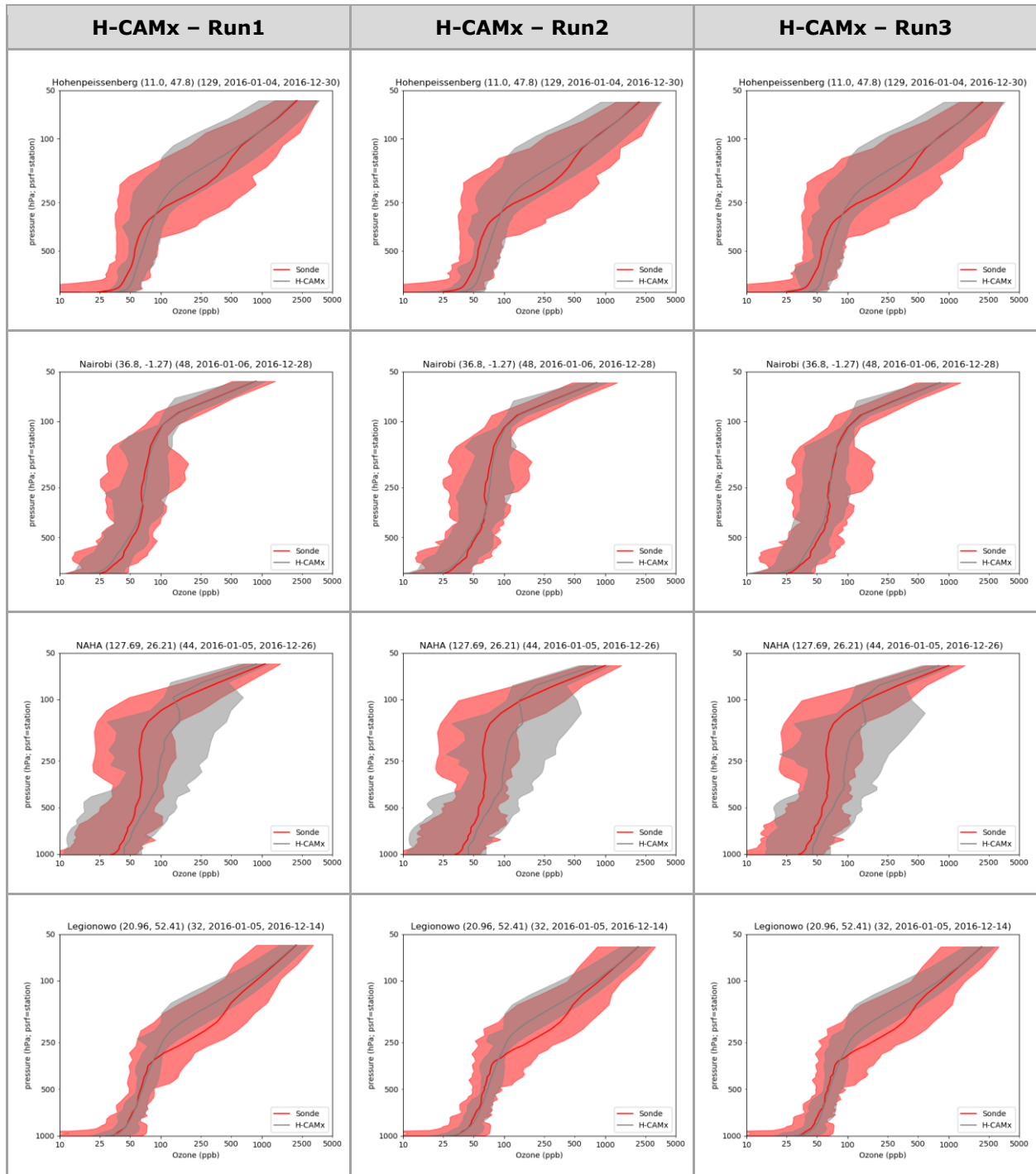


Figure 4-16 (continued).

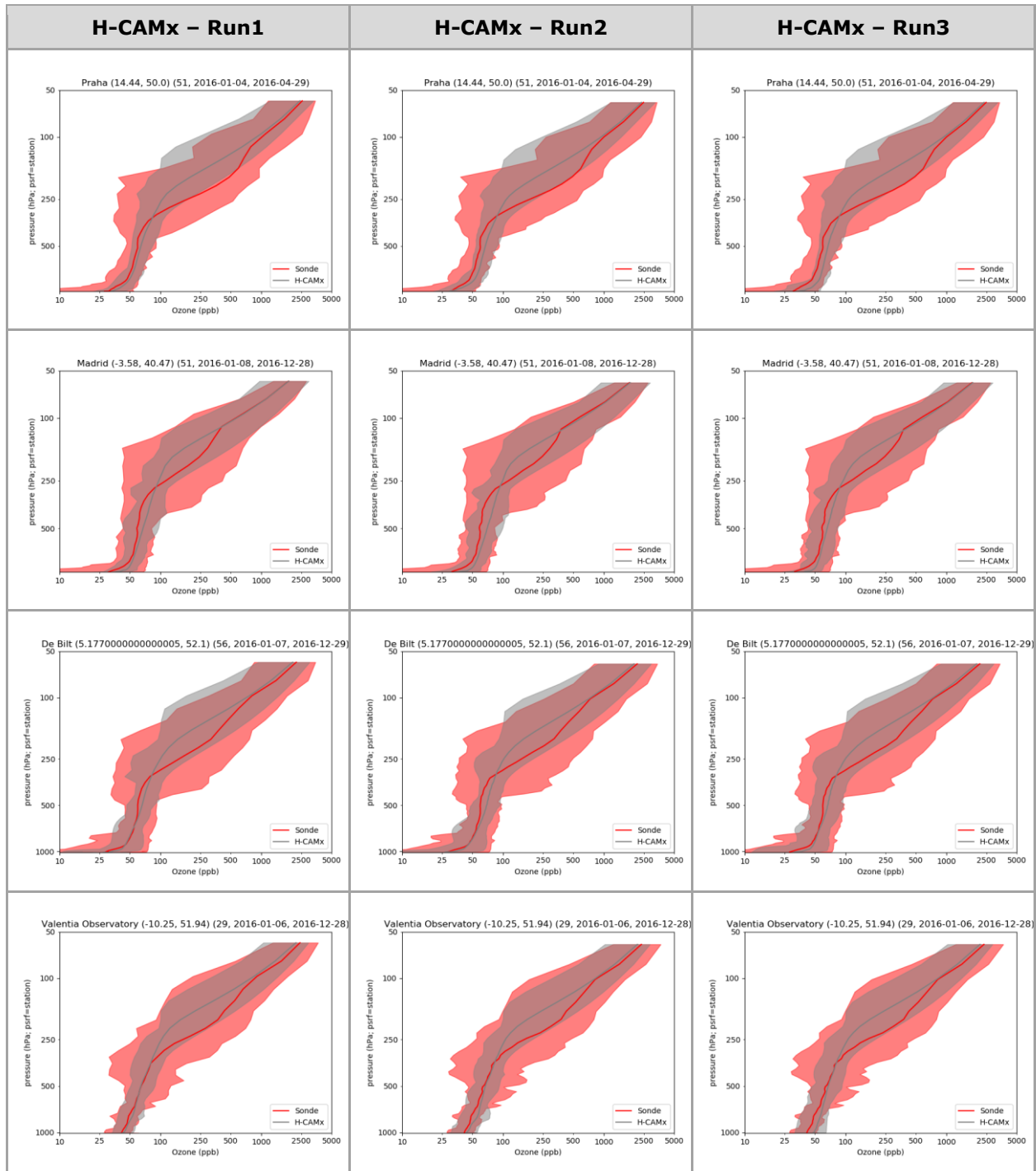


Figure 4-16 (continued).

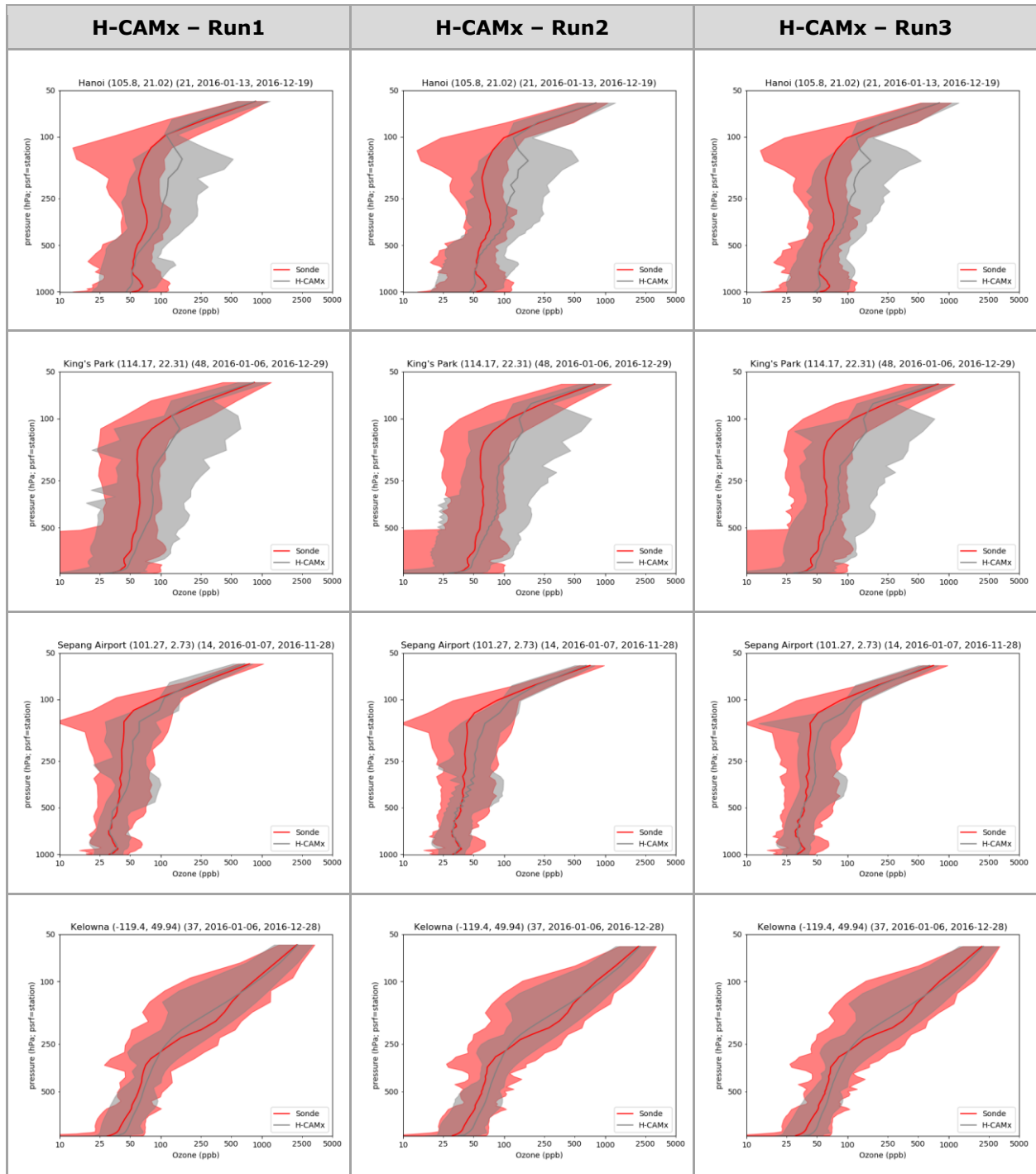


Figure 4-16 (continued).

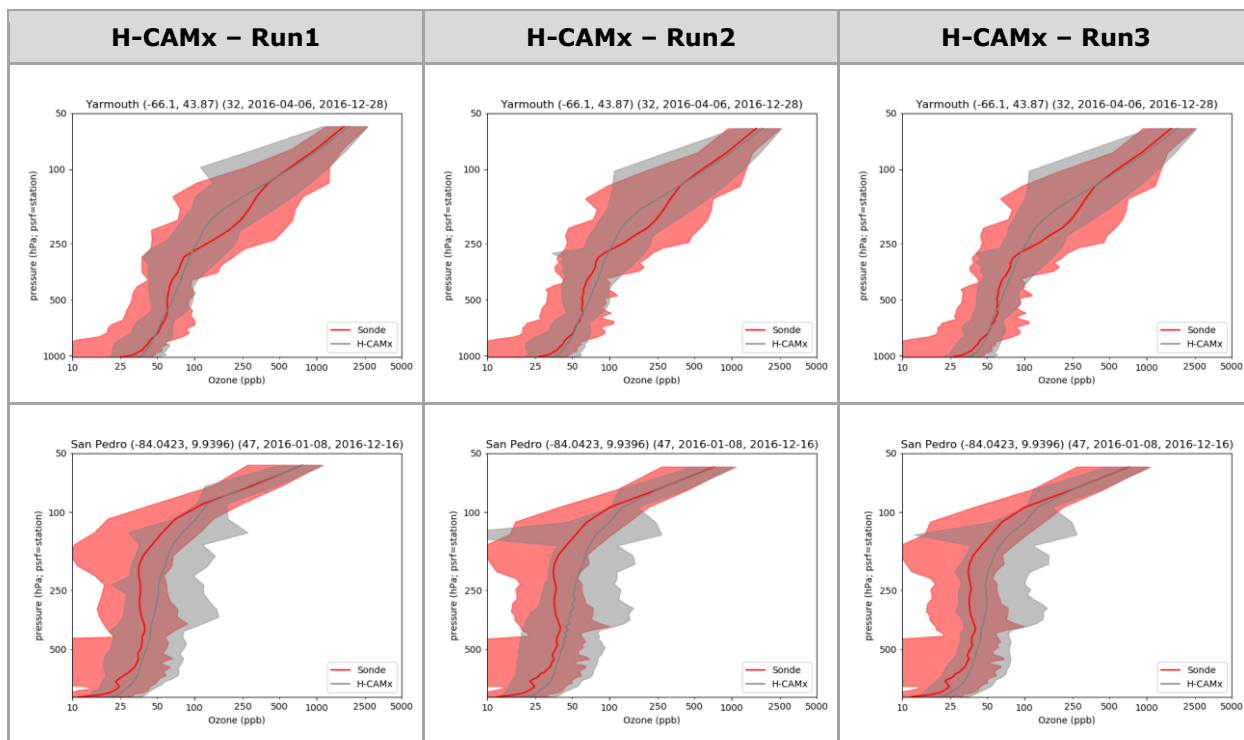


Figure 4-16 (concluded).

4.5.2 Surface Ozone Comparisons

Figures 4-17 through 4-21 compare measured and modeled surface ozone ranges and statistical performance metrics by site for each of the five site groups. Model results and statistics for H-CAMx Run0 through Run3 are shown together to ease comparison. Overall, the different H-CAMx sensitivity cases are consistent with Run0 results, with a continued tendency for H-CAMx to overpredict ozone in all cases. Interestingly, over predictions tend toward progressively higher means moving from Run1 through Run3, although this does not necessarily translate to a similar effect for site-specific ozone ranges, which show more mixed results. The pattern of progressively higher means is especially apparent among the US and European groups, and somewhat apparent in the Asia group. However, this tendency is not as clear in the Oceanic and Polar groups.

None of the modifications applied in Run1 through Run3 (our own WRF run, revised stratospheric ozone treatment, monthly-mean boundary conditions and satellite-derived top concentrations, additional layers and improved vertical resolution, use of the sub-grid cloud mixing scheme) result in fundamentally different effects on surface ozone, except to drive model bias and gross error slightly higher with the introduction of each change. We expect that higher modeled ozone in Run1 is most likely driven by the change in stratospheric ozone treatment that increased tropospheric ozone slightly, while much smaller effects likely occur from our WRF run or the alternative initial/boundary/top concentrations. While Run2 with higher vertical resolution introduced minor increases in aloft ozone profiles, we expect that the slightly higher mean surface ozone over Run1 is mostly caused by the deeper surface layer. This would cause less ozone titration by diluting NOx-rich areas, perhaps slightly higher ozone production rates in rural terrestrial areas by shifting VOC:NOx ratios toward more efficient ranges, and less ozone destruction by diluting oceanic halogens over oceanic areas. The slightly higher Run3 ozone over Run2 is more difficult to understand, but given that we only

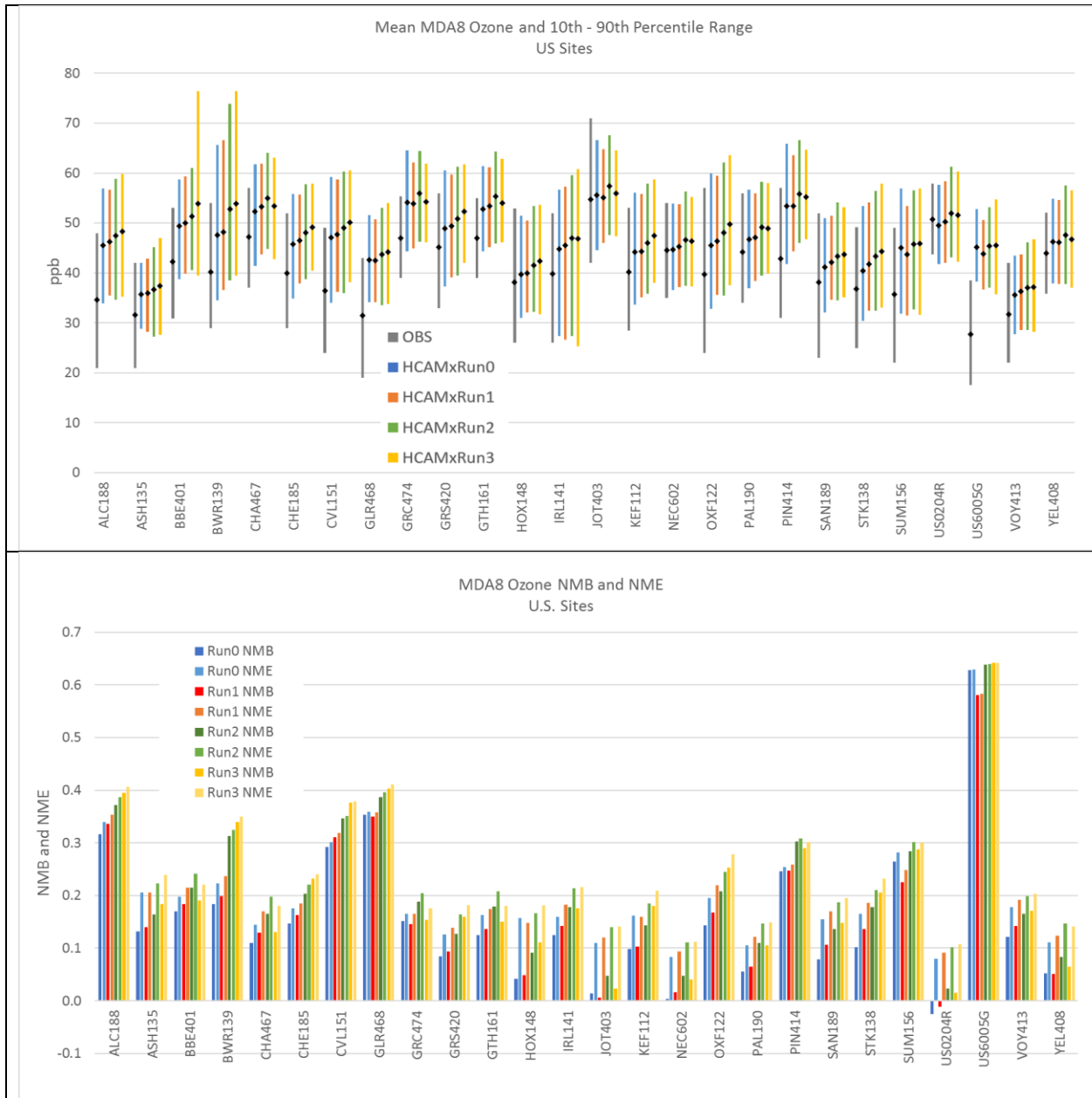


Figure 4-17. Measured and H-CAMx annual average (black dots) and 10th-90th percentile ranges (vertical bars) of surface ozone by US site (top panel), and modeled statistical performance metrics for bias (NMB as decimal fraction) and gross error (NME as decimal fraction) by US site (bottom panel). Observations are shown in grey, H-CAMx results are shown in color.



Figure 4-18. Measured and H-CAMx annual average (black dots) and 10th-90th percentile ranges (vertical bars) of surface ozone by European site (top panel), and modeled statistical performance metrics for bias (NMB as decimal fraction) and gross error (NME as decimal fraction) by European site (bottom panel). Observations are shown in grey, H-CAMx results are shown in color.

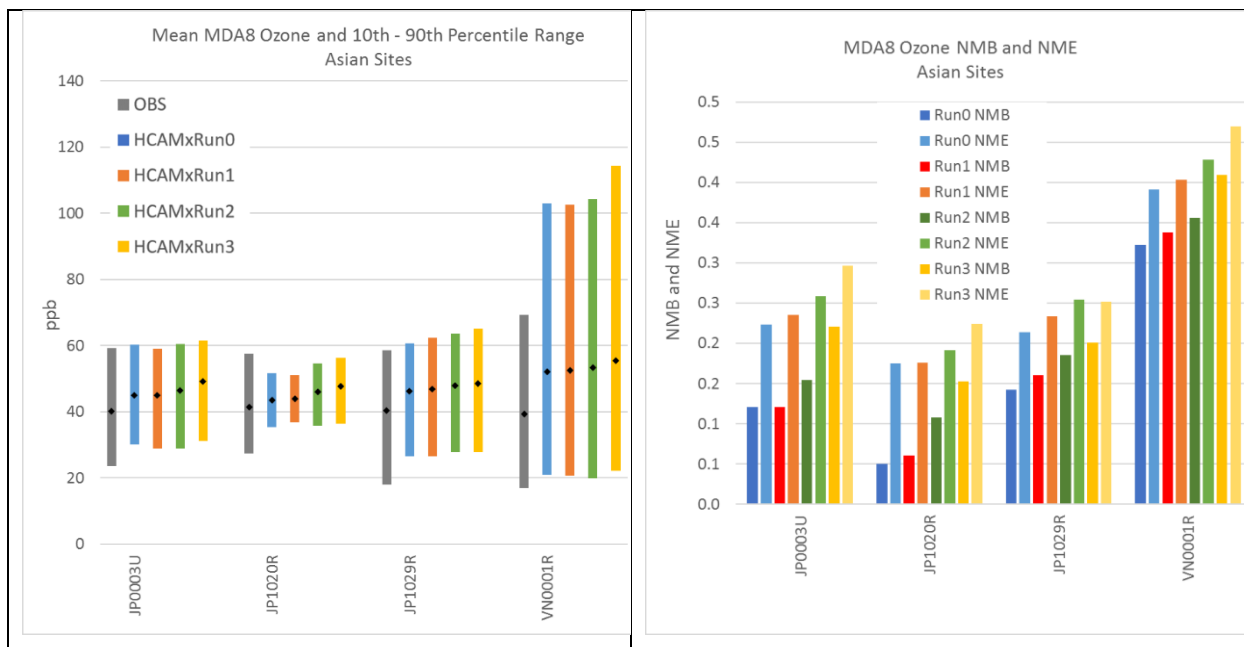


Figure 4-19. Measured and H-CAMx annual average (black dots) and 10th-90th percentile ranges (vertical bars) of surface ozone by Asian site (left panel), and modeled statistical performance metrics for bias (NMB as decimal fraction) and gross error (NME as decimal fraction) by Asian site (right panel). Observations are shown in grey, H-CAMx results are shown in color.

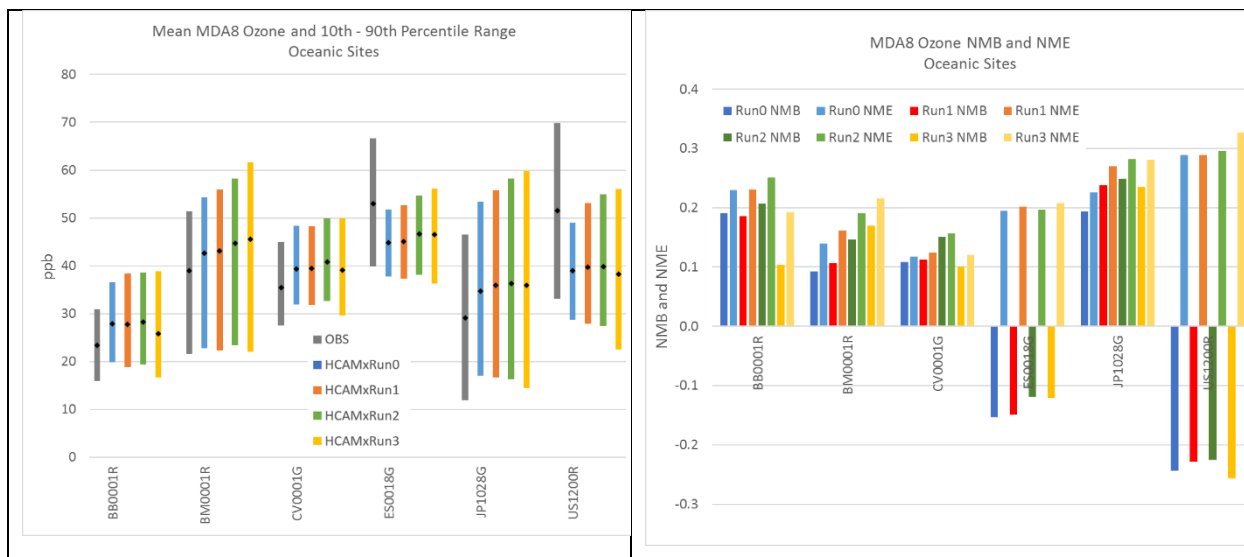


Figure 4-20. Measured and H-CAMx annual average (black dots) and 10th-90th percentile ranges (vertical bars) of surface ozone by Oceanic site (left panel), and modeled statistical performance metrics for bias (NMB as decimal fraction) and gross error (NME as decimal fraction) by Oceanic site (right panel). Observations are shown in grey, H-CAMx results are shown in color.

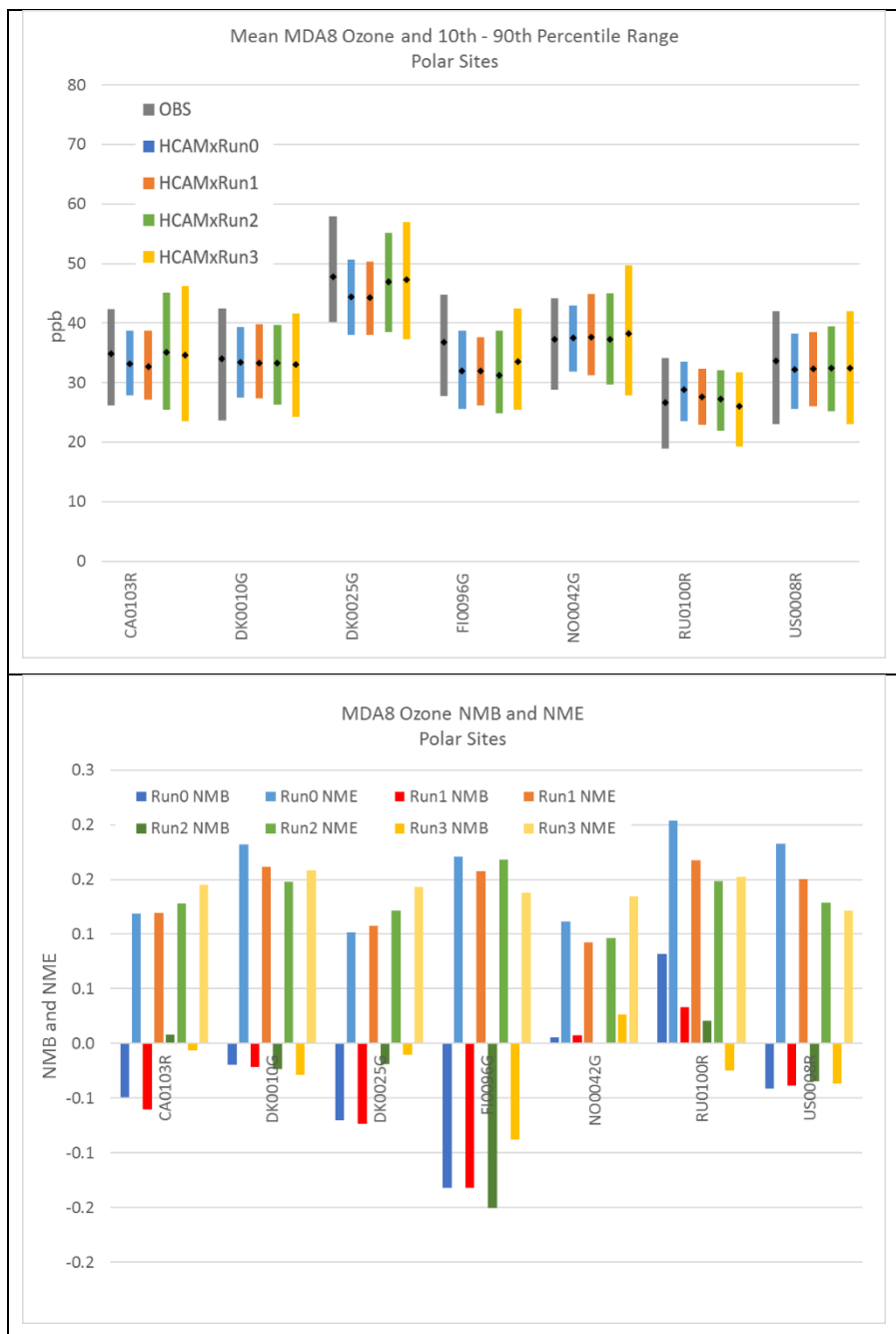


Figure 4-21. Measured and H-CAMx annual average (black dots) and 10th-90th percentile ranges (vertical bars) of surface ozone by Polar site (left panel), and modeled statistical performance metrics for bias (NMB as decimal fraction) and gross error (NME as decimal fraction) by Polar site (right panel). Observations are shown in grey, H-CAMx results are shown in color.

changed the treatment of sub-grid convection (in both WRF and H-CAMx), convection around the hemisphere brought more mid- and upper-level ozone to the surface throughout the year relative to the enhanced cloud mixing imposed in our deep cloud Kv patching applied in Run0 through Run2. Note that Run3 had little average impact in the polar region given lack of convective activity there.

Table 4-6 summarizes results described above by listing site-averaged annual bias (NMB), gross error (NME) and correlation coefficient (R) over each of the five monitoring groups and for H-CAMx Run1 through Run3. Statistics for Oceanic sites exclude Mauna Loa, Hawaii where all runs were biased low because coarse resolution could not replicate high ozone at the high altitude of the monitor (but statistics at Canary Islands are included). Relative to Run0, the higher ozone in all sensitivity cases results in upward shifts in NMB and NME over all monitor groups, yet rather consistent correlation. Poor correlation among the Polar group in Run0 is improved substantially in the sensitivity cases, while bias and error performance over the US and Asia degrade to outside benchmark criteria. The high bias among the Asia group is driven by higher ozone at Hanoi, Vietnam, as described in Section 4.4.2. Removing Hanoi from statistics brings NMB and NME to within benchmark criteria.

Table 4-6. Site-averaged annual bias (NMB, %), gross error (NME, %) and correlation coefficient (R) over five global monitoring groups for each H-CAMx run. Statistics are color coded according to whether they meet (green) or exceed (orange) ozone statistical performance criteria recommended by Emery et al. (2016) for regional photochemical modeling (NMB ≤ ±15%; NME ≤ 25%, R > 0.50).

Monitor Group	Run1 NMB	Run2 NMB	Run3 NMB	Run1 NME	Run2 NME	Run3 NME	Run2 R	Run2 R	Run3 R
US	16%	20%	21%	21%	24%	25%	0.64	0.64	0.63
Europe	6%	8%	12%	17%	17%	19%	0.74	0.71	0.69
Asia	17%	20%	25%	26%	28%	31%	0.74	0.74	0.73
Oceanic	4%	7%	4%	21%	23%	22%	0.64	0.61	0.59
Polar	-4%	-3%	-2%	14%	13%	14%	0.54	0.59	0.59

4.6 Recommended H-CAMx Configuration

On the basis of the analyses and results summarized in this section, we recommend that TCEQ adopt the modeling system configuration defined in Run1: satellite-derived top BCs for ozone; monthly “climatological library” of IC/BCs for all chemical species as derived from GEOS-Chem; and the original 44-layer structure in both WRF and H-CAMx. The lower resolution offered with 44 layers does not appear to have a material impact on simulated ozone while it minimizes runtimes. We cannot offer any specific recommendation on the use of the Cloud-in-Grid model as it had negligible apparent impacts on ozone distributions and model performance against measurements. We recommend continuing to use a spin-up period over the fourth quarter of 2015, which is now possible with the library of chemically-evolved and consistent IC fields derived from GOES-Chem. Figure 4-22 displays season-averaged Run1 surface ozone fields over the H-CAMx modeling domain.

O3MDA8 seasonal average

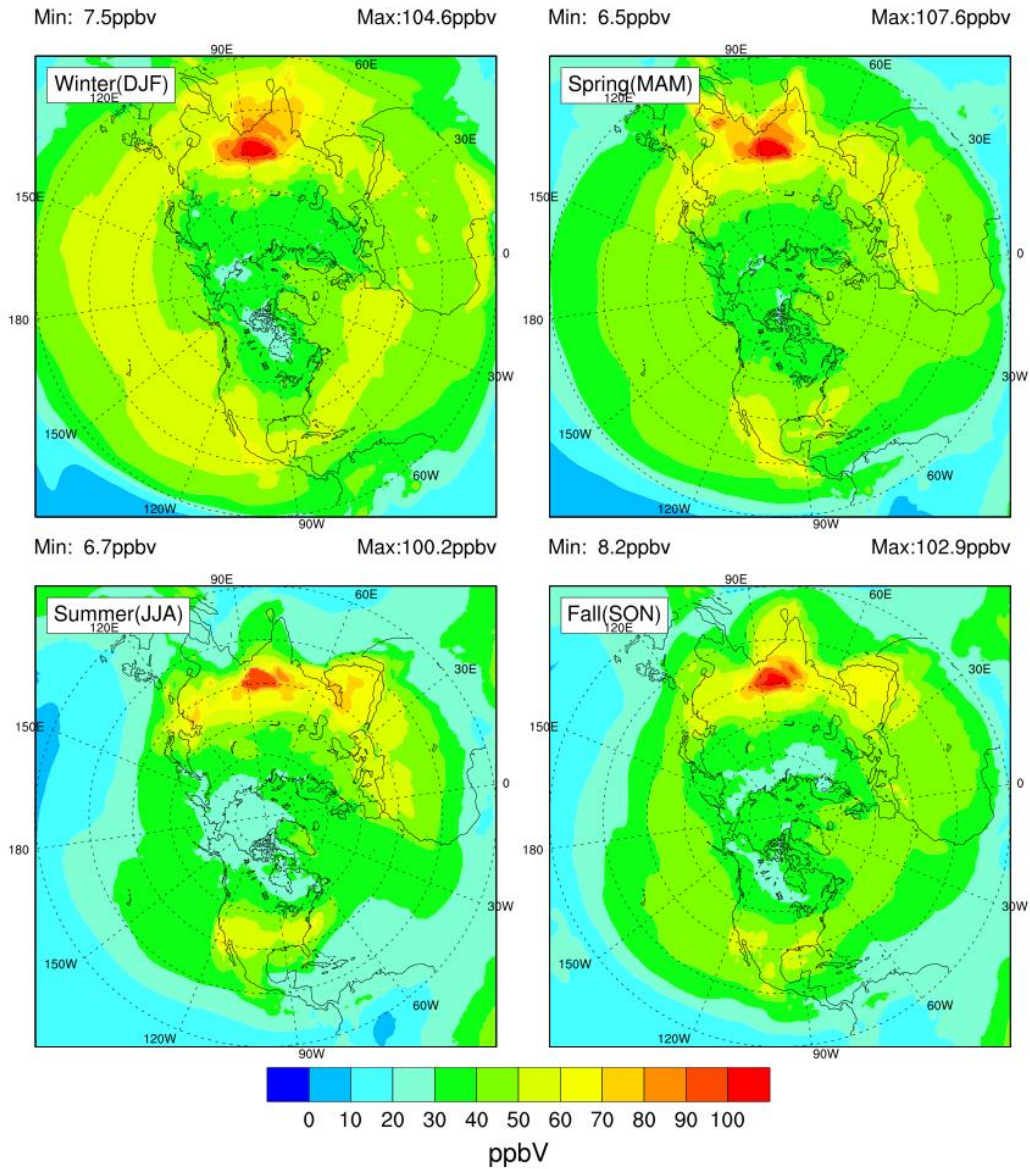


Figure 4-22. Season-averaged surface ozone fields simulated by the H-CAMx Run1 modeling configuration: winter (DJF) in top left, spring (MAM) in top right, summer (JJA) in bottom left, and autumn (SON) in bottom right.

5.0 CONCLUSION AND RECOMMENDATIONS

5.1 Summary

This project built upon previous work to enhance and further evaluate H-CAMx in preparation for regulatory and policy use. The project involved three components: (1) evaluate and develop the use of satellite data products to derive boundary concentrations; (2) apply and evaluate alternative meteorological model configurations to test sensitivity to vertical resolution and sub-grid convection; and (3) conduct a more comprehensive model performance for the year 2016.

We developed daily H-CAMx ozone top BC input files from daily global AIRS satellite ozone data at the 50 mb pressure level, which coincides with the top pressure of both WRF and H-CAMx modeling domains. A new Fortran program translates AIRS data to the CAMx top BC input file format, which includes filling missing data zones that routinely occur between the swaths and in other more randomly-occurring areas.

New considerations were necessary to address IC and lateral BCs for ozone and other important and highly spatially/temporally variable compounds such as CO, NO_x, VOC and PM, to alleviate the dependence of H-CAMx on third-party global models. These compounds are especially important when considering initial conditions, as we seek to characterize pollutant concentration distributions throughout the domain in a manner that reduces model spin-up times. We developed a library of monthly-averaged ICs (three-dimensional) and lateral BCs (two-dimensional) for all CAMx species from the raw output of GEOS-Chem. These monthly, spatially-varying inputs can be used to represent a recent global climatology within a reasonable interval (arguably ± 5 years) from 2016. Since they are model-derived, all species are chemically consistent with each other. This solution provides the best balance among flexibility and representativeness and will allow for a shortened hemispheric spin-up period.

We employed the same version of WRF used by EPA to run a replication of EPA's configuration and then ran two alternative WRF configurations over the hemispheric grid for the year 2016, including a spin-up period for H-CAMx covering October 1 – December 31, 2015. Key changes in the WRF configuration included: (1) increasing vertical resolution in the mid-troposphere through the lower stratosphere to the extent that is similar to or better than the GOES-Chem global model; and (2) invoking the multi-scale Kain-Fritsch sub-grid cumulus option, which supports the CAMx CiG convective sub-model. The second modification also required the use of different WRF surface model and boundary layer schemes.

We conducted a qualitative comparison of wind speed, temperature and humidity fields over the modeling domain at two levels (near-surface and near-tropopause) and for two months (January and July) among the four WRF runs. Comparing to EPA's WRF results indicated no spurious or concerning differences and the larger differences occurring for near-surface humidity and temperature were likely related to our parallelization methodology that affects the soil moisture nudging approach. Differences arising from the modified layer structure were consistent with expectations and related to deeper layers resolving the lower boundary layer and better resolution of the temperature and wind profiles at jet stream altitudes. Only minor effects aloft and near the surface occurred with modified convection, boundary layer, and surface schemes.

We compared results from 4 H-CAMx runs, GEOS-Chem, and EPA's H-CMAQ to tropospheric/stratospheric ozone profiles from 22 global ozonesonde balloon launch sites, and to surface-level ozone measurements from 67 global monitoring sites. With respect to ozone profiles, GEOS-Chem

consistently best replicated stratospheric ozone at most sites around the world, with a slight negative bias in the troposphere. H-CMAQ was similar to GEOS-Chem but consistently exhibited more negative bias throughout the profiles. Conversely, H-CAMx consistently generated a negative bias in the stratosphere and a positive bias in the troposphere. All models generally exhibited narrower minimum-to-maximum ranges than the observations. This comparison revealed some puzzling stratospheric ozone traits in H-CAMx, which we were able to partially alleviate with some minor improvements to the stratospheric ozone treatment.

At the surface, all three models performed adequately at most sites with a few outliers. GEOS-Chem exhibited a consistently negative ozone bias, H-CAMx exhibited a consistently positive ozone bias, while H-CMAQ had a mix of over and under predictions. Statistical performance for H-CAMx and H-CMAQ were more consistent with each other than GEOS-Chem, given their equivalent meteorology, emissions, and grid structures. For example, both H-CAMx and H-CMAQ over predicted a summer reduction in marine ozone at Trinidad Head, California, whereas GEOS-Chem properly simulated that feature. The cause for this performance difference remains unclear. Additionally, we note an apparent issue with over estimated emission rates in southeast Asia, particularly around Hanoi, Vietnam, in the H-CAMx/CMAQ datasets. This led to very large and unrealistic over predictions of ozone during the spring season in that area. Finally, all three models under estimated ozone at high altitude oceanic sites perched on the volcanoes at Mauna Loa, Hawaii and Canary Islands. We attribute this feature to the inability for coarse resolution to resolve the altitudes of these sites.

In analyzing performance of H-CAMx sensitivity runs against ozonesondes, we found that all H-CAMx sensitivity cases exhibited improved performance in the stratosphere from adjusting the stratospheric ozone scheme. However, H-CAMx performance aloft degraded at two Asian sites (Hong Kong and Hanoi) downwind of the Himalayas where the model over predicted significantly at high altitudes. The higher stratospheric ozone in all sensitivity cases resulted in a slight increase in upper and mid-tropospheric ozone. Somewhat surprisingly, this increase was further enhanced with the introduction of improved vertical resolution. Therefore, the diffusive transport of stratospheric ozone into the upper troposphere was not so much a result of insufficient vertical resolution, but apparently caused by the numerically diffusive nature of the CAMx vertical transport solver in combination with the WRF terrain-following vertical coordinate structure and the CAMx vertical velocity calculation, which includes apparent motions induced by the time/space undulations in the vertical grid structure. This issue could be relieved, at least partially, by employing WRF's new hybrid vertical coordinate, which removes the terrain-following feature in upper atmospheric layers. There were no obvious impacts to ozone profiles around the hemisphere from introducing the CAMx Cloud-in-Grid sub-grid convection treatment.

At the surface, the different H-CAMx sensitivity cases were consistent, with a continued tendency for H-CAMx to overpredict ozone in all cases. Over predictions tended toward progressively higher mean ozone in each successive case, especially among the US and European sites. None of the modifications applied in the sensitivity cases resulted in fundamentally different effects on surface ozone, except to drive model bias and gross error slightly higher with the introduction of each change. We expect that higher modeled ozone was partially related to the change in the stratospheric ozone treatment that increased tropospheric ozone slightly, while much smaller effects likely occurred from changes in WRF or the alternative initial/boundary/top concentrations. In the case with higher vertical resolution, surface ozone increased most likely because of the deeper surface layer as opposed to any significant affect aloft. The changes in sub-grid convection, boundary layer and surface layer schemes in WRF tended to bring more mid- and upper-level ozone was brought to the surface throughout the year; these had little average impact in the polar region given lack of convective activity there.

5.2 Recommendations

On the basis of analyses described in this report, we recommend that TCEQ adopt the modeling system configuration defined in Run1: satellite-derived top BCs for ozone; monthly "climatological library" of IC/BCs for all chemical species as derived from GEOS-Chem; and the original 44-layer structure in both WRF and H-CAMx. The lower resolution offered with 44 layers does not appear to have a material impact on simulated ozone while it minimizes runtimes. We cannot offer any specific recommendation on the use of the Cloud-in-Grid model as it had negligible apparent impacts on ozone distributions and model performance against measurements. We recommend continuing to use a spin-up period over the fourth quarter of 2015, which is now possible with the library of chemically-evolved and consistent IC fields derived from GOES-Chem.

We have delivered CAMx source code, the entire modeling dataset, and new pre-processor codes to TCEQ for additional testing and use.

We further recommend the following additional activities and model enhancements, in approximate order of importance.

- TCEQ staff should apply H-CAMx in the recommended configuration to learn how to use the tool, further study its characteristics, and conduct Source Apportionment runs that can support the development of tagged boundary conditions for regional US/Texas modeling applications.
- Add NO₂ to top boundary conditions along with ozone so that a stratospheric NO_x column can be maintained in the model; this is critically important to allow for model comparisons to satellite NO₂ column data.
- Apply WRF for H-CAMx using the hybrid vertical coordinate, which should help to alleviate numerical diffusion in the vertical advection scheme.
- Test CAMx using an alternative vertical advection solver to reduce numerical diffusion; Ramboll has completed a concurrent TCEQ project (Ramboll, 2020b) investigating the use of the Piecewise Parabolic Method of Colella and Woodward (1984) with promising results.
- Add the ability to change or directly simulate methane in the model, to allow for simulations that better address various levels of anthropogenic activity on ozone (e.g., pre-industrial and/or future greenhouse gas scenarios, etc.); currently a single methane concentration is set in the chemical mechanisms that reflects a contemporary global-average concentration.
- Investigate model sensitivity to the choice of surface deposition scheme, or review and consider any contemporary information on deposition, as this process is important for the tropospheric ozone budget; the Zhang et al. (2003) scheme was used in all H-CAMx work to date, yet the original Wesely (1989) scheme remains available and results in higher ozone deposition rates relative to Zhang.
- Investigate causes for marine summer ozone suppression at Trinidad Head (and likely along much of the western US coastline, and elsewhere) and the physical and chemical schemes in GEOS-Chem that may be responsible for properly capturing this effect; consider implementing the GEOS-Chem scheme identified as the key factor for model differences.
- Investigate issues noted with the EPA-generated emission inventory in Southeast Asia that leads to unrealistically large ozone over predictions specifically over northern Vietnam.

6.0 REFERENCES

- Barnet, C., E. Manning, P. Rosenkranz, L. Strow, J. Susskind, M.T. Chahine, H.H. Aumann, 2007. Algorithm Theoretical Basis Document: AIRS-Team Retrieval for Core Products and Geophysical Parameters, Level 2 (Version 4.0 1 March 2007; JPL D-17006). https://docserver.gesdisc.eosdis.nasa.gov/repository/Mission/AIRS/3.3_ScienceDataProductDocumentation/3.3.4_ProductGenerationAlgorithms/20070301_L2_ATBD_signed.pdf.
- Colella, P., and P.R. Woodward, 1984. The Piecewise Parabolic Method (PPM) for Gas-dynamical Simulations. *J. Comp. Phys.*, 54, 174-201.
- Bey, I., D.J. Jacob, R.M. Yantosca, J.A. Logan, B.D. Field, A.M. Fiore, Q. Li, H.Y. Liu, L.J. Mickley, M.G. Schultz, 2001. Global modeling of tropospheric chemistry with assimilated meteorology: Model description and evaluation. *J. Geophys. Res. Atmos.*, 106(D19), 23073–23095, 2001.
- Eastham, S.D. and D.J. Jacob, 2017. Limits on the ability of global Eulerian models to resolve intercontinental transport of chemical plumes. *Atmos. Chem. Phys.*, 17(4), 2543–2553, doi:10.5194/acp-17-2543-2017.
- Emery, C., Z. Liu, A.G. Russell, M.T. Odman, G. Yarwood, N. Kumar, 2016. Recommendations on statistics and benchmarks to assess photochemical model performance. *Journal of the Air & Waste Management Association*, <http://dx.doi.org/10.1080/10962247.2016.1265027>.
- Harvard University, 2020. GEOS-Chem Model website. <http://acmg.seas.harvard.edu/geos>.
- Herman, R., D. Fu, S. Kulawik, K. Miyazaki, G. Osterman, K. Bowman, J. Worden, et al., 2017. AIRS/OMI Validation Report, Version 1.0. Prepared by NASA Jet Propulsion Laboratory (December 8, 2017). https://avdc.gsfc.nasa.gov/pub/data/satellite/Aura/TES/AIRS_OMI/Support/AIRSOMI_ValidationReport_8Dec2017.pdf.
- Mathur, R., J. Xing, R. Gilliam, G. Sarwar, C. Hogrefe, J. Pleim, G. Pouliot, S. Roselle, T.L. Spero, D.C. Wong, J. Young, 2017. Extending the Community Multiscale Air Quality (CMAQ) modeling system to hemispheric scales: overview of process considerations and initial applications. *Atmos. Chem. Phys.*, 17, 12449–12474.
- NCAR, 2017. Weather Research and Forecasting ARW, Version 3 Modeling System User's Guide. Mesoscale and Microscale Meteorology Division, National Center for Atmospheric Research (v3.8, January 2017). https://www2.mmm.ucar.edu/wrf/users/docs/user_guide_V3.8/ARWUsersGuideV3.8.pdf.
- Olsen, E.T. (Ed.) et al., 2017. AIRS/AMSU/HSB Version 6, Level 2, Product User Guide. Prepared by the Jet Propulsion Laboratory, California Institute of Technology (27 November 2017, Version 1.7.2). https://docserver.gesdisc.eosdis.nasa.gov/repository/Mission/AIRS/3.3_ScienceDataProductDocumentation/3.3.4_ProductGenerationAlgorithms/V6_L2_Product_User_Guide.pdf.
- Ramboll, 2018. Scoping Study for Development/Application of CAMx for the Northern Hemisphere. Prepared for the Texas Commission on Environmental Quality, Austin, TX, by Ramboll, Novato, CA (Work Order No. 582-18-83121-32, July 2018).
- Ramboll, 2019a. Development and Testing of a Hemispheric Comprehensive Air Quality Model with Extensions (CAMx) Application. Prepared for the Texas Commission on Environmental Quality, Austin, TX, by Ramboll, Novato, CA (Work Order No. 582-19-93346-05, August 2019).
- Ramboll, 2019b. Global Observation Dataset Selection for GEOS-Chem Model Performance Evaluation. Prepared for the Texas Commission on Environmental Quality, Austin, TX by Ramboll, Novato, CA (Work Order No. 582-19-92775-04, April 2019).
- Ramboll, 2020a. User's Guide: Comprehensive Air quality Model with extensions (CAMx), version 7.00. www.camx.com.
- Ramboll, 2020b. Evaluation of Model Vertical Structure and Top Concentrations. Prepared for the Texas Commission on Environmental Quality, Austin, TX by Ramboll, Novato, CA (Work Order No. 582-20-11097-012, June 2020).

- Wesely, M.L. 1989. Parameterization of Surface Resistances to Gaseous Dry Deposition in Regional-Scale Numerical Models. *Atmos. Environ.*, 23, 1293-1304.
- WMO, 1992. International Meteorological Vocabulary (2nd ed.). Geneva: Secretariat of the World Meteorological Organization, p. 636. ISBN 978-92-63-02182-3.
- Zhang, L., J. R. Brook, and R. Vet. 2003. A revised parameterization for gaseous dry deposition in air-quality models. *Atmos. Chem. Phys.*, 3, 2067–2082.
- Zheng, Y. K. Alapaty, J.A. Herwehe, A.D. Del Genio, D. Niyogi, 2016. Improving High-Resolution Weather Forecasts Using the Weather Research and Forecasting (WRF) Model with an Updated Kain–Fritsch Scheme. *Monthly Weather Review*, 144, 833-860, DOI: 10.1175/MWR-D-15-0005.1. <https://journals.ametsoc.org/doi/pdf/10.1175/MWR-D-15-0005.1>.
- Zhuang, J., D.J. Jacob, S.D. Eastham, 2017. The importance of vertical resolution in the free troposphere for modeling intercontinental plumes. *Atmos. Chem. Phys. Discuss.*, <https://doi.org/10.5194/acp-2017-1124>.

Appendix A. Statistical Definitions

Metric	Mathematical Definition
Mean Bias (MB)	$\frac{1}{N} \sum_{i=1}^N (P_i - O_i)$
Mean Error (ME)	$\frac{1}{N} \sum_{i=1}^N P_i - O_i $
Root Mean Squared Error (RMSE)	$\sqrt{\frac{\sum_{i=1}^N (P_i - O_i)^2}{N}}$
Normalized Mean Bias (NMB) (-100% to +∞)	$\frac{\sum_{i=1}^N (P_i - O_i)}{\sum_{i=1}^N O_i}$
Normalized Mean Error (NME) (0% to +∞)	$\frac{\sum_{i=1}^N P_i - O_i }{\sum_{i=1}^N O_i}$
Coefficient of Determination (R ²) (0 to 1)	$\left(\frac{\sum_{i=1}^N (P_i - \bar{P})(O_i - \bar{O})}{\sqrt{\sum_{i=1}^N (P_i - \bar{P})^2 \sum_{i=1}^N (O_i - \bar{O})^2}} \right)^2$

Symbol definitions:

P: Predicted quantity

O: Observed quantity

N: Number of prediction-observation pairs

i: Ith prediction-observation pair in set

$\bar{(\)}$: Mean